



HAL
open science

Effect of Residual Stress on the Elasticity of Fiber Networks.

Samuel Cazayus-Claverie

► **To cite this version:**

Samuel Cazayus-Claverie. Effect of Residual Stress on the Elasticity of Fiber Networks.. Biological Physics [physics.bio-ph]. Université Paris-Saclay, 2020. English. NNT : 2020UPASS030 . tel-02954169v1

HAL Id: tel-02954169

<https://theses.hal.science/tel-02954169v1>

Submitted on 30 Sep 2020 (v1), last revised 12 Oct 2020 (v2)

HAL is a multi-disciplinary open access archive for the deposit and dissemination of scientific research documents, whether they are published or not. The documents may come from teaching and research institutions in France or abroad, or from public or private research centers.

L'archive ouverte pluridisciplinaire **HAL**, est destinée au dépôt et à la diffusion de documents scientifiques de niveau recherche, publiés ou non, émanant des établissements d'enseignement et de recherche français ou étrangers, des laboratoires publics ou privés.

Effect Of Residual Stress On The Elasticity Of Fiber Networks.

Thèse de doctorat de l'Université Paris-Saclay

École doctorale n° 564, Physique en Île-de-France (EDPIF)
Spécialité de doctorat: Physique
Unité de recherche: LPTMS (UMR 8626)
Réfèrent: Faculté des sciences

Thèse présentée et soutenue à Orsay, le 25 février 2020, par

Samuel CAZAYUS-CLAVERIE

Composition du jury:

Giuseppe FOFFI Professeur, Laboratoire de Physique des Solides (UMR 8502)	Président
Chaouqi MISBAH Directeur de Recherche, Laboratoire Interdisciplinaire de Physique (UMR 5588)	Rapporteur
Anaël LEMAÎTRE Professeur, Laboratoire Navier (UMR 8205)	Rapporteur
Cécile LEDUC Chargée de recherche, Institut Pasteur (UMR 8640)	Examinatrice
Raphaël VOITURIEZ Directeur de Recherche, Laboratoire Jean Perrin (UMR 8237)	Examineur
Martin LENZ Directeur de recherche, Laboratoire de Physique Théorique et des Modèles statistiques, (UMR 8626)	Directeur
Jean-Marc ALLAIN Directeur de Recherche, Mechanics Department and Solid Me- chanics Laboratory (UMR 7649)	Membre Invité

Remerciements

Cette thèse de doctorat est le fruit de deux grandes de mes passions : la physique, et les mathématiques.

Je dois la première à mon grand-père “Pay” qui m’a sensibilisé à la physique dès le plus jeune âge : il laissait à ma portée des livres de science sur lesquels je ne manquais pas de m’arrêter. Les images suscitaient ma curiosité, j’allais voir Pay et nous finissions bien souvent par réaliser une expérience ensemble. On citera, pèle-mêle, la synthèse de cristaux de sel d’alun, la réalisation d’électro-aimants ou celle d’un démodulateur FM... Cette époque eut trop tôt une fin, et il n’y eut alors plus d’expériences encadrées par un adulte, pour le meilleur comme pour le pire ! En effet, j’entrepris de disséquer tout appareil qui croisait mon chemin, que ce soit pour le réparer... ou simplement pour satisfaire à ma curiosité. Rien à la maison n’échappa au bistouri du touche-à-tout que je devenais : les montres, le vélo, les instruments de musique, le téléphone, l’ordinateur, ou la voiture, m’auront tour à tour fasciné. Je me demandais bien comment on pouvait inventer de si merveilleuses machines. Je suis aujourd’hui convaincu que la physique y aide grandement, de par son efficacité opérationnelle.

Ma passion pour les mathématiques ne s’éveilla que plus tard. Enfant, je m’entendais mieux avec les lettres qu’avec les chiffres. J’éprouvais bien peu d’intérêt à compter, si ce n’est que cela permettait de résoudre des “carrés magiques” ! Au collège toutefois, ma découverte du calcul littéral me réconcilia avec la discipline : envisager la globalité à travers le concept d’inconnue me séduisait beaucoup ; que c’est beau l’abstraction ! Quelques années après, je découvris l’élégance d’une belle preuve, son côté poétique et sa logique irréfutable, cela finit de m’acquérir aux mathématiques.

Au gré de mes études, ce goût me mena à étudier la physique théorique, qui explore les fondements du monde dans un cadre élégant. L’universalité de son formalisme permet la transposition d’idées entre différents domaines ; même la biologie, j’en fus le premier surpris ! En effet, je ne découvris la biophysique que lors de ma deuxième année de master. Je fus attiré par cette branche dans laquelle l’expérience est accessible, et entretient d’étroits liens avec la théorie ! C’est ce qui décida de mon choix de sujet de thèse.

C’est au LPTMS d’Orsay, sur la campus de Paris-Saclay, que s’est déroulée cette thèse, dans le groupe de recherche de Martin Lenz. Je tiens à exprimer

ma gratitude envers Martin, dont le bureau m'est toujours resté ouvert, que ce soit pour des discussions scientifiques ou pour faire part de mes doutes lorsque j'en avais. Le plus dur fut bien souvent d'oser pousser sa porte, mais chaque fois que ce fut fait, j'en ressortis avec une piste fraîche. Merci aussi aux membres de mon comité de suivi à l'école doctorale Cécile Sykes et Denis Ullmo, qui ont été présents quand il le fallait, ainsi qu'à Emmanuel Trizac qui dirige le laboratoire avec compétence et succès, et qui trouve pourtant encore le temps d'observer les écureuils roux autour du laboratoire.

Je tiens aussi à remercier les membres de l'équipe de biophysique : Guglielmo, Ananio, Hugo, Félix, Lara, Mert, Luca, Mehdi et Pierre : comment donc la science aurait avancé sans les "Group Meetings", sans l'accueil royal de Pierre à Princeton, sans l'expertise en physique numérique de Mehdi, et sans nos discussions griffonnées sur un coin de tableau noir ?

Le laboratoire ne serait pas ce qu'il est sans les personnes qui le peuplent. Je pense ici à Claudine Le Vaou et Karolina Kolodziej dont le professionnalisme, l'organisation sans faille et la gentillesse sont si nécessaires. Je pense aussi à mes camarades du LPTMS, doctorants et post-doctorants : Alexandre, Bertand, Inés, Nina, Nadia, Kirill, Aurélien, Antonio, et Hao... Mais aussi, à mes camarades de bureau Mathieu, Ivan et Thibault, martyrs de mes idées inachevées, de mes nombres hyperduaux, et de mes erreurs de compilation, toujours partants pour un restau japonais ou un concert en fin de journée. J'ai souvent une pensée heureuse pour eux tous, aujourd'hui disséminés à travers le globe, puissent nos amitiés perdurer !

Merci aux membres du jury Chaouqi Misbah, Anaël Lemaître, Cécile Leduc, Giuseppe Foffi, Jean-Marc Allain, Raphaël Voituriez d'avoir apporté leur regard critique sur les premières versions du manuscrit, et ainsi contribué à sa clarification.

Enfin, merci au soutien indéfectible de ma famille, qui sans comprendre l'objet de ma thèse, aura su me soutenir en aveugle. Merci à Jessica qui illumine mes jours de son joli sourire, pareille à nul autre pour remonter le moral d'un trait d'humour tordant.

Place maintenant au plat de résistance : la thèse ! Ce manuscrit s'ouvre sur un résumé de quelques pages en français, immédiatement suivi du texte principal, en anglais... Enjoy ! ;)

Contents

Résumé en français	1
Introduction	5
1 From a whole organism to fiber networks	6
2 Fiber networks store residual stresses	12
3 Summary	18
1 A Model for residual stress in fiber networks	19
1.1 Description of actin networks	19
1.2 Mechanics of the network : system's potential energy	23
1.3 Sending parameters to infinity	29
1.4 Appendix : construction of units cells geometries	35
2 Numerical procedures	41
2.1 Energy minimisation	41
2.2 Stresses and elastic constants	42
2.3 Apply an external stress to the material	52
2.4 Code structure	53
3 Linear response in presence of residual stresses	59
3.1 Choice of geometry	59
3.2 Linear Results	62
3.3 A model to explain linear stiffening in presence of residual stresses.	65
3.4 Limits of validity of the simulations	69
3.5 Summary	74
4 Response to finite boundary strains	77
4.1 Response to non linear compression and shear	77
4.2 A model for non linear behavior on the alpha unit cell	85
4.3 Conclusion	91
5 General conclusion	93
6 Bibliography	97

Résumé en français

Les réseaux de biopolymères biologiques sont des structures qui apparaissent à différentes échelles. En effet, on rencontre ces derniers du squelette des cellules au collagène de la peau en passant par les caillots sanguins. À chacune de ces échelles les réseaux de fibres jouent un rôle mécanique important. Dans les cellules elles sont responsables des processus de la motilité cellulaire, qui permettent à la cellule de se déplacer et de se déformer. Dans la peau ces réseaux permettent une élasticité peu familière des cristaux ordonnés. Dans les caillots sanguins ils permettent la cicatrisation des plaies. Le fait de retrouver les réseaux des fibres dans de si nombreuses structures biologiques pose la question du lien entre les propriétés microscopiques des fibres et l'élasticité de leurs assemblages. Cela motive une étude multi-échelles, qui déduit le comportement des assemblages mésoscopiques de fibres de la connaissance de leur structure microscopique. Nos filaments d'intérêt -les polymères d'actine- sont bien caractérisés microscopiquement. On sait mesurer leur longueur de persistance, l'équilibre dynamique de leur polymérisation est bien compris et la structure protéique des monomères d'actine est résolue. Ces polymères peuvent interagir par le biais de protéines réticulantes, propres à rassembler plusieurs filaments en fagots parallèles ou à les ancrer à un angle fini. C'est pourquoi le processus d'auto-assemblage de l'actine en présence d'un important excès de protéines réticulantes mène à la formation d'épais fagots (d'environ 30 filaments). Ces fagots se retrouvent interconnectés au sein d'un réseau désordonné. Les filaments qui forment ces fagots stockent une importante énergie de courbure, comparable à l'énergie d'attachement des protéines réticulantes. Cette configuration est cependant stabilisée par la gêne stérique qui existe entre les filaments. Elle exhibe de fortes contraintes résiduelles, ces contraintes résiduelles ont peu été étudiées dans la littérature scientifique. Cette thèse étudie leur effet dans des réseaux bidimensionnels d'un point de vue théorique.

Chapitre 1 : Modèle

Pour aborder ce problème, le Chapitre 1 présente un modèle pour simuler la statique des réseaux de fibres. Ces réseaux sont modélisés par un réseau de fibres subdivisées en N ressorts hookéens dont l'énergie s'écrit, dans sa

forme adimensionnelle :

$$\mathcal{U}_s = \frac{\mu N}{2} \left(\ell - \frac{1}{N} \right)^2.$$

Ces ressorts sont reliés entre eux par des jonctions rigides en flexion, leur énergie s'écrit:

$$\mathcal{U}_b = 2N \sin^2\left(\frac{\phi}{2}\right).$$

Nous proposons une forme de l'énergie potentielle pour tenir compte de contraintes résiduelles dans le réseau. Chaque nœud connecté à trois autres sera appelé une fourche. Sur chaque fourche on choisit une direction de fermeture. La fourche est alors pourvue d'une rigidité angulaire sur chacun des trois angles qu'elle divise :

$$\mathcal{U}_r = 2g \sum_{i=1}^3 \sin^2\left(\frac{\delta\theta - \delta\theta_0}{2}\right),$$

Les angles étant mesurés par rapport à une configuration hexagonale dans laquelle il n'y a pas de frustration. Cette forme permet de décrire les fagots frustrés mentionnés auparavant, mais ne s'y limite pas car elle permet d'ajuster l'angle de la connexion entre les fagots à n'importe quelle valeur finie : cela permet d'étudier la frustration de façon plus générale, $\delta\theta_0$ étant le paramètre de contrôle de cette frustration. $\delta\theta_0 = 0$ revient à un système non frustré, tandis que $\delta\theta_0 \neq 0$ revient à un système frustré.

Après avoir présenté le modèle, la chapitre s'attache à en ajuster les paramètres dans un soucis de représenter fidèlement des polymères semi-flexibles, d'efficacité numérique et de minimaliste théorique.

Nous formulons des hypothèses pour délimiter le périmètre de l'étude et nous contrôlons leur pertinence.

- En particulier nous discutons la limite de polymères inextensibles, souples en courbure, conformément à des éléments de littérature sur les polymères semi-flexibles.
- Nous contrôlons aussi notre approximation de la limite continue pour les polymères
- Nous testons l'hypothèse de fourches infiniment rigides.

Cela nous mène à choisir le jeu de paramètres suivants :

- $N = 4$ (Limite "continue" d'un filament discret)
- $\mu = 1000$ (hypothèse d'inextensivité)
- $g = 1000$ (hypothèse de fourches infiniment rigides)
- Laisser $\delta\theta_0$ varier entre $-\frac{\pi}{3}$ et $\frac{2\pi}{3}$, ce qui correspond à la limite physique d'autointersection des filaments.

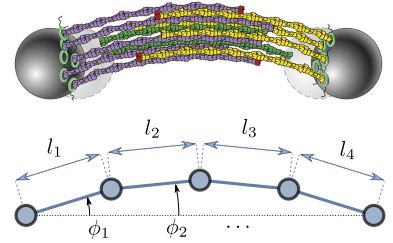


Figure 1: Un fagot d'actine est modélisé par un quatre ressorts en série reliés par des liaisons rigides.

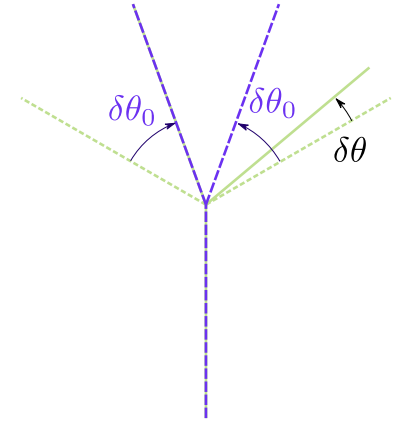


Figure 2: Les contraintes résiduelles sur une fourche sont paramétrées par rapport à la configuration au repos d'un réseau hexagonal.

Enfin, nous nous interrogeons sur la répartition des orientations des fourches. Pour cela, nous rassemblons par classe de symétrie les différents motifs qu'elles peuvent former au sein d'un réseau hexagonal. Nous concluons que quatre classes de symétrie englobent les répartitions possibles des orientations des contraintes résiduelles. Nous n'étudions donc la mécanique que d'un représentant de chacune d'entre elles. Ces représentants, qui constitueront les motifs de référence, sont étiquetés (α) , (β) , (γ) et (δ) . Cette étude préalable permet l'étude systématique des effets de la géométrie sur la mécanique des réseaux de fibres dans les chapitres ultérieurs.

Chapitre 2 : Méthodes numériques

Dans le Chapitre 2 nous introduisons les méthodes numériques utilisées pour calculer les contraintes et les modules élastiques dans les réseaux de taille finie. Plus précisément, nous discutons les limitations de la méthode classique de différences finies. Nous concluons que cette méthode manque de précision, qu'elle est chronophage, et qu'elle ne permet pas de rétrocontrôle sur la précision des résultats. Nous présentons alors une méthode originale de différentiation automatique, qui utilise des nombres hyperduaux (une généralisation de l'algèbre complexe). Cette méthode est à l'épreuve des erreurs de troncature et ne requiert pas l'ajustement manuel du pas de différentiation. À titre d'exemple, la figure 3 illustre les précisions numériques comparées entre les deux méthodes.

Dans la suite du chapitre, nous présentons la structure du code de calcul utilisé pour permettre le réemploi futur de ses éléments, notamment à l'aide d'un manuel Doxygen™.

Chapitre 3 : Réponse linéaire

Dans le Chapitre 3 nous testons la réponse linéaire des réseaux en présence de contraintes résiduelles. Cette étude se limite aux motifs de référence du premier chapitre, car nous prérelaxons les bords du système avant de calculer ses modules élastiques, or cette opération devient très chronophage lorsque le système devient trop grand. Nous découvrons que les contraintes résiduelles peuvent affecter la réponse linéaire des réseaux élastiques aussi bien en cisaillement qu'en compression, comme le montre la figure 4. Nous discutons enfin notre choix de ne nous intéresser qu'aux modules de cisaillement et de compression isotrope en analysant la perte de symétrie des motifs de référence à mesure que $|\delta\theta_0|$ évolue.

Chapitre 4 : Réponse non linéaire

Dans le chapitre 4 nous testons la réponse non linéaire des réseaux précontraints à des déformations appliquées extérieurement. Nous répétons

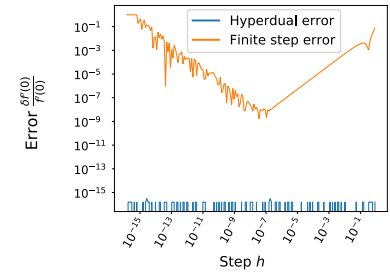


Figure 3: Précision relative des deux méthodes de dérivation numérique, sur une fonction test, échelle log-log.

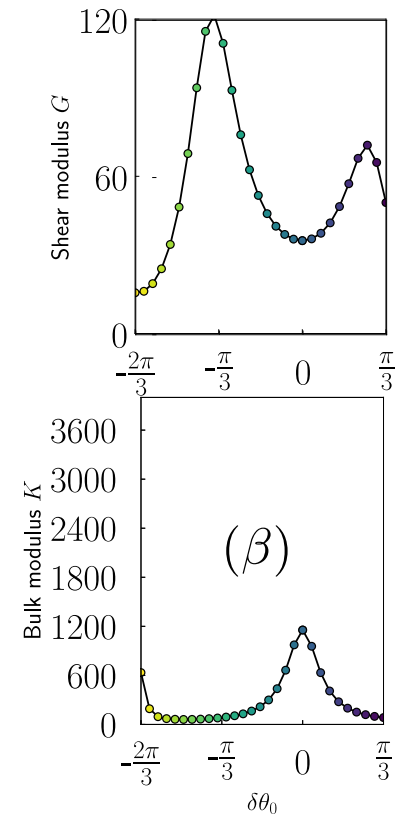


Figure 4: En haut, module de cisaillement en fonction du paramètre de contrainte résiduelle. En bas Module de compression isotrope en fonction du paramètre de contrainte résiduelle. Cas de la géométrie (β)

cette procédure en cisaillement et en compression isotrope, pour les motifs de référence et pour de petits réseaux dont les fourches sont orientées aléatoirement.

En cisaillement, nous rapportons qu'en présence de contraintes résiduelles, la réponse élastique se compose d'un régime linéaire de module élastique constant et d'un régime non linéaire où le module élastique croît linéairement avec la contrainte aux bords. La déformation critique survient plus tôt à mesure que $|\delta\theta_0|$ croît, alors que la contrainte critique augmente.

En compression, l'étude est compliquée par la présence d'instabilités mécaniques. Pour cette raison, le chapitre décrit les réseaux à la fois numériquement et analytiquement. Numériquement, nous avons essayé de compresser le network aussi progressivement que possible afin de poursuivre une courbe pression-strain continue en dépit des instabilités. Nous avons effectué ceci pour les quatre motifs de référence avec plus ou moins de succès. Néanmoins, cette étude a été instructive car elle nous a permis de conjecturer que la géométrie locale des fourche induisait tantôt une stabilisation du réseau, tantôt un effondrement local, ce qui nous a été confirmé par l'étude de réseaux aléatoires de taille modérée. Nous avons ensuite étudié analytiquement l'effondrement du motif (α) sur lequel nous avons pu réaliser un diagramme de stabilité (fig.5) pour confirmer nos observations numériques qui, seules, auraient été peu probantes.

Conclusion

Cette thèse apporte quatre contributions principales.

- La première d'entre elles est une nouvelle procédure pour calculer des quantités élastiques différentielles autour d'une configuration donnée du réseau. Elle peut aussi être utilisée pour calculer précisément les forces et la matrice des raideurs locales d'un système de particules sans se perdre dans un calcul de dérivées analytiques.
- La seconde contribution est que les contraintes résiduelles peuvent aussi bien rigidifier que ramollir la réponse d'un réseau autour de sa configuration au repos.
- La troisième est que les contraintes résiduelles peuvent ajuster le seuil d'apparition des non linéarités dans la réponse des réseaux de fibres à une déformation non linéaire.
- La quatrième est que les contraintes résiduelles induisent des effondrements locaux des réseaux lors d'une compression isotrope. Nous avons prouvé analytiquement que ces effondrements surviennent pour certaines géométries des précontraintes. Cependant nous n'avons pas caractérisé totalement le devenir de ces effondrements en présence d'interactions de contact entre filaments car cela sort du cadre de nos modèles.

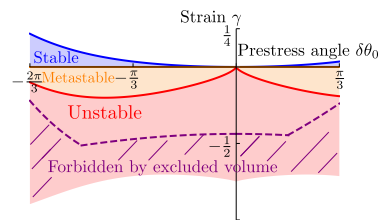


Figure 5: Diagramme de stabilité de la géométrie (α) en fonction du paramètre de contrainte résiduelle.

Introduction

Scientists ask questions to the surrounding world through observation, and they end up with models to explain it. In physics, we can develop models with two goals in mind : being quantitatively accurate to make predictions, or being qualitatively accurate to understand phenomena beyond the reach of experiments. The first way of doing is fruitful to design systems of increasing performance in engineering for instance. The second is fruitful when doing to identify important features of a system in research for instance. Sometimes, a family of models share similarities, which allow to find an unifying rule governing the family of phenomena they describe. During the last century the advent of quantum physics and general relativity provided physics with very universal fundamentals. These theories pushed the limits of models beyond the borders of experiments, to such an extent that the discovery of new phenomena nowadays requires international collaborations and result in global mediatisation, way beyond academic borders as was the case for the discovery of the Higgs bosons, for the release of the all-sky map of the Cosmological Microwave Background or for the observation of gravitational waves. On the other hand, biology experiments remain human-sized and new phenomena get discovered every day. Nonetheless, biology doesn't lack of foundational principles : in the *XVIIth* century, cells were discovered, in the late 60's DNA was first observed, and I think that the microscopies of today are good candidates for revolutions to come thanks to the fruitful collaboration between biologists and physicists.

Indeed, the new microscopies push away the boundaries of the observable living world : confocal microscopy allows 3D imaging of microscopic samples, optical tweezers allows to manipulate micron-sized dielectric objects, automatic tracking of diffusing particles allows for the statistical characterisation of the motion of biological objects, atomic force microscopy allows the observation of nanometric objects, magnetic resonance imaging enables in vivo observation of organs etc... All these new methods contribute to improve the spatiotemporal resolution of experiments. This improved precision allows to elaborate quantitative mathematical models in biology. These models export the dramatic predictive power of physics to biology. This thesis is written in a period when the main questions in biology lie on the edges of resolution of microscopies. The collaboration between physicists and biologists is thus

required to elaborate models across scales, which propose microscopic mechanisms to explain mesoscopic behaviours. I believe that these models are a valuable approach to understand the objects of soft matter.

This introduction chapter goes from general aspects in cell biology to the very topic of the thesis. It is articulated around three sections that approach the topic of the thesis from macroscopic scales to microscopic scales. The section 1 gives motivations to study cells by going from macroscopic organisms to cells, to fiber networks. This allows to highlight the interplay between developments in physics and observations in biology across centuries. The section 2 provides informations about the fiber networks that we study, including orders of magnitude for the actin networks we have in mind, these orders of magnitude are the foundational basis for the approximations of the thesis. finally, section 3 formulates a manageable question for the study of residual stress, and announces the structure of the thesis as a way to answer it.

1 From a whole organism to fiber networks

According to the encyclopedia britannica, biology is the science that studies living organisms and their vital processes. It provides tools of thought to address questions about living beings. According to us, two majors discoveries in biology provided unifying principles in biology : the discovery of cells and the discovery of DNA. In this paragraph, we underline the interplay between these discoveries and developments in physics.

Cells have been observed for the very first time by Robert Hooke in 1665¹. Actually, with the optical resolution of his microscope at this time, Hooke merely observed cellular walls in plant samples. However, he gave their name to "cells" and introduced the new concept of minimal block required for life to exist. This was a major step towards universal principles in biology and induced a frenesy of observations of plants under a microscope. The idea that all plants were made of cells became accepted as observations confirmed it over and over.

With the early microscopes in use at that period. Two limitations were to overcome to access the micron-scales : diffraction of light through glass, and spherical aberrations². The first issue was solved by John Dollond, upon Hall's idea, in 1757³. The second one was solved with the commercialisation of the first apochromatic triplet of lenses in 1886, thanks to the partnership of Abbe, Zeiss and Schott .

For this reason it took almost two centuries before the advent of the cellular theory in 1858 by Rudolf Virchow in ref ⁴. This theory presents cells as fundamental units of life, be it animal or vegetal, it obeys the following principles :

- All living organisms are composed of one or more cells.
- The cell is the basic unit of structure and organisation in organisms.

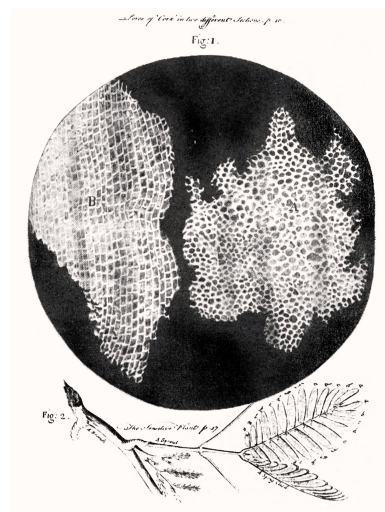


Figure 6: Historic observation of cell walls of plants by Robert Hooke. From *Micrographia*, 1665

¹ R. Hooke, J. Allestry, and J. Martyn. *Micrographia, or, Some physiological descriptions of minute bodies made by magnifying glasses : with observations and inquiries thereupon*. London :Printed by Jo. Martyn and Ja. Allestry, printers to the Royal Society ..., 1665

² J.-F. Bruch, D. Sizaret, A. Brault, F. Tabareau-Delalande, and F. Maître. Étude historique du microscope optique : Des premières lentilles du XVIIe siècle aux techniques de super-résolution et de lecture automatisée. *Revue Francophone des Laboratoires*, Jan. 2015

³ J. Dollond and J. Short. Xcviii. an account of some experiments concerning the different refrangibility of light. by mr. john dollond. with a letter from james short, m. a. f. r. s. acad. reg. suec. soc. *Philosophical Transactions of the Royal Society of London*, 1757 <https://www.zeiss.fr/microscopie/a-propos-de-nous/histoire.html>

⁴ R. Virchow. *Die cellularpathologie in ihrer begründung auf physiologische und pathologische gewebelehre*. Berlin, A. Hirschwald, 1858, 1858. Théorie cellulaire

- Cells arise from pre-existing cells.

Tableau I – Évolution des lentilles du microscope.			
Siècle / Date	Matériel(s)	Figure(s) emblématique(s)	Propriétés
Début 17 ^e	Lentilles de verre	Leeuwenhoek	Grossissement par réfraction
18 ^e	Lentilles achromatiques	Dolland / Douglas	Correction des aberrations chromatiques (rouges et bleues) dues à la dispersion
19 ^e	Apochromatique	Zeiss / Abbe / Schott	Correction des aberrations chromatiques (trois couleurs) et sphériques ; augmentation de l'ouverture numérique (ON) augmentant la résolution
Années 50	Anneau et plateau de phase	Zernike	Rendre visible les modifications de phase de la lumière (cellules vivantes non colorées)
Années 60	Idem avec polariseur et interféromètre	Nomarsky	Modifications subtiles de phase et de structure (exemple : visualisation de défaut des spermatozoïdes)
Années 70	Objectifs à l'infini		Permettent une observation confortable sans accommodation
Années 90	Objectifs « 4p »	Hell	Augmentation de l'angle d'ouverture numérique par utilisation de deux objectifs « tête-bêche »
1995	APO-TIRF		Recueil d'ondes évanescentes dans le champ proche par réflexion totale interne (TIRF) possible grâce à un objectif à très grande ouverture (ON > 1,45)
2000-2005	Superlentille	Pendry	Recueil d'ondes évanescentes dans le champ proche par réfraction négative
2007-2010 et suivantes	Hyperlentille Métalentille	Liu & Zhang ; Smolyaninov	Recueil d'ondes évanescentes devenues propagatives dans le champ lointain par réfraction négative et résonance plasmonique

Since the cell theory, the study of cells for themselves became a field of biology in itself called *cell biology*. This field deciphers the structure and function of cells, this thesis contributes to this field as it studies the cellular skeleton from a mechanical viewpoint. The goal of this section is to present a few of the cellular functions, called *cellular motility*. This will enable to understand the importance of studying fiber networks which play a major role in motility.

We do this in two parts : the first part presents the motility mechanisms in cells. The second part presents cytoskeleton and describes the central it plays in these mechanisms.

1.1 Cell Motility

Organisms are assemblies of cells, which result from the successive divisions of an original cell, the simplest are unicellular like bacterias, the biggest known on earth weights around 6000 tons, it is a forest called Pando, made of an unique tree that lives in Utah. The mass of a cell being around 10^{-12} kg, this single organism contains 10^{15} cells.

The DNA, which codes for the synthesis of proteins into genes, is conserved through the stages of divisions is henceforth characteristic of the individual. DNA may be expressed in a different phenotype in the different

Figure 7: Table of the technological breakthroughs that pushed away the limits of observable world. From *Bruch et al.*, 2015



Figure 8: The Axolotl has a faculty to recover from cut members : a dramatic example of cell differentiation in adult organisms. Picture from *Regrow Like An Axolotl*, Science *Beverly A. Purnell*, 2017

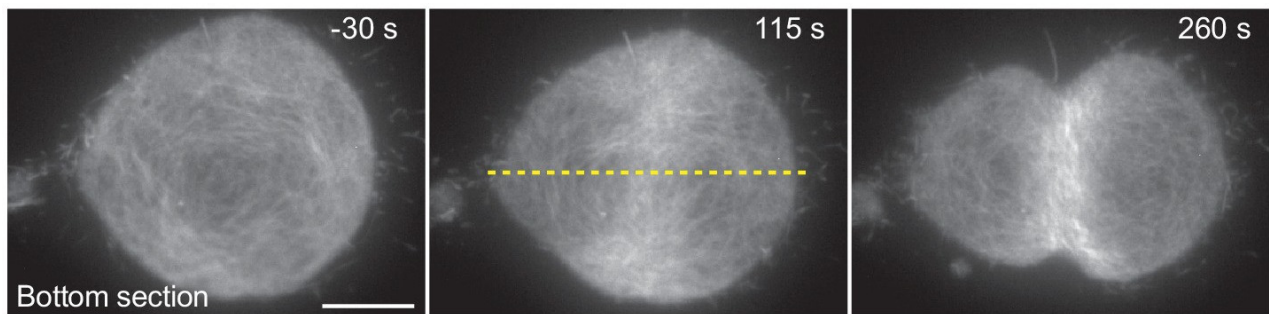
cells of an organism, depending of the surrounding of these cells. For example a stem cell, laid on top of substrates of different stiffnesses, mimicking different organs, may specialise into different phenotypic types⁵. This differentiation is not a reversible process in most organisms, nonetheless certain organisms like the axolotl figure 8 have cells able to differentiate into eye or brain cells after an injury even at adult age as reported in ref⁶.

These differences in gene expression allow cells to fill a wide variety of biological functions : they can form tissues, bones, immune cells, blood cells, spermatozoa etc... These many specialisations lead to many biological processes, some of them being common to all phenotypic types of cells, some specific to some !

Cells are able to regulate their shape, to divide or to exert stress on their surrounding. These processes involve the cytoskeleton, an architecture of filaments such as actin that we will describe section 1.2. Before, we present a non exhaustive list of mechanical processes in which cells participate. This presentation motivates the study of actin networks that we do in throughout the thesis.

Cell division

All eukaryotic cells divide, and the single division mechanism that preserves DNA is called *mitosis*. On the last stages of the division, cell undergo the *cytokinesis* (from Greek κύτος -kytos, a hollow- and Latin derivative cyto-cellular- (Wikipedia)). During this process, a contractile ring made of actin polymers and myosin molecular motors is formed in the middle of the cell and its contraction leads to a split⁷, as shown on figure 9, adapted from ref⁸.



⁵ A. J. Engler, S. Sen, H. L. Sweeney, and D. E. Discher. Matrix Elasticity Directs Stem Cell Lineage Specification. *Cell*, Aug. 2006

⁶ B. A. Purnell. Regrow like an axolotl. *Science*, 2017

⁷ G. T. Risa, F. Hurtig, S. Bray, A. E. Hafner, L. Harker-Kirschneck, P. Faull, C. Davis, D. Papatziadou, D. R. Mutavchiev, C. Fan, L. Meneguello, A. A. Pulschen, G. Dey, S. Culley, M. Kilkenny, L. Pellegrini, R. A. M. de Bruin, R. Henriques, A. P. Snijders, A. Šarić, A.-C. Lindås, N. Robinson, and B. Baum. Proteasome-mediated protein degradation resets the cell division cycle and triggers ESCRT-III-mediated cytokinesis in an archaeon. preprint, *Cell Biology*, Sept. 2019

⁸ F. Spira, S. Cuylen-Haering, S. Mehta, M. Samwer, A. Reversat, A. Verma, R. Oldenbourg, M. Sixt, and D. W. Gerlich. Cytokinesis in vertebrate cells initiates by contraction of an equatorial actomyosin network composed of randomly oriented filaments. *eLife*, Nov. 2017

Amoeboid motion, pseudopodium

Some cell types are able to move, this is the case of unicellular organisms like amoeboid cells. These cells deploy locomotory appendages, called pseudopodia, to propel themselves to their target, however the precise mechanism is not fully elucidated as two theories are plausible in⁹ (actin driven motility, involving parallel bundles of actin) and¹⁰ (bleb driven motility involving the formation of a membrane bleb, without reorganisation in the actin cortex). This type of motion enables these cells to find very efficiently

Figure 9: Total internal reflection fluorescence (TIRF) microscopy of hTERT-RPE-1 under confinement stably expressing LifeAct-mCherry. Adapted from Spira *et al.*, 2017.

nutrients.

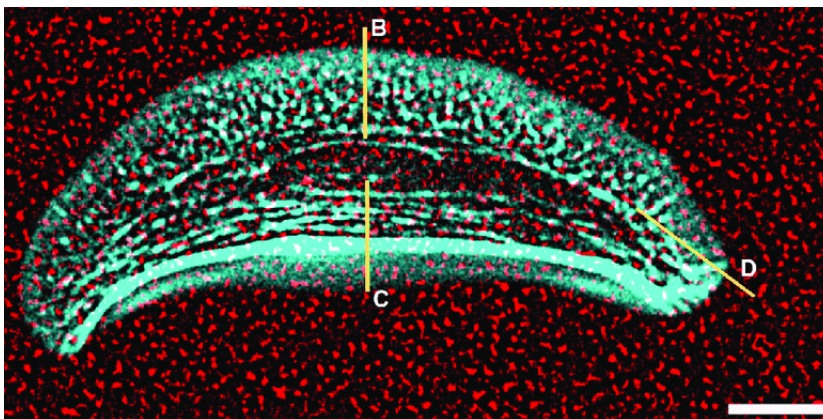


Figure 10: Chaos carolinense, an amoeboid having lobopodia (a type of pseudopodia). From <https://en.wikipedia.org/wiki/Pseudopodia>

Phagocytosis of micron-size targets

Phagocytes are able to wrap around micron-size targets and perform endocytosis. These dramatic deformation of cells are possible only through active deformation of their membrane. It was observed recently in ref¹¹.

Keratocyte's motion Keratocytes are able to propel them self over a surface through a strong organisation of actin inside cells into a lamellipodium. In this structure, actin is organised on the front of the cell, and disorganised back the cell. A moving keratocyte is represented figure 11 from reference¹².



¹¹ M. V. Baranov, R. A. Olea, and G. van den Bogaart. Chasing Uptake: Super-Resolution Microscopy in Endocytosis and Phagocytosis. *Trends in Cell Biology*, Sept. 2019

¹² M. E. Fournier, R. Sauser, D. Ambrosi, J.-J. Meister, and A. B. Verkhovsky. Force transmission in migrating cells. *The Journal of Cell Biology*, 188, Jan. 2010

Figure 11: Simultaneous observation of actin motion and substrate deformation in migrating keratocytes. The image of phalloidin-labeled actin (cyan) is superimposed on the image of the fluorescent beads (red) spread on the substrate surface. Scale bar 10 μm .

1.2 Cell architecture : Major role of cytoskeleton in cells

All the mechanisms mentioned above require adaptations of the cytoskeleton. This part presents cytoskeleton and the filaments it is built of. These filaments are microtubules, intermediate filaments and filamentous actin (F-actin). All these are polymers, nonetheless they are of a very different mechanical nature as microtubules are really stiff inextensible polymers, actin filaments are semiflexible at cellular scale inextensible, and intermediate filaments can bear hundred percents of extensile strain¹³.

These filaments carry out several functions in cells. First of all microtubules are polar filaments that help transport molecular cargos from membrane to nucleus¹⁴. They form tracks for chromosomes during cell division in the mitotic spindle and build up flagellas in spermatozoa, to cilia in the respiratory epithelium. Secondly actin filaments are polar filaments that operate in conjunction with cross-linking proteins : they form disordered meshes in the actin cortex, parallel bundles in the lamellipodium of keratocytes, they lead to a cytokinetic ring during mytosis. For these reasons the actin cortex is a regulator of the cells surface properties, it can change cells shape, stiffness, induce division of them and propel them. Finally, intermediate filaments doesn't participate in motility processes, they play a structural role to reinforce cells when they form tissues.

We observe a fluorescence cliché of the cytoskeleton in figure 13, the inner part of cells is spanned by the *cytoskeleton*, ranging from cell membrane to nucleus membrane. From nucleus to cell membrane we see the microtubules, disposed radially. On the periphery of cells we can see actin cortex, a disordered network containing actin filaments, connected to the cell membrane, we do not see intermediate filaments.

From now on, we will leave appart leave appart intermediate filaments and microtubules and focus our interest into actin structures. Actin cortex displays structures made of actin with very different properties : they range from visco-elastic structures to stiff bundles, passing through soft elastic meshes.

These structures are diverse by the level of ordering of their fibers, by the average connectivity of the meshes of their members, by the cross-linkers into play as depicted in figure 12, from ref¹⁵. Connectivity is known to affect the stiffness of a network, cross-linkers can induce the storage of residual stresses as we will see in next section. The physics models that study fiber networks require the knowledge of the underlying microscopic constituent. For this reason, the next section describes the experiments that were performed to characterise actin polymers at a microscopic scale, it will also provide the orders of magnitude that will guide us in building the model of chapter 1 for the study of residual stress in use throughout this thesis.

¹³ H. Herrmann, H. Bär, L. Kreplak, S. V. Strelkov, and U. Aebi. Intermediate filaments: from cell architecture to nanomechanics. *Nature Reviews Molecular Cell Biology*, July 2007

¹⁴ M. A. Welte. Bidirectional Transport along Microtubules. *Current Biology*, July 2004

¹⁵ L. Blanchoin, R. Boujemaa-Paterski, C. Sykes, and J. Plastino. Actin Dynamics, Architecture, and Mechanics in Cell Motility. *Physiological Reviews*, Jan. 2014

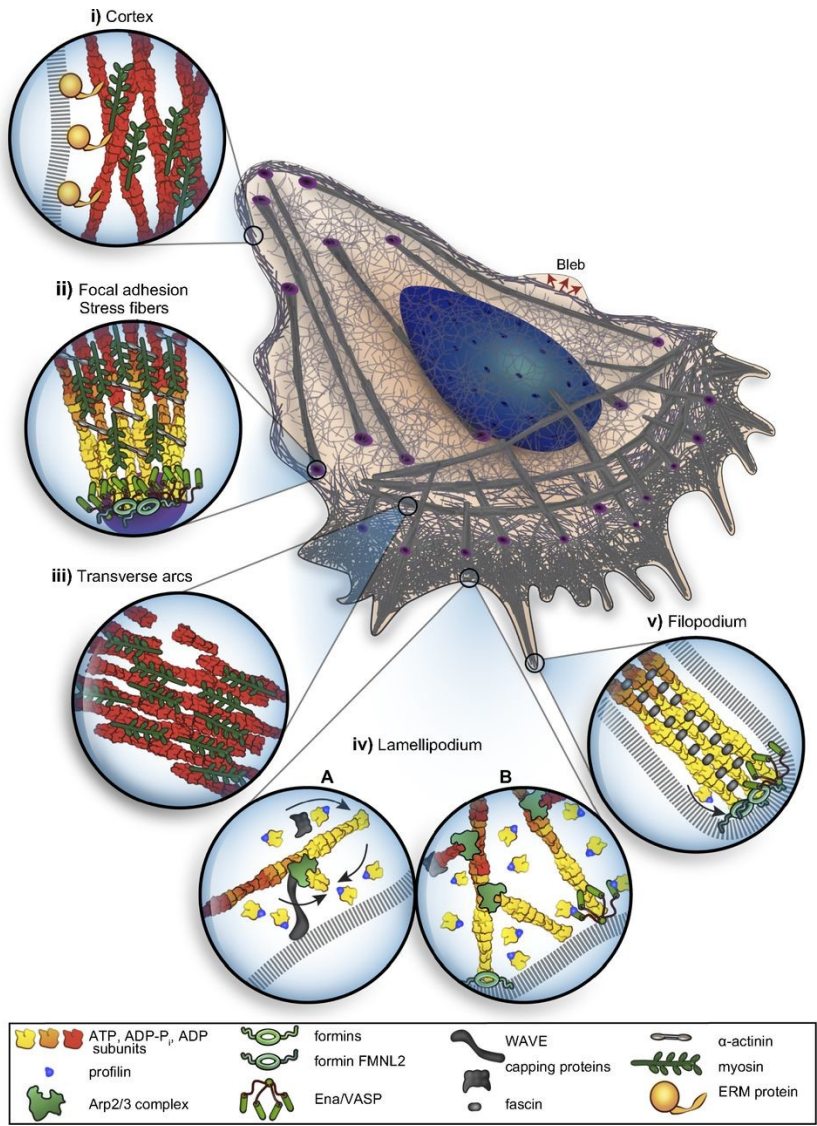


Figure 12: Cytoskeleton make use of fiber networks for motility. From Blanchoin et al. 2014

2 Fiber networks store residual stresses

In the previous section, we have seen that mechanisms of cell motility involved actin networks. In this section we present actin filaments and give quantitative measurements that have been performed to characterise them, then we show that their interactions can lead to large residual stresses in self-assembled network.

2.1 Characterisation of actin filaments

Actin filaments are double helicoidal polymers with a monomer diameter of around 5.4 nm¹⁶, this results into filaments that are approximately 9 nm in diameter, as we understand in figure 14. At room temperature these filaments are subject to non negligible fluctuations, as you can see on the timelapse 15 from ¹⁷.

The average length of these filaments results from an steady state between polymerisation and depolymerisation ¹⁸. We can characterise the fluctuations in orientation by studying correlations on tangent vectors $\vec{t}(s)$ along the filament's arc length s of a polymer. In average, if the polymer is in solution at equilibrium, it behaves as :

$$\langle \vec{t}(0) \cdot \vec{t}(s) \rangle \propto e^{-\frac{s}{\ell_p}}$$

which defines the persistence length ℓ_p of the filament. For actin filaments, it measures 10 μm ¹⁹. This measurement, when compared to typical sizes of animal cells 50 μm , allows to classify actin networks in cells amongst semi-flexible networks, which means that actin polymers play the role of elastic rods that we can bend at a moderate energy cost.

An important property of semiflexible filaments is their entropic stretching stiffness. Indeed, when filaments are fixed at an end-to-end length of ξ , they are able to fluctuate. These fluctuations must fulfill the constraint of having a fixed total arc length L , the rest length of the filament, considered inextensible. We can count all the paths of length L with an end-to-end vector of imposed length ξ to see that low ξ states are entropically favoured, on the contrary, for $\xi = L$, we just have one configuration possible. However, low ξ states involve bending of the filament, and are energetically penalised. As a consequence, if we let a filament equilibrate in contact with a thermal bath at finite temperature, it will reach an average length L_0 . If we further apply a force to its ends, we can compute - in the limits of the worm-like chain model - an average force-extension relation. The result is that the polymer behaves as a non linear spring ²⁰. The linear limit of this spring has a stiffness scaling with $\frac{k_b T \ell_p^2}{\xi^4}$. For semi-flexible polymer networks, which are cross-linked at an average distance $\xi \ll \ell_p$. As a result, the stretching stiffness of

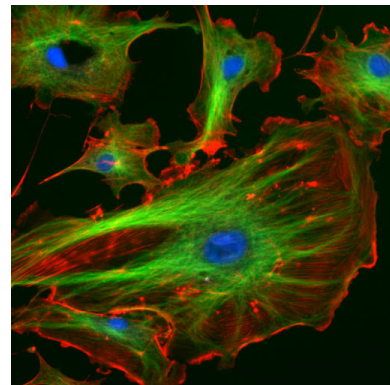


Figure 13: Cytoskeleton of a cell, this architecture is made of actin cortex on the outer layer (in red), microtubules that span radially (in green), and intermediate filaments that we don't see here. From <http://rsb.info.nih.gov/ij/images/>.



Figure 14: Double stranded actin filament, if globular actin has a diameter of 5.4nm, the filament is 9nm in diameter.

¹⁶ P. Moore, H. Huxley, and D. DeRosier. Three-dimensional reconstruction of f-actin, thin filaments and decorated thin filaments. *Journal of Molecular Biology*, 1970

¹⁷ H. Isambert, P. Venier, A. Maggs, A. Fat-toum, R. Kassab, D. Pantaloni, and M. Carlier. Flexibility of actin filaments derived from thermal fluctuations. effect of bound nucleotide, phalloidin, and muscle regulatory proteins. *Journal of Biological Chemistry*, 1995

¹⁸ B. Alberts, A. Johnson, J. Lewis, D. Morgan, M. Raff, K. Roberts, P. Walter, J. Wilson, and T. Hunt. *Molecular biology of the cell*. Garland Science, Taylor and Francis Group, New York, NY, sixth edition edition, 2015. OCLC: ocn887605755

¹⁹ A. Ott, M. Magnasco, A. Simon, and A. Libchaber. Measurement of the persistence length of polymerized actin using fluorescence microscopy. *Phys. Rev. E*, Sep 1993

²⁰ A. V. Dobrynin, J.-M. Y. Carrillo, and M. Rubinstein. Chains Are More Flexible Under Tension. *Macromolecules*, Nov. 2010

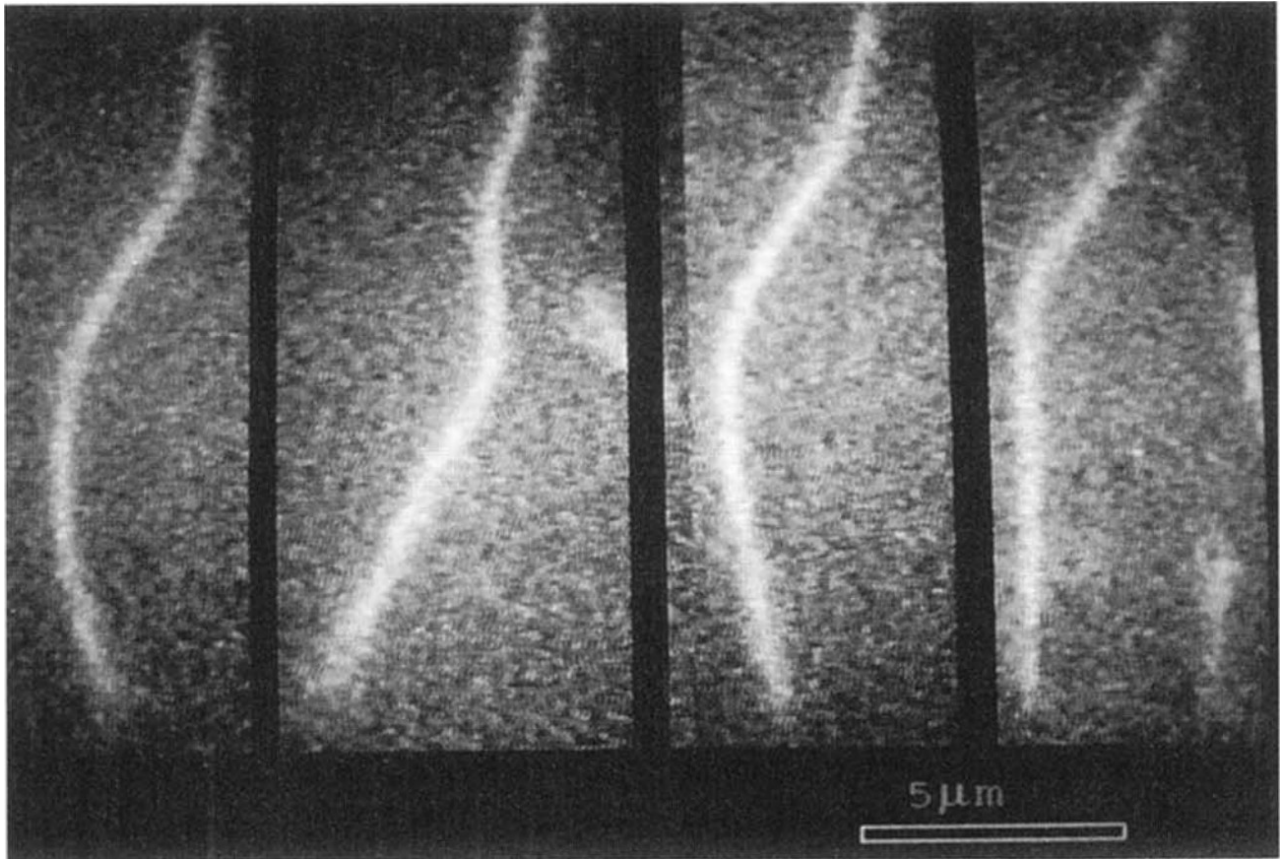


Figure 15: Actin filament fluctuating at room temperature, from Isambert et al. 1995

bending a filament on its first mode is orders of magnitude smaller than the one required to bend it by fluctuating on the higher orders modes.

In the above paragraphs we learned about the properties of single actin filaments, however, these filaments are able to form structures ranging from disordered meshes to parallel bundles of several filaments. The protagonists of these structures are cross-linking proteins, which mediate binding between filaments. The figure 16 gives an idea of the families of crosslinkers and their function. Some of them are able to bind actin to other proteins, some of them bind actin to its siblings, but can do it in various ways : indeed they can be sensitive to polarity in actin filaments, they can impose an angle between neighbours or simply introduce anchoring points. To be more precise the dystrophin binds plasma membrane to the cytoskeleton²¹. Fascin is a crosslinker that can gather actin into either parallel-bundles or meshes. α -actinin is able to gather both parallel and antiparallel²², forming either a mesh or bundles. Filamin is able to gather filaments between each other into a mesh.

²¹ Q. Q. Gao and E. M. McNally. The Dystrophin Complex: Structure, Function, and Implications for Therapy. In R. Terjung, editor, *Comprehensive Physiology*. John Wiley & Sons, Inc., Hoboken, NJ, USA, June 2015

²² B. Sjöblom, A. Salmazo, and K. Djinović-Carugo. α -actinin structure and regulation. *Cellular and Molecular Life Sciences*, May 2008

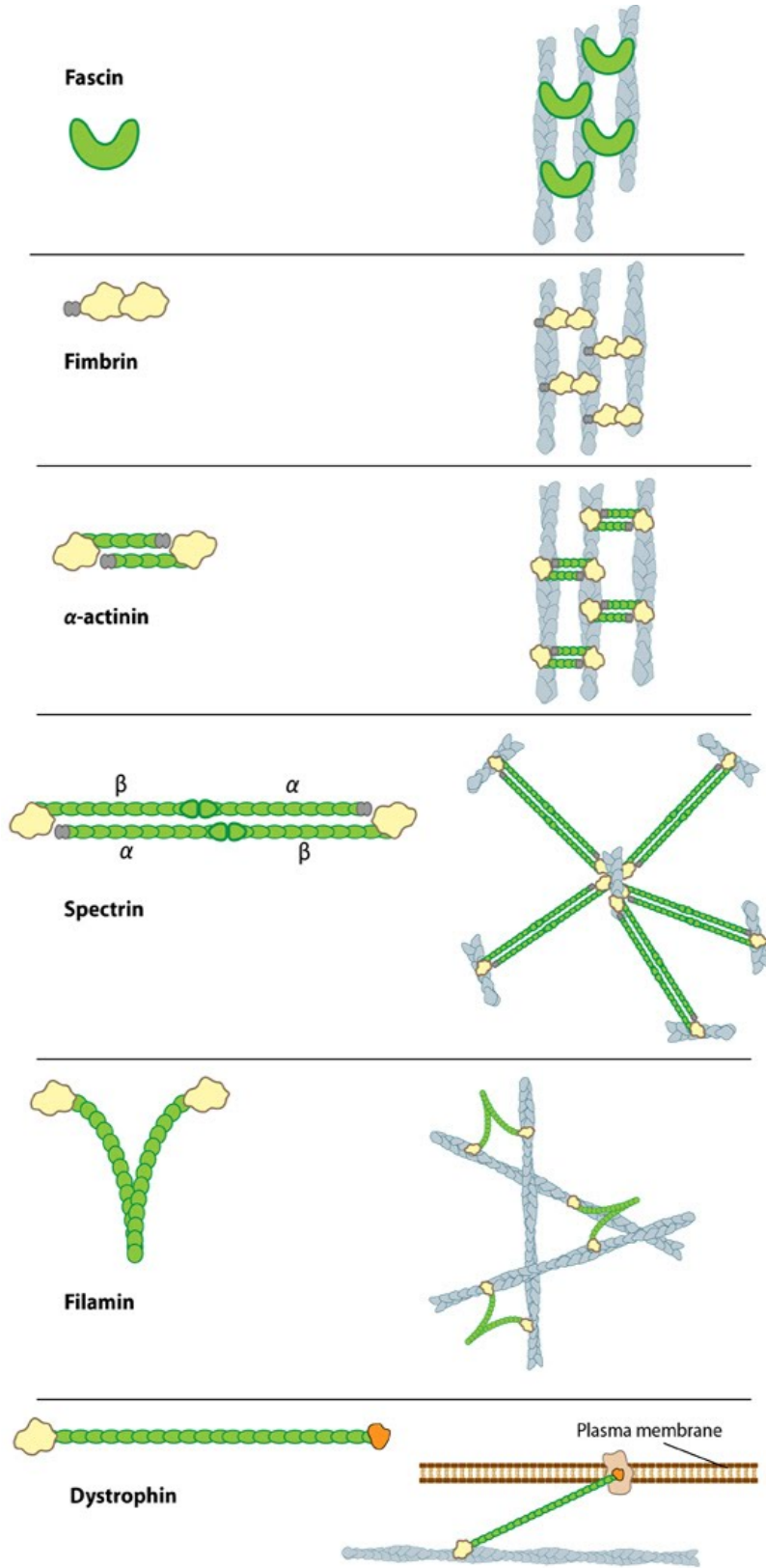


Figure 16: Types of actin crosslinkers, from <https://www.mechanobio.info/cytoskeleton-dynamics/actin-crosslinking/>

The possibility for cross-linkers to gather filaments into bundles makes us wonder how the features presented above - namely bending stiffness and stretching stiffness - are affected by cross-linking. The answer again depends on the type of cross-linkers, however there are models to understand their physics. By explicitly modeling bundles as assemblies of filaments that can slide relative to each other to the price of cross-linkers extensions (fig 17), we can compute that the bending stiffness of a bundle depends on the cross-linkers, it ranges between $N\kappa$ for unsharable bundles to $N^2\kappa$ for sliding bundles, where N is the number of filaments in one bundle, and κ the bending stiffness of one filament²³. A third regime is possible for intermediate cases, where internal deformation induce a wave-length dependant shearing stiffness. For the entropic stretching stiffness, the phenomenology is simpler as the corresponding stiffness scales with N^2 in all cases. Some measurement confirm these models, these results are in agreement with measurements in ref²⁴ (weakly coupled case), their experiment is sketch in fig 18.

Up to now, we merely indicated the behaviour of single bundles. Next subsection explains how they induce residual stresses into fiber networks.

2.2 Origin of residual stress

The previous section considered single actin filaments on one side and single actin bundles on the other side. In particular, we didn't consider interactions between bundles. However the self assembled nature of biological networks induce actin bundling nature of actin depending on the amount of available cross-linkers during growth.

Some experiments were designed to observe the self assembly process of actin monomers, in presence of cross-linkers and ATP *in vitro*^{25,26,27}. These experiments are able to reproduce a wide variety of actin networks, ranging from a mesh of thin actin filaments to a network of thick bundles of around 30 filaments each, by tuning a single parameter : the cross-linkers concentration. These networks display rich rheological properties which can be measured by observing the diffusion of polystyrene beads in the network. We display confocal microscopy pictures of the different types of networks we can obtain from non bundled to bundled ones in figure 19.

A mechanism for this phenomenology has been proposed. It invokes in the kinetic trapping of actin polymers into the network as filaments get too large. There is a competition between diffusion of filaments, bundling and steric hindrance of them²⁸.

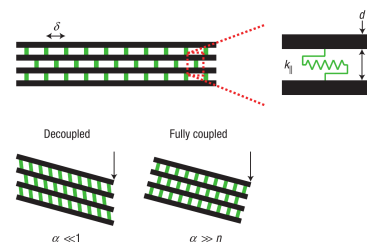


Figure 17: A model of sliding bundles, with elastic cross-linkers relates the bending mechanics of bundles to that of single filaments. From Claessens et al. 2006

²³ C. Heussinger, M. Bathe, and E. Frey. Statistical Mechanics of Semiflexible Bundles of Wormlike Polymer Chains. *Physical Review Letters*, July 2007

²⁴ F. R uckerl, M. Lenz, T. Betz, J. Manzi, J.-L. Martiel, M. Safouane, R. Paterski-Boujema, L. Blanchoin, and C. Sykes. Adaptive Response of Actin Bundles under Mechanical Stress

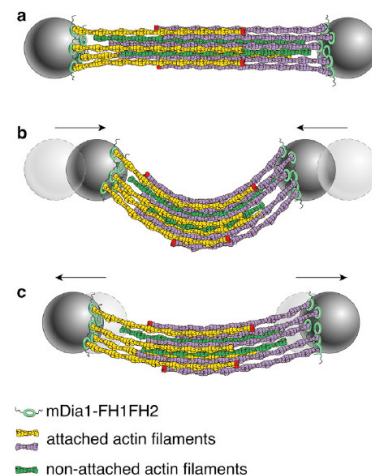


Figure 18: This experiments treats the surface of polystyrene beads for bundles to polymerize. It becomes then possible to study their adptive response under mechanical stress. From R uckerl et al. Adaptive Response of Actin Bundles under Mechanical stress

²⁵ T. T. Falzone, M. Lenz, D. R. Kovar, and M. L. Gardel. Assembly kinetics determine the architecture of α -actinin crosslinked F-actin networks. *Nature Communications*, Jan. 2012

²⁶ C. Pelzl, K. D urre, and A. Bausch. Reconstituted active actin networks in confinement. *Biophysical Journal*, 106, 01 2014

²⁷ J. Deek, R. Maan, E. Loiseau, and A. Bausch. Reconstitution of composite actin and keratin networks in vesicles. *Soft Matter*, 14, 02 2018

²⁸ G. Foffano, N. Levernier, and M. Lenz. The dynamics of filament assembly define cytoskeletal network morphology. *Nature Communications*, Dec. 2016

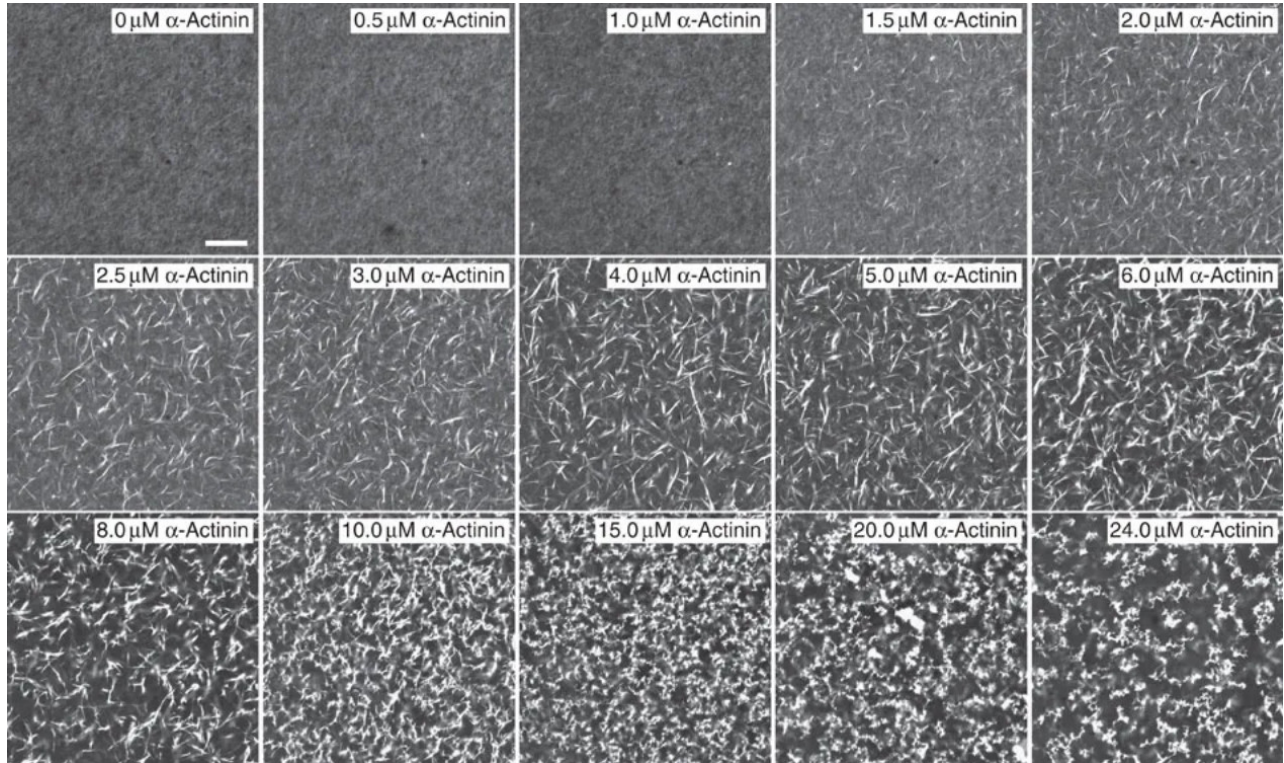


Figure 19: Self-assembly of actin monomers in the presence of α -actinin, quenched by phalloidin 60 min after polymerization was initiated by the addition of salts. As α -actinin concentration is increased, the network architecture changes from single-filament meshwork ($c_{\alpha} = 0-1.0 \mu\text{M}$) to a composite network ($c_{\alpha} = 1.5-3 \mu\text{M}$), to a network of bundles ($c_{\alpha} = 4-10 \mu\text{M}$), to a network that appears to be composed of very short and bright bundles of actin ($c_{\alpha} \leq 10 \mu\text{M}$). Scale bar = $30 \mu\text{m}$ from *Falzone et al.*

This kinetic trapping suggests the existence of residual stresses in the network. In this thesis, when we will talk about residual stress in a network, this would mean forces compensated at a local scale between filaments.

We will now explain how residual stress emerge. During the self assembly process of the network, filament get bundled, but at the same time they diffuse. As a result, the orientations of the bundles get distributed in all directions, up to the point where two bundles arrive in contact with each other. These contacts enhance the probability for cross-linkers to attach bundles together. An other thing that can happen is that two partial bundles get attached parallel to each other at one end, and get stochastically zipped towards the other by cross-linkers. During this zipping mechanism, the two parts of the bundle being zipped can get sterically trapped in the network. The cross-linkers will continue to zip the bundle, up to the point where fighting against steric hindrance becomes too costly from an energetic viewpoint. As a result, we end up with a network containing objects like the in figure 20. These objects in which a bundle of $n + m$ filaments splits into one bundle of n filaments and an other one of m filaments will be referred to as *forks* in this thesis. Forks inherit their stiffness from a combination of the individual bending stiffnesses of constitutive filaments and the forces

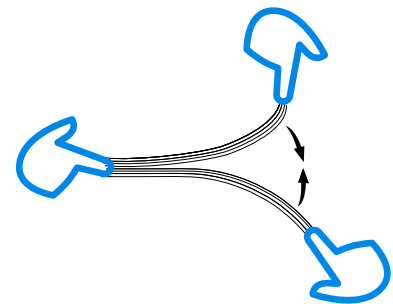


Figure 20: Cartoon of a fork. It represents the microscopic structure of two bundles of size 4 zipping into one of size 8 in presence of boundary constraints. The hands represent the anchoring points that are imposed by the rest of the network during its self assembly process.

exerted by cross-linkers between its two halves. Because the unbinding of cross-linkers is energetically costly, forks exert residual stresses in the network. These residual stresses, even if they do not induce boundary stress, may affect elastic response of the network, for instance through its elastic moduli.

The goal of this thesis is to study the effect of residual stresses on the mechanics of fiber networks.

3 Summary

This introduction teaches that fiber networks are ubiquitous in cells, they are at the origin of mechanical structures ranging from very stiff non-dissipative rods to viscoelastic mesh passing through contractile force transmissive rings. These networks self-assemble and this self-assembly has been experimentally reproduced. Depending on the rates of cross-linkers they contain, fiber networks can end up trapped into highly bundled states, storing important residual stresses. However, the effect of residual stresses in bundled networks has not much been studied up to now.

In this thesis we ask the following question :

WHAT IS THE EFFECT OF RESIDUAL STRESS ON SEMIFLEXIBLE POLYMER NETWORKS ?

We answer to it from a numerical perspective, on 2 dimensional networks. Namely we develop four chapters :

- Chapter 1 introduces a model for fiber network and defines notations.
- Chapter 2 explains our computational methods, including an original algorithm to numerically compute elastic moduli.
- Chapter 3 gives elements about the effect of residual stresses on the linear response of fiber networks.
- Chapter 4 gives elements about the effect of residual stresses on the non-linear response of actin networks.
- Finally, a conclusion sums up the important points of the thesis.

1

A Model for residual stress in fiber networks

This chapter describes the model for fiber networks that we use. In section 1.1 we talk about the physical description of fiber networks, in section 1.2 describe the sources of its motion. In section 1.3 we explain how we tuned the adjustable parameters of the model, finally in section 1.3 we explain how to get rid of some parameters by sending them to infinity or by taking a continuous limit. We conclude this chapter by giving a few examples of equilibrium geometries.

1.1 Description of actin networks

In this section we tackle the issue of modelling fiber networks, regardless of the forces that act on it, since a section is devoted to it more specifically. We need to make this discussion unambiguous so as to build mathematical tools that enable numerical simulations. The presented model leads to approximations that we will explicitly discuss. Sometimes, the developed formalism can look overwhelming, the reader should then recall that it only refers to the memory structures in use in our simulations for a non redundant storage of information and an efficient computation of energies.

1.1.1 Topology of fiber networks

When we think about a fiber network, we think of a set of points connected assembled in pairs by links. The mathematical structure of a *graph* is especially in line with this idea : the data of a set of objects \mathcal{P} together with that of a set of edges $\mathcal{E} \in \mathcal{P} \times \mathcal{P}$, which are pairs of points are enough to define such a graph.¹

With this definition we are able to describe the topology of the network by saying which point is connected to which other point, but still unable to encompass its structure in space. In order to do this we need to be more specific with the set of points \mathcal{P} : we chose $\mathcal{P} = \mathbb{R}^d$, where d is the space dimension. This endows naturally edges with a set of vectors thanks to the vector structure of \mathbb{R}^d . We end up with a structure that associates a vector to

¹ Example : if we take $\mathcal{P} = \{1,2\}$ and $\mathcal{E} = \{(1,2)\}$, we define a network with two points labeled 1 and 2 and one link between them.

each point and to each edge in the graph.

For reasons of convenience we label the vectors in \mathcal{P} , $P_i, i \in \{1, \dots, N\}$, N being the total number of points. We refer to their coordinates relative to an arbitrary origin in space by $x_i, i \in \{1, \dots, N\}$.

However, the labelling i and the absolute position x_i are difficult to measure since they require to label sites in real biopolymer networks and to fix an arbitrary origin. A better choice when we start from a clear reference configuration (for instance, a zero stress state) is to track displacements relative to the reference. Henceforth, it is well suited to split $x_i = x_i^0 + u_i$ in two parts : x_i^0 , the reference position, and u_i , the *displacement*, cf. ².

1.1.2 Regular lattices

The networks we will study are derived from regular lattices, this subsection present a way to describe them. We generate a regular lattice as follows : we define a unitary cell by a set of vertices ranging from 1 to $q \in \mathbb{N}^*$, and a set of edges that can connect these vertices between each other or to their periodic copies in neighbouring cells. We then replicate this unit cell all over the network. We can refer to a site by the d integer coordinates of the cell and by its number in the unit cell.³

1.1.3 Boundary conditions, Strain

A thought experiment to study the mechanics of a material is to cut a square piece of it and apply to it a small *affine deformation*. Such a deformation keeps parallel lines parallel : they can be a simple shear, an isotropic compression, an uniaxial compression or any kind of affine transformation ...

Experimentalists are able to realise these experiments in some cases. Indeed they can put the network inside of a rheometer and exert a shear on its edges, or apply a pressure from outside. We would like to be able to exert such deformations of the network from its edges. We do this by using appropriate *Lees-Edwards boundary conditions*⁴. These boundary conditions allow us to approximate an infinite system at a reasonable computational cost, and at the same time to apply affine strain to it.

Let's make explicit the scheme in 2 dimensions of space. Let's consider a network made of N cells in the direction of a Bravais⁵ vector \vec{u} , and M cells in the direction of a Bravais vector \vec{v} it totalises $N \times M$ cells. Along \vec{u} 's direction, an N 'th elementary cell a site would be connected to an $N + 1$ 'th one in an infinite system. What we do instead is to connect it to the first one in direction of \vec{u} . This can be easily done in our framework, since it comes to replace the edge $(N, N + 1)$ by $(N, 1)$ in \mathcal{E} . We emphasise here that these boundary crossing links are to be understood in a topological sense : they provide the network with the topology of a torus, but don't impact its geometry in space, in particular the corresponding terms in the energy are computed through the minimal image prescription with respect to the

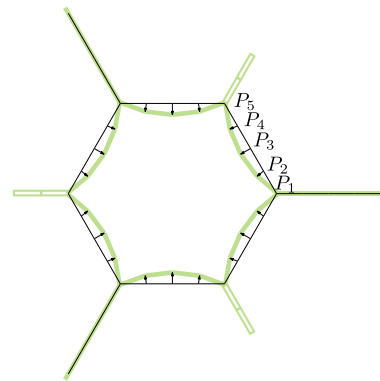


Figure 1.1: We labeled a few sites P_i and represented displacements from an hexagonal configuration by arrows.

² L. Landau, E. Lifshitz, A. Kosevich, J. Sykes, L. Pitaevskii, and W. Reid. *Theory of Elasticity*. Course of theoretical physics. Elsevier Science, 1986

³ GIVE EXAMPLES !!

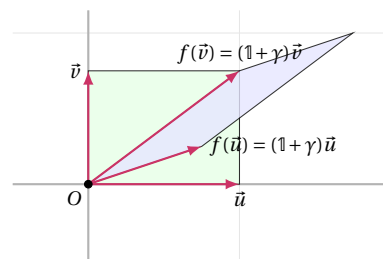


Figure 1.2: Rectangular cut all \vec{u} and \vec{v} into a material. Under affine deformation, the green rectangle deforms into the blue one, if the lengths of \vec{u} and \vec{v} become infinitesimal, γ is called the strain at the point O . If γ doesn't depend on the reference point all over the material, the material is said to affinely deform.

⁴ A. W. Lees and S. F. Edwards. The computer study of transport processes under extreme conditions. *Journal of Physics C: Solid State Physics*, Aug. 1972

⁵ N. W. Ashcroft and N. D. Mermin. *Solid state physics*. Brooks/Cole Thomson Learning, South Melbourne, repr edition, 2012. OCLC: 935097630

boundaries.

As you can see on figure 1.2, we can define a strain γ which is responsible for the affine response of Bravais vectors according to :

$$\begin{cases} \vec{u} \mapsto (1 + \gamma)u \\ \vec{v} \mapsto (1 + \gamma)v \end{cases} \quad (1.1)$$

Which allows us to decompose the displacement of a given site i into an affine part and a non affine part :

$$\begin{cases} u_i = u_i^{aff} + u_i^{Naff} \\ u_i^{aff} = \gamma x_i^0 \end{cases} \quad (1.2)$$

The Lees-Edwards periodic boundary condition that we use comes to generate an $(M + 1) \times (N + 1)$ network, and to impose boundary condition :

$$\begin{cases} u_{1,j}^{Naff} = u_{N+1,j}^{Naff} \\ u_{i,1}^{Naff} = u_{i,M+1}^{Naff} \end{cases}$$

This simplicity to apply periodic boundary conditions legitimates in its own the splitting in affine and non affine displacement : the non affine displacement is a property of sites, whereas the affine displacement is a property of edges. Namely, when it will come to compute forces on sites, we will always deduce the end-to-end vector between sites from the edges' affine displacements and the non affine displacements of sites, never referring to absolute position in space, thus treating edges that come across the system as the bulk ones.

However, this way of enforcing boundary conditions challenges intuition. It doesn't fix all positions on the boundaries of the system, instead it divides the number of boundary degrees of freedom by two with respect to the free boundary case. Instead of 4 tunable straight walls we only have two Fig. 1.4 that can lie on a curve. This kind of features can appear when compressive a triangular lattice for instance. In that case, creases can appear in the networks as described in reference⁶. This had been observed by Pierre Ronceray when I arrived in 2016 and he highlighted to this amusing fact at that time.

⁶ S. Ganguly, D. Das, J. Horbach, P. Sollich, S. Karmakar, and S. Sengupta. Plastic deformation of a permanently bonded network: Stress relaxation by pleats. *The Journal of Chemical Physics*, (18), Nov. 2018

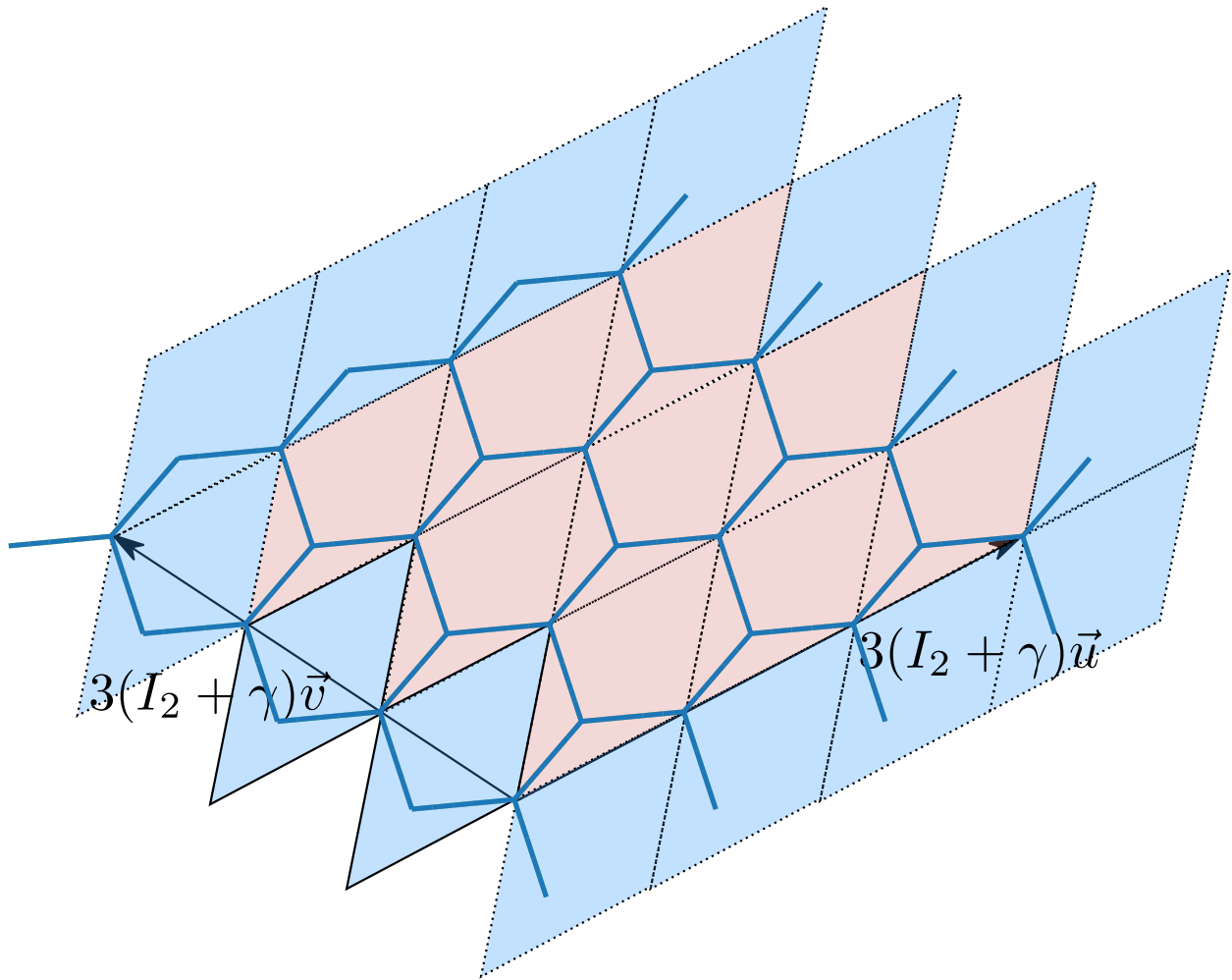


Figure 1.3: Lees-Edwards periodic boundary conditions used to shear a 4×4 honeycomb lattice of 20%. The edges are represented in blue, the strained Bravais vectors in black, and the unit cells with dotted black boundaries. The 3×3 pink cells are in the bulk of the network, but the outer layer of blue cells are connected to each other through the boundaries, thus they allow strains to be applied.

We can thus apply a strain to the system by changing the affine displacements on edges, which amounts to change \vec{u} and \vec{v} to $(1 + \gamma)\vec{u}$ and $(1 + \gamma)\vec{v}$, that is to deform the reference box into a parallelogram. Sites have then the freedom to move around this configuration by means of non affine displacements.

1.2 Mechanics of the network : system's potential energy

In the previous section we described the kinematics of the network, we will now discuss its interactions. In the introduction, we have focused our interest in bundled actin networks, which are polymer networks crosslinked over a distance small in front of their persistence length, i.e. semiflexible networks, in presence of residual stresses due to frustrated bundles. Henceforth, the relevant forces will be entropic stretching, bending rigidity⁷ and our new ingredient, residual stress which we present later a model of.

1.2.1 Bending interaction

Physical origin. Biofilaments result from the assembly of a repeated pattern of proteins. The complex links binding these proteins together provides a finite stiffness to filaments. For example actin filaments result from an helicoidal twist of actin monomers, and have a persistence length of around $10\ \mu\text{m}$ at room temperature⁸. Furthermore, cross-linking proteins such as α -actinin are able to gather filaments into bundles, providing bundle a cooperative bending stiffness which has been measured in ref⁹. Some detailed models were proposed in ref.¹⁰ concerning the coupling between cross-linkers shear and bundle extension, bundle twist, and bundle bending. However, we will merely model a bundle by a filament characterized by its bending and stretching stiffnesses as we think of α -actinin as cross-linker, which we consider as unshearable : henceforth, there is no bundle's state-dependant bending stiffness to consider.

A model that is often used is the *worm-like chain model* in which we model a polymer by a continuous curve parameterized by its arc length s ranging from $-\frac{\ell_0}{2}$ to $\frac{\ell_0}{2}$, ℓ_0 being the rest length of the polymer. This model was originally introduced in¹¹. We assume that we are in $2D$, which allows to consider the field $\phi(s)$, which represents the angle between a reference axis and the tangent vector to the polymer at arc length s . The bending energy per unit length has to be a function of the spatial variations of $\phi(s)$, and to be minimal for a straight polymer. We introduce the bending constant per unit length κ_c so that

$$e_b(s) = \frac{\kappa_c}{2} \left(\frac{\partial\phi}{\partial s} \right)^2 (s)$$

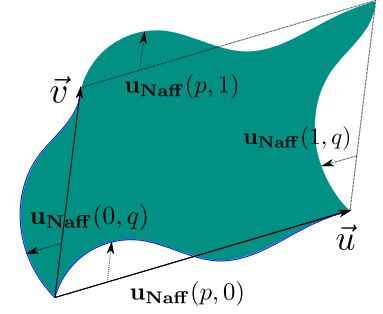


Figure 1.4: Lees-Edwards periodic boundary conditions might challenge intuition since they allow soft walls with identical non affine displacement from wall to wall.

⁷ C. P. Broedersz and F. C. MacKintosh. Modeling semiflexible polymer networks. *Reviews of Modern Physics*, July 2014. arXiv: 1404.4332

⁸ F. Gittes. Flexural rigidity of microtubules and actin filaments measured from thermal fluctuations in shape. *The Journal of Cell Biology*, Feb. 1993

⁹ F. R uckerl, M. Lenz, T. Betz, J. Manzi, J.-L. Martiel, M. Safouane, R. Paterski-Boujema, L. Blanchoin, and C. Sykes. Adaptive Response of Actin Bundles under Mechanical Stress

¹⁰ C. Heussinger, F. Sch uller, and E. Frey. Statics and dynamics of the wormlike bundle model. *PHYSICAL REVIEW E*, 2010; and M. Claessens, M. Bathe, E. Frey, and A. Bausch. Actin-binding proteins sensitively mediate f-actin bundle stiffness. *Nature materials*, 10 2006

¹¹ O. Kratky and G. Porod. R ontgenuntersuchung gel oster Fadenmolek ule. *Recueil des Travaux Chimiques des Pays-Bas*, Sept. 2010

which leads to the potential energy functional :

$$\mathcal{U}[\phi] = \int_{-\frac{\ell_0}{2}}^{\frac{\ell_0}{2}} \frac{\kappa_c}{2} \left(\frac{\partial \phi}{\partial s} \right)^2 (s) ds.$$

This form is able to take account of bending modes no matter their wavelength since it has an infinite number of degrees of freedom. However, it would be impossible to deal numerically with them. Henceforth we need to find an discrete approximation of filaments, reasonable enough to capture the low wave-length properties of the continuous model, tractable enough to be used in large networks.

Our numerical model.

For this we subdivide a filament of rest length ℓ_0 into N strands of rest length $\frac{\ell_0}{N}$. We will refer to a structure of two subsequent edges in this subdivided filament as hinges denote them by $h = (e_i, e_j) \in \mathcal{H}$ since they are a set of edges. For this reason, the set of hinges can be generated on a non ambiguous way from the mere data of \mathcal{E} and \mathcal{P} . We draw examples of hinges in 1.5.

On an energetic viewpoint we introduce a discrete bending constant $\frac{\kappa}{\ell_0}$ so that the bending energy of the filament reads :

$$E_b(\{u_i\}) = -\frac{N\kappa}{\ell_0} \sum_{(e_1, e_2) \in \mathcal{H}} \left(\frac{\vec{u}_{e_1} \cdot \vec{u}_{e_2}}{u_{e_1} u_{e_2}} - 1 \right)$$

With a sum on the $N - 1$ hinges formed by the N edges. We will establish and discuss in section 1.3.1 a correspondance between the two models. We chose this scaling for the bending stiffness so that the model converges towards the worm-like chain model as $N \rightarrow \infty$, which provides a link to the measurable continuous κ_c .

This energy is minimal when \vec{u}_{e_1} is aligned with \vec{u}_{e_2} in all hinges, it is maximal when they point in opposite directions. A typical intermediate situation is displayed 1.6. The interaction becomes increasingly soft as we bend hinges, which can be understood easily on the case of a two edges filaments for which the energetical cost $-\cos(\phi_1 - \phi_2)$ is bounded, contrarily to $(\phi_1 - \phi_2)^2$. However when $N \rightarrow \infty$, this difference with the quadratic energy $\frac{(\phi_{(i+1)} - \phi_i)^2}{2}$ disappears since angle variations between neighbours get smoothed out. Taking this energy instead of the quadratic represents a gain in computational time given it avoids costly arccos evaluations to compute the angles ϕ_i by inverting the scalar product between unit edge's vectors.

1.2.2 Stretching interaction

Physical origin. At biological micron-size scales, filaments are subject to thermal fluctuations. Indeed they evolve in an aqueous medium which subjects them to collisions with water molecules, inducing energy exchanges between a thermal bath and the polymer. Thermal fluctuations play a role of major importance as discussed in the introduction.

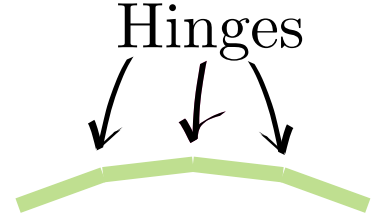


Figure 1.5: Examples of three hinges $h_1 = (e_1, e_2)$, $h_2 = (e_2, e_3)$ and $h_3 = (e_3, e_4)$ on a rod subdivided into four segments.

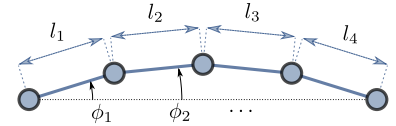


Figure 1.6: The geometrical interpretation of the bending energy on a hinge is made clearer if we introduce angles of edges with respect to (Ox) . For instance here the energy of the first hinge can be written $2 \frac{N\kappa}{\ell_0} \sin^2 \left(\frac{\phi_1 - \phi_2}{2} \right)$.

If an operator controls the end-to-end length of a polymer, he notices that they are exponentially more coiled configurations with a small end-to-end vector than they are extended ones with a large end-to-end vector. For this reason he feels an entropic restoring force against extension. In biological networks, no operator can control the filaments' extension, but they belong to a mesh, at an average distance ξ of each other. Depending on how ξ relates to the persistence length of the polymers, the latter will behave as springs and their bending-to-stretching ratio $\frac{\kappa}{\mu}$ will evolve as $\frac{\xi^4}{l_p^2}$. Typically $\frac{1}{1000}$ is observed in semiflexible biologic meshes : filaments are very stiff in extension, and softer in bending, we will account of this in simulations by staying close to the inextensible limit, which will be discussed in a next section.

Our Model. In this thesis, we will not model explicitly the fluctuating filaments, instead we will introduce the stretching energy that an effective edge would have to mimick the average behaviour. This approximation is only valid in a mesh with cell size small compared to the persistence length, which is our framework.

In our discrete approximation, we model filaments strands as springs with rest lengths $\frac{\ell_0}{N}$ and stiffness per strand $\frac{N\mu}{\ell_0}$. The resulting stretching stiffness reads :

$$E_s = \frac{N\mu}{2\ell_0} \sum_{e \in \mathcal{E}} \left(l_e - \frac{\ell_0}{N} \right)^2.$$

This is merely the energy of an hookean spring, it is minimal when all edges are of length ℓ_0 , i.e. when the full filament is of length ℓ_0 . This is a Taylor expansion of the average energy-extension relation we obtain in a worm-like chain model ¹² in the canonical ensemble. This form remains valid for small extensions, however we will typically take very stiff springs in simulations, so there won't be excursions to extreme extensions.

1.2.3 Residual stresses

Physical origin. Cross-linked actin networks are made of a self-assembly of interacting filaments. These filaments tend to stay straight, they are interacting together, they are long compared to the characteristic lengths of these interactions, and the mesh size can be comparable with it. As a result, residual stresses remain in configurations that are macroscopically at rest. An example of it is provided by actin networks cross-linked with high rates of α -actinin ¹³. The filaments are gathered into bundles aligned parallel to one another over lengths up to the mesh size. Over larger scales however, the bundles split making forks as you can see on the cartoon displayed Fig. 1.9.

We will take this kind of residual stresses into account by introducing an angular interaction in our system on each site with coordination number of 3.

¹² A. V. Dobrynin, J.-M. Y. Carrillo, and M. Rubinstein. Chains Are More Flexible Under Tension. *Macromolecules*, Nov. 2010

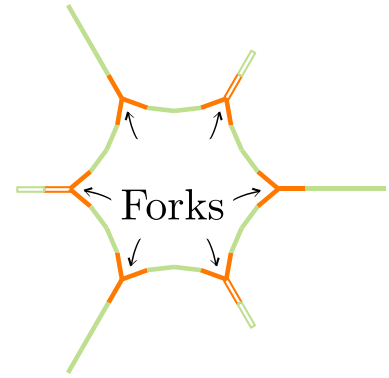


Figure 1.7: Example of closing forks in orange, they are the 3 coordinated nodes.

¹³ T. T. Falzone, M. Lenz, D. R. Kovar, and M. L. Gardel. Assembly kinetics determine the architecture of α -actinin crosslinked F-actin networks. *Nature Communications*, Jan. 2012

Our model. We will refer to a structure of three neighbouring filaments incident on a site as forks, we note them $f \in \mathcal{F}$. The set of forks can be generated on a non ambiguous way from the mere data of \mathcal{E} and \mathcal{P} . We draw examples of forks in 1.7. Forks are our model for frustrated bundles.

We will stick to the case of a 2D lattice, with a coordination number of 3. This degree of coordination enables us to think of forks distributed all over the network that exert angular stresses on the filaments. We take the following residual stress energy :

$$E_r = 2g \sum_{i=1}^3 \sin^2 \left(\frac{\delta\theta - \delta\theta_0}{2} \right),$$

which has two adjustable parameters : its intensity g , and the frustration angle $\delta\theta_0$. The angular degrees of freedom $\delta\theta$ are depicted in 1.8, they correspond to the difference between the opening of the thirds of forks in the present configuration and in the honeycomb rest configuration it would have without residual stress.

This energy is minimal when the two angles adjacent to the parent filament equate $\frac{2\pi}{3} + \delta\theta_0$ and the angle in front of it equates $2 \left(\frac{\pi}{3} - \delta\theta_0 \right)$.

We think of this energy as a modification of the honeycomb geometry. In the latter, all filaments can stay straight and keep a unit length ; by introducing frustrated angles we induce residual stresses in the network. This cannot be seen as a perturbation since forces doesn't stay infinitesimal : we take typically very stiff angular rigidities g . This specific point is going to be discussed in section 1.3.2.

We stress out the fact that this form is more general than a simple model of closing forks since it gathers all possible $\delta\theta_0$ ranging between $\frac{\pi}{3}$ (fully closed forks) and $-\frac{2\pi}{3}$ (fully open forks).

Choice of directions.

This interaction over a single fork is anisotropic. For this reason we must distribute forks' directions throughout the network to maximise symmetry of the elastic properties. For this we tried two solutions :

- We distributed the directions at random at every 3-coordinated node of a honeycomb lattice. generate the full network and we coin a 3-states uniform random variable over each fork to decide its direction.
- We built a repeated pattern of unit cells. These cells had directions distributed by hand according to a specific rule. This rule was to have as many forks pointing in each direction in the unit cell. We show in appendix 1.4 that we can reduce all choices possible to the four inequivalent families invariant up to the axial symmetries and rotations that leave the honeycomb cell invariant. These geometries are labelled (α) , (β) , (γ) and (δ) , we represent them into 1.10.

The first choice is better approximating the mechanics of a real prestressed

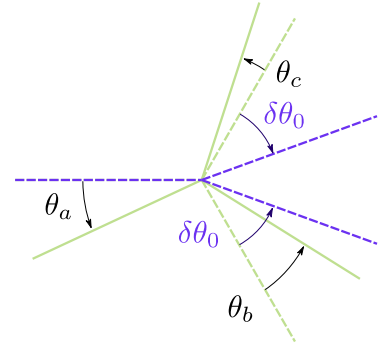


Figure 1.8: We represent in dashed green the honeycomb configuration, in dashed purple the preferred orientation of a fork turned to the right, and in plain green a general configuration of the fork. We measure fork angles with respect to what they are in the honeycomb lattice. We define θ_a , θ_b and θ_c the angles formed by the edges with respect to their value in the honeycomb lattice. We then measure $\delta\theta_{ij}$ the opening angle of the third of fork (ij) (with $(i, j) \in \{a, b, c\}^2$). Here the purple configuration has $\delta\theta_{ac} = \delta\theta_{ab} = \delta\theta_0$.

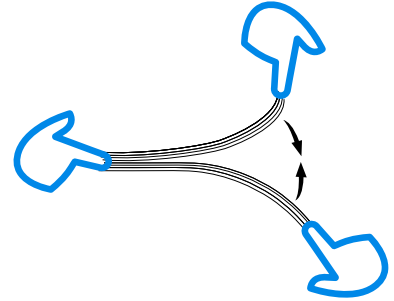


Figure 1.9: Cartoon of a fork oriented to the right. It represents its bundle microscopic structure. The hands represent the anchoring points that are imposed by the rest of the network during its self assembly process. The zipping of the bundle continues up to a point where there is a strong energetic barrier for a cross-linker to bind the two strands. At this point, strong residual stresses are exerted on the fork as represented by the arrows. This is what our models describes : a fork has a preferred angle, which results from the competition between anchoring and zipping, we will consider very strong bindings.

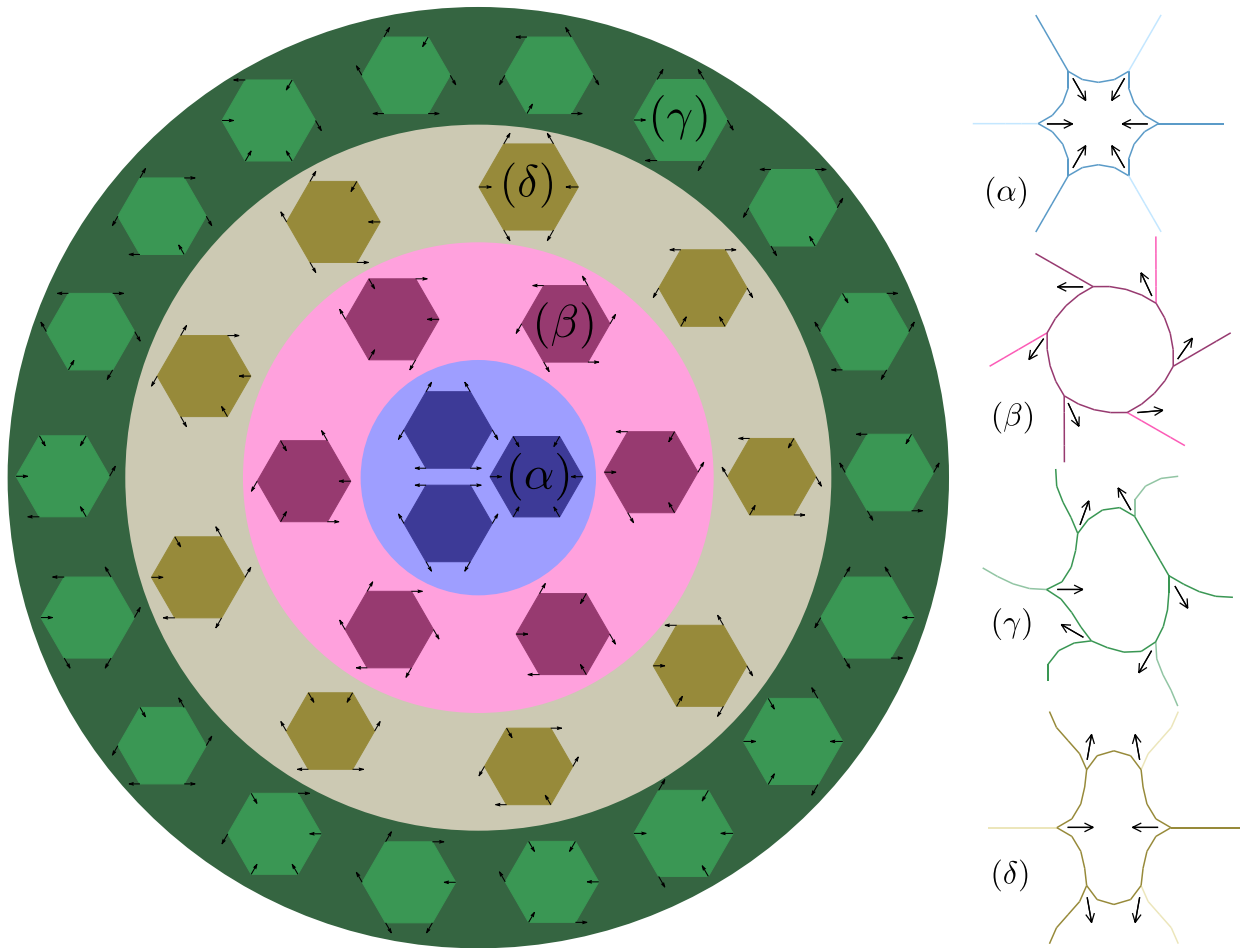


Figure 1.10: The 4 classes of inequivalent geometries are represented in four different colours in four different backgrounds. The arrows represent the direction in which forks close. We chose one representant in each category, the greek label of the class is written on top of the representant. The zero boundary stress geometry is plotted on the right for each representant for $g = 1000$ and $\delta\theta_0 = \frac{\pi}{6}$, dimmer colors suggest the periodic boundary conditions.

network with coordination of 3, whereas the second choice enables to perform analytic calculations and are instructive in their simpler behaviour.

1.2.4 Dimensionless form for energy

At this stage, we have several adjustable parameters. In order to get rid of a part of this complexity, we will put them in dimensionless form.

Let's first list out the dimensions of the different physical parameters :

- The potential energy \mathcal{U} has units of an energy.
- The stretching constant μ has units of an energy over a length.
- The length of edge e ℓ_e has units of a length.
- The rest length of a filament ℓ_0 has units of a length.
- The bending constant κ has units of an energy times a length.
- The intensity of residual stress g has units of an energy.
- Angles are dimensionless.
- The number of subdivisions of filaments is dimensionless.

We choose ℓ_0 as unit of length, and $\frac{\kappa}{\ell_0}$ as unit of energy. The following dimensionless tilded variables derive from this choice :

$$\begin{aligned} \ell &\mapsto \tilde{\ell} = \frac{\ell}{\ell_0} \\ \mathcal{U} &\mapsto \tilde{\mathcal{U}} = \frac{\ell_0}{\kappa} \mathcal{U} \\ \mu &\mapsto \tilde{\mu} = \frac{\mu \ell_0^2}{\kappa} \\ g &\mapsto \tilde{g} = \frac{g}{\kappa}. \end{aligned}$$

This choice only leaves us with 4 adjustable parameters : the number of subdivisions of filaments N , the reduced residual stress intensity \tilde{g} , the reduced stretching constant $\tilde{\mu}$ and the opening of forks at rest $\delta\theta_0$. As a consequence, the dimensionless reduced potential energy reads

$$\begin{aligned} \tilde{\mathcal{U}} &= \sum_{e \in \mathcal{E}} \frac{\tilde{\mu} N}{2} (\tilde{\ell}_e - 1/N)^2 \\ &+ 2N \sum_{(e_1, e_2) \in \mathcal{H}} \sin^2 \left(\frac{\phi_{e_1} - \phi_{e_2}}{2} \right) \\ &+ 2\tilde{g} \sum_{f \in \mathcal{F}} \sum_{i_f=1}^3 \sin^2 \left(\frac{\delta\theta_{i_f} - \delta\theta_{i_f,0}}{2} \right). \end{aligned}$$

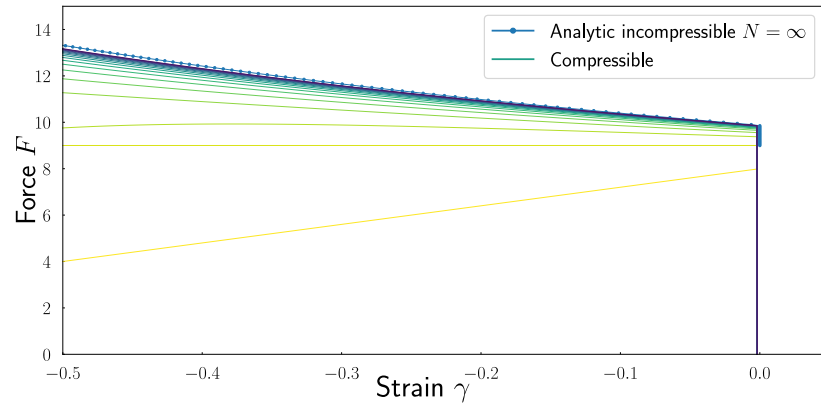
N plays a special role in that it is not a physical observable : it is an artifact of our model, which aims at reducing the number of degrees of freedom

while keeping important physical features observables. In section 1.3.1, we make sure to tune it to the least value that allows physics to be observed. From now on we will get rid of the tildes forever in this thesis, always talking about the reduced dimensionless quantities.

1.3 Sending parameters to infinity

In the previous section we put the model in dimensionless form to be sure that no parameters were physically redundant. However we still need to discuss the number of subedges in each filaments, as we cannot afford numerically to increase too much the number of degrees of freedom in the system. In addition, our system of interest behave as inextensible, which addresses the question of the inextensible limit in our model. In this section we make simulations in simple systems to justify the parameters that we will use later on in the thesis.

1.3.1 Estimating continuous limit from segmented filaments



The model with two subedges is unable to take into account bendings of the modes of order larger than one for one polymer^{1.11}, this was problematic since a filament with opposite angular forcings on its ends should bend on its mode n°2.

For this reason, we study continuous the limit where the number of edges in a filament $N \rightarrow \infty$. For this we study the 1D chain of springs under axial compression for $N \rightarrow \infty$, as displayed in 1.12. In the figure 1.13. the strain in the filament is defined as $\gamma = \frac{\ell - \ell_0}{\ell_0}$.

It is worth noting that we find the usual buckling phenomenology¹⁴: for positive strains the filament remains straight and its response is stretching dominated, with a stiffness (here the slope in the diagram $-\frac{dF}{d\gamma}$) of order μ . After some buckling threshold γ_0 , which is almost zero here given the

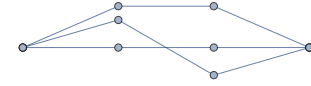


Figure 1.11: Here we represent the 2 bending modes of filament subdivided in 4 parts (the 2 remaining one are stretching modes). A system with N degrees of freedom has N normal modes. However two angular forcings in opposite directions at the ends of the system can enhance filament's mode 2 bending and will require at the very least 3 subedges to be possible.

Figure 1.13: Convergence of the force-strain curve to a continuous limit (with dots) as N grows from 2 (yellow) to 20 (purple) for $\mu = 10^5$.

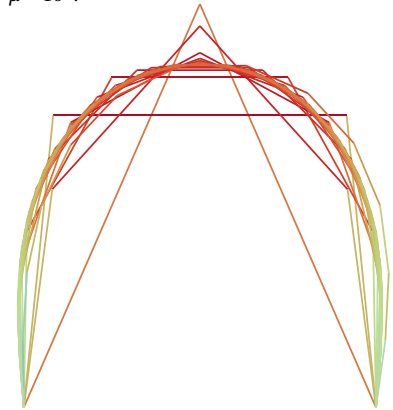


Figure 1.12: Here we represent the spatial configuration of the filaments for a strain $\gamma = 60\%$. N ranges from 2 to 20. In red appear the filaments under compression, in green those that are unextended. This gives us a feeling of the continuous limit, and asks the question of extension of coupling between stretching and bending.

¹⁴ C. P. Brangwynne, F. C. MacKintosh, S. Kumar, N. A. Geisse, J. Talbot, L. Mahadevan, K. K. Parker, D. E. Ingber, and D. A. Weitz. Microtubules can bear enhanced compressive loads in living cells because of lateral reinforcement. *The Journal of Cell Biology*, 2006

stretching to bending ratio, the filament buckles on its mode 1, it has a rigidity of order κ .

On the other hand, we can obtain force-strain curves analytically in the limit where $\mu \rightarrow \infty$. For this we cancel out the functional derivative of 1.2.1 with respect to the tangent vector angle $\phi(s)$ under a force F . This leads to the resolution of :

$$\begin{cases} \frac{d^2\phi}{ds^2} - F \sin(\phi) = 0 \\ \frac{d\phi}{ds} \left(-\frac{1}{2}\right) = 0 \\ \frac{d\phi}{ds} \left(\frac{1}{2}\right) = 0 \end{cases}$$

The boundary condition on θ is a null torque on edge filaments as indicated on fig. 1.14. We note ϕ_F^* the solution function for a given value of F , we solve it numerically by using a shooting method that starts from a non zero Ansatz $\phi(s) = -\epsilon \cos(2\pi s)$, $\epsilon > 0$ so as to break the symmetry between top and bottom. We can then obtain the length as a function of F :

$$\ell(F) = \int_{-\frac{1}{2}}^{\frac{1}{2}} \cos(\phi_F^*(s)) ds$$

and use it to compute the strain $\gamma(F) = \ell(F) - 1$ and plot the reference curve in fig. 1.13.

In order to get a quantitative criterion to evaluate how we reached the continuum limit, we plot the relative differences between the worm-like chain model and our finite differences one in figure 1.15.

To conclude, we can select a threshold on how accurately we want to approximate the continuous limit by simply reading it on the above graph of relative differences, and that provides us one value for N (the value of μ being fixed). The more accurate we want to be, the larger number of degrees of freedom we must involve in the simulation. Typically, if we want to reach the continuous limit at 10%, we must use $N = 10$. A less drastic choice to keep simulations fast is to wonder which modes of deformation are physically meaningful, and which we can get rid of. Indeed, we will see later that forks never bend on deformation modes of order more than two : we choose $N = 4$ so as to be able to take account of them, we read on the above graph that it lead to an accuracy to the continuum of at worst 25% for large deformations.

1.3.2 Tuning prestress parameters : the strong clamp limit

In order to study the effect of prestress, we have to tune two parameters : the forks stiffness g and their rest angle defect $\delta\theta_0$. We want to generate strong angular anchoring that couldn't be uncoiled by bending modes. Indeed, the process leading to residual stress is the maximal zipping of two partial bundles up to the point where it becomes energetically impossible for cross-linkers to fight against the tension stored into the bundle because of the steric constraints in the network. However the binding energy of cross-linkers is around $2k_B T$ for a bond of size of 20 nm as reported on ref. ¹⁵.

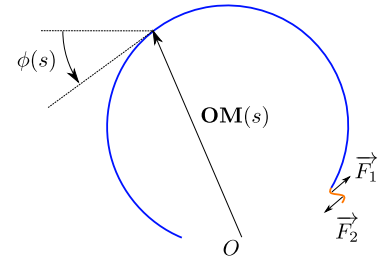


Figure 1.14: Geometry of a continuous filament, the point $M(s)$ at arc length s on the filament is labeled by the vector $\mathbf{OM}(s)$ with respect the origin. We see that spatial variations of ϕ induce a torque. As an example the orange part here is subject to a torque because of two opposite variations in angle that induce forces \vec{F}_1 and \vec{F}_2 .

¹⁵ H. Miyata, R. Yasuda, and K. K. Jr. Strength and lifetime of the bond between actin and skeletal muscle a-actinin studied with an optical trapping technique. 1996

Discretisation effect on 1D filament's force-strain curve

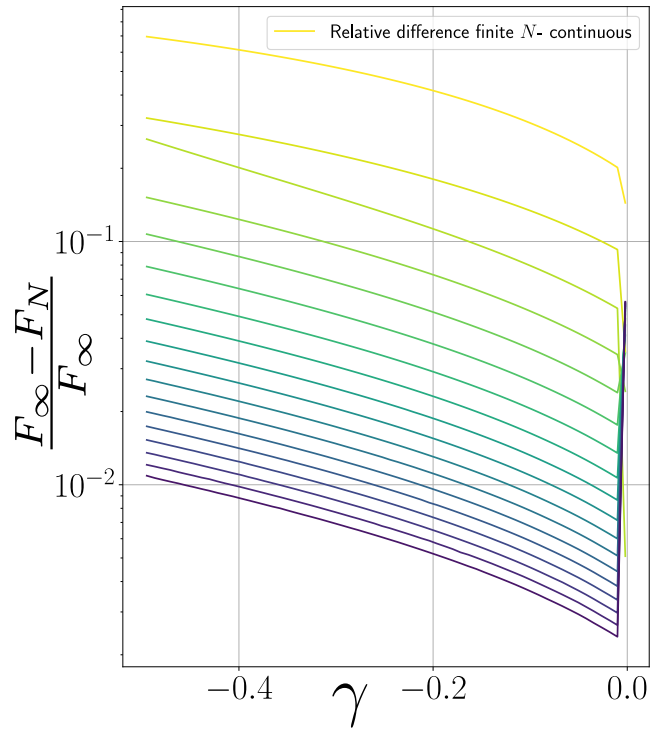


Figure 1.15: Relative difference between WLC and finite N model (yellow for $N = 2$, purple for $N = 18$), stretching stiffness $\mu = 10^5$. One notices that the more compressed are the filaments, the more finite μ effects show up. Indeed, some stretch remains in such cases, as we experienced on fig. 1.12

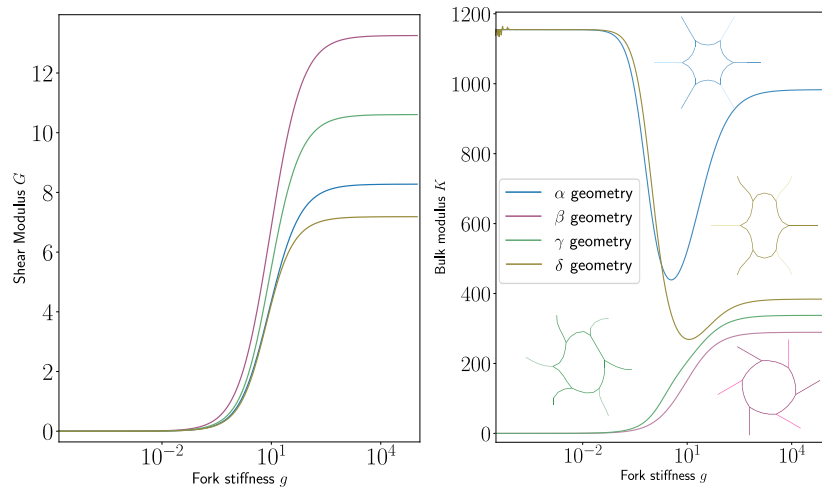


Figure 1.16: Bulk modulus and shear modulus around the zero boundary stress configurations of the four geometries (α), (β), (γ) and (δ) as a function of the fork stiffness g , $\delta\theta_0 = \frac{2\pi}{6}$, $N = 4$. A corresponding color code displays the zero boundary stress geometries for $g = 1000$.

The bending energy required over the same length is much smaller, thus our approximation.

For this reason we study in this section the $g \rightarrow \infty$ limit on the four unit geometries (α), (β), (γ) and (δ). We display measurements of shear modulus and bulk modulus versus g in fig. 1.16. For shear moduli, we observe two regimes : for low g 's, the response under compression is essentially due to the deformation of forks, at a cost $g \ll 1$ for (β), (γ) and (δ). For bulk moduli, (α) and (δ) behave differently at low values of g . Indeed their response is governed by stretching (bulk modulus of order $\mu = 1000$) because forks are too weak to bend filaments, henceforth the networks respond affinely to an infinitesimal isotropic strain, which stretches the filaments.

In both cases the second regime starts for g of order 1000. We see a saturation of network's response because forks become so stiff that they don't participate anymore in the network elastic response. We choose everywhere after in this thesis to work with $g = 1000$.¹⁶

1.3.3 Tuning stretching constant : the inextensible filament limit

Up to now, we were in the approximation $\mu \ll 1$ where stretching dominates largely over bending. We want to control this approximation because of numerical error issues in simulations ranging from slow convergence to inaccuracy in results. Indeed, the energy is a sum of many terms with different orders of magnitude, which is a typical example of where numerical errors issues come out in computer science. Let us tell a few words about those : floating point numbers use a certain number n of bytes to be stored in memory. Those n numbers are shared between p numbers for the *significand* and q numbers for the exponent¹⁷. To fix ideas, we take $n = 64$, $p = 53$ and $q = 11$ which is the official norm for the double precision numbers that we use in C++.

The significand can thus range between the binary number $-0.1111 \dots 11$ with 52 "ones" and the binary number $0.1111 \dots 10$, with 51 "ones", whereas the exponent can range between $-2^{10} = -1024$ and $2^{10} - 1 = 1023$. Which in basis of 10 gives up to 14 digits, among which seven are relevant.

This way of encoding for number enables to perform a difference between two numbers of different orders of magnitude at the price of the loss of the lowest decimals in basis of two. The more the exponents are away from each other, the more we loose digits. Another phenomenon occurs when taking the differences of very close numbers is truncation error, which rounds off the result to the closest binary number ... 0 in extrem cases !

Let's come back to our filament : untill now we had $\mu = 10^5$, it is worth wondering about cancelation error in energies since bending energy and stretching energy differ by orders of magnitude for unit displacements. This time, we stay at $N = 20$ and we study the effect of μ ranging from 100 to $100 \cdot 2^{19}$ to show the precision loss as μ increases in figure 1.19. We also see

¹⁶ As we will see when sending stretching constant to infinity in section 1.3.3, convergence time increases as g increases, we were also afraid of numeric error issues, but they only show up when there are orders of magnitude of difference between μ and g (typically, when $g = 10^{-4}$ and $\mu = 1000$). We didn't address them quantitatively however.

¹⁷ B. A. Stickler and E. Schachinger. *Basic concepts in computational physics*. Springer, Cham, second edition edition, 2016. OCLC: 951090652



Figure 1.17: We display the geometry of an Euler elastic rod made of $N = 20$ edges. In red edges are compressed, in green they are at rest. For strong compression rates, we end up with a coupling between bending and stretching, even for large μ .

the shift in buckling threshold and the convergence to an unstretchable limit.

Like before we plot the relative differences with the incompressible limit in Fig .1.3.3. The incompressible limit is given by the shooting method for the worm-like chain model described when studying the continuum limit.

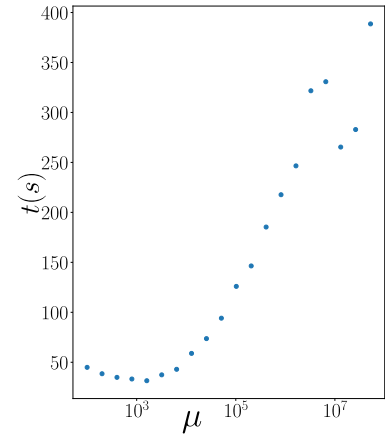


Figure 1.18: Computational time to perform a compression of the system from $\gamma = 0.2$ to $\gamma = 0.6$ in 400 steps, $N = 20$. At first it goes down as some time is spent in changing edges lengths, then it increases because . This one of the reasons for our choice of $\mu = 1000$.

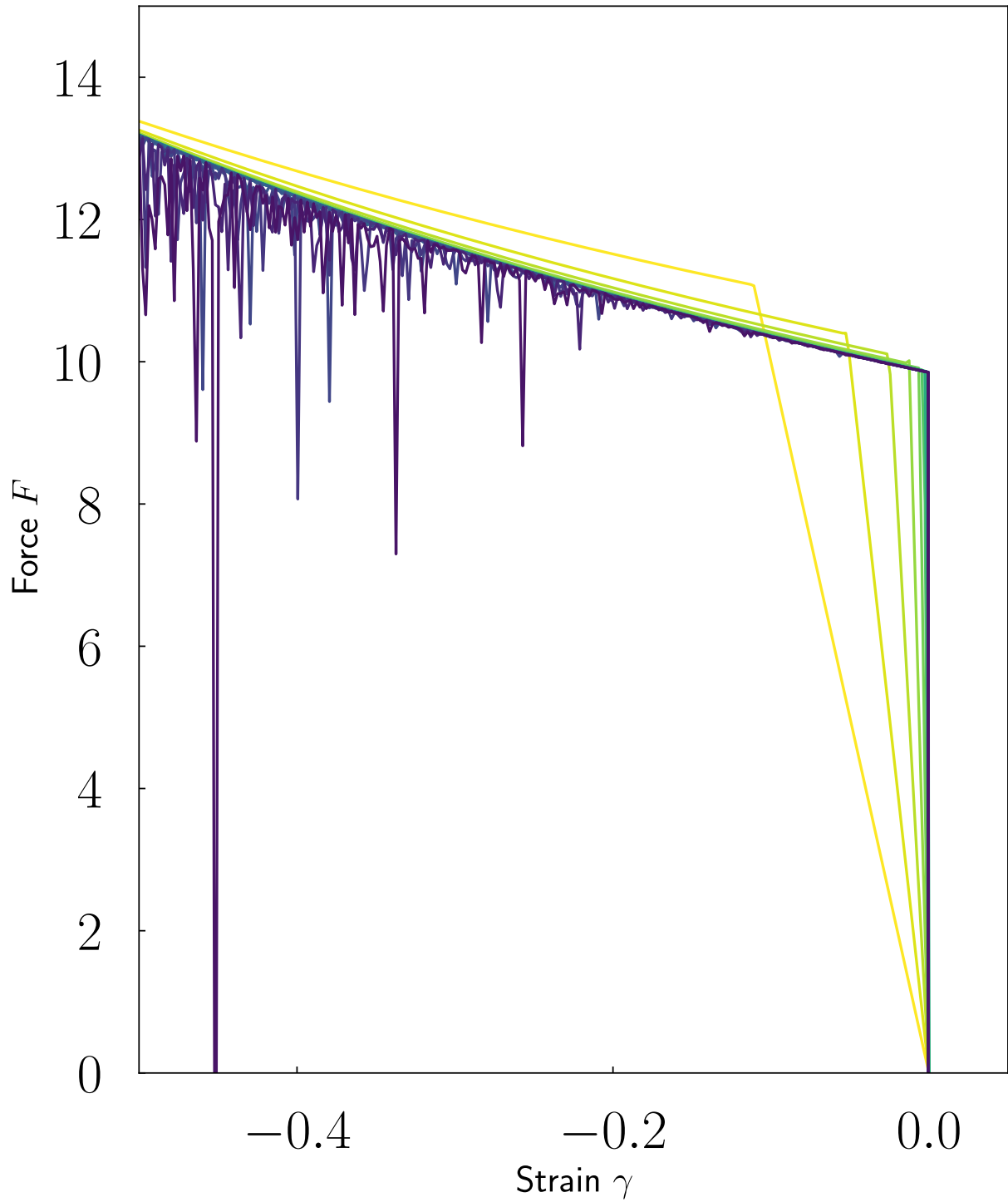


Figure 1.19: Influence of μ on the force-strain curve, $N = 20$ from yellow to purple, we go from $\mu = 100$ (yellow) to $\mu = 100.2^{19}$ (purple). The buckling threshold is affected by the stretching to bending ratio μ . Furthermore, cancellation error appear as μ grows too much.

To conclude, we have an evidence that finite stretching effects occur, and that they get increasingly important as we compress strongly the filaments 1.3.3. These differences are qualitatively inexistant, and quantitatively small : for $\mu = 100000$, the relative difference to the incompressible limit is below 10% for $N = 20$.

However the bigger μ gets, the more numerical error we accumulate and the longer the simulations take 1.3.3. For this reason, we chose to take $\mu = 1000$ everywhere after.

1.4 Appendix : construction of units cells geometries

This appendix explains how we classified the orientation of the forks throughout the network in the network. In a first part we explain the choice of the span of an individual cell, in a second part we explain how we represented the directions of forks in a handy way, so as to generate automatically all the classes with the group theoretic tools in Mathematica software.

The unit cell of a honeycomb lattice in the absence of residual stress cannot be the basis of a periodic repetition of directional forks, indeed it contains only one fork, and would lead to an anisotropic mechanics with an axis. For this reason, we chose an unit cell over a full hexagon, as displayed in fig. 1.21. Then we label the six possible sites inside of an hexagon from 1 to 6. To represent an unit cell, we draw arrows on top of these sites in the direction in which the fork operates. We label it by its affix $z_p = e^{i\theta_p}$. We end up with $3^6 = 729$ possibilities to distribute forks, some of them being obviously anisotropic as the average direction of their forks differs from 0. For this reason, we first reduce the amount of these geometries before classifying the remaining ones.

Reducing the amount of geometries. The first filtration of cells will occur with as we will keep only cells with one fork in each direction. To construct such a configuration, we draw one arrow out of three on top of site 1, one arrow out of the two remaining in the site 3, and the site 5 follows. We do the same thing for sites 2, 4 and 6. By doing so we reduced the possible geometries to $3^2 2^2 = 36$ possibilities.

Construction of equivalence classes. At this stage, we will analyse the symmetry group of a honeycomb network, and construct equivalence classes of cells that are images of each other under these symmetries.

The periodic lattice that we consider is invariant under all the transformations generated by iterations of :

- The axial symmetry of a cell with respect to axis of (Ox) . Its effect is to send the affix z_p of the arrow of site p to $\overline{z_p}$ after sending sites $(1, 2, 3, 4, 5, 6)$ to $(1, 6, 5, 4, 3, 2)$, in the end it sends $(z_1, z_2, z_3, z_4, z_5, z_6)$ to $(\overline{z_1}, \overline{z_6}, \overline{z_5}, \overline{z_4}, \overline{z_3}, \overline{z_2})$.
- The rotation of angle $\frac{\pi}{3}$ with center in the middle of the reference hexagon.

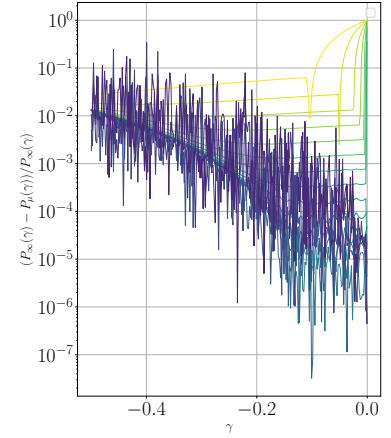


Figure 1.20: Relative difference between the force-strain curve and the inextensible one as μ goes from 100 (yellow) to 100.2^{19} (purple), for $N = 20$. We see the relative error reduce (in the post-buckling region) as μ increases.

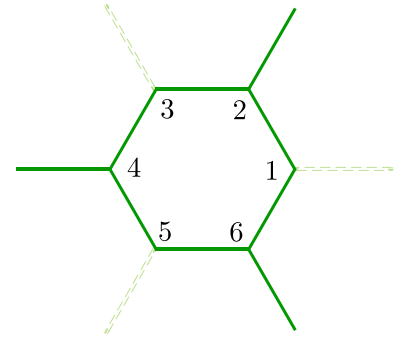


Figure 1.21: We label the 6 sites of an hexagon from 1 to 6. We coloured differently the possible reference unit cells to highlight the permutation operation that occurs when doing a translation from one to the other.

It sends $(z_1, z_2, z_3, z_4, z_5, z_6)$ to $e^{i\frac{\pi}{3}}(\overline{z_6}, \overline{z_1}, \overline{z_2}, \overline{z_3}, \overline{z_4}, \overline{z_5})$.

- The translation symmetry which is reminiscent of our choice to take a light green reference cell instead of a dark green or a purple hexagon in 1.22. The transformation that brings from light green to dark green, and from dark green to purple sends $(z_1, z_2, z_3, z_4, z_5, z_6)$ to $(z_3, z_6, z_5, z_2, z_1, z_4)$.

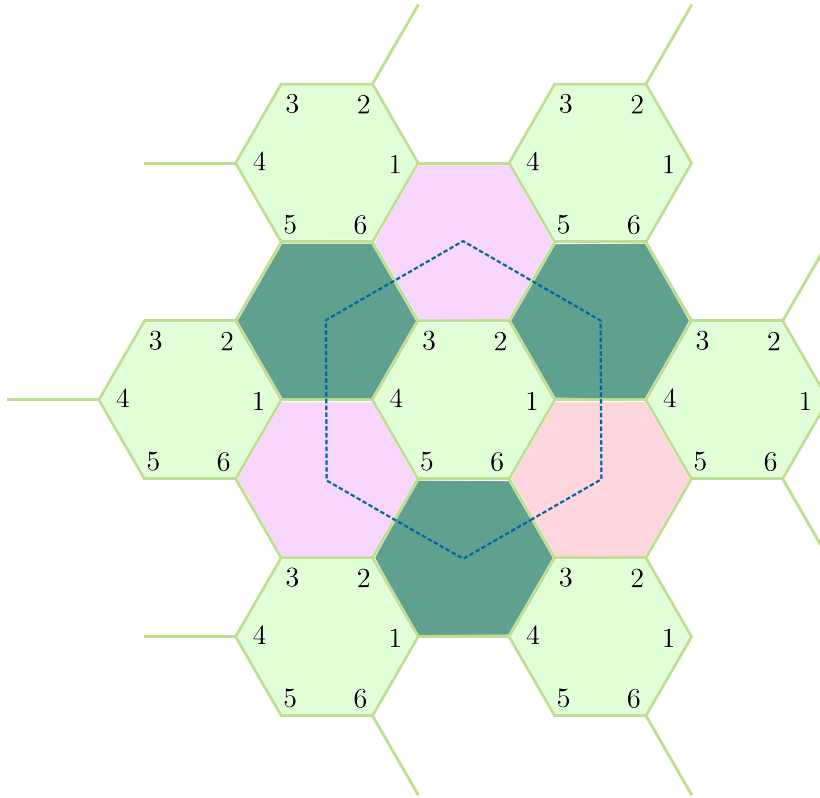


Figure 1.22: If we consider the whole crystal, there is a translation symmetry which depends of our choice of $(0,0)$ cell to be light green, dark green or purple. This gauge invariance is reminiscent of the fact that the translational group of the honeycomb lattice is not the one of our pattern of forks.

To obtain an equivalence class, we take a geometry, and we iterate symmetries operations several times on it, up to the point where we find the first configuration back¹⁸. We then start back with a not yet spanned element. We finally label the equivalence classes according to the symmetry operations that let it invariant.

We summarise the results of the action of symmetries on the elements of the four classes (α) , (β) , (γ) in figures 1.23, 1.24, 1.25 for (δ) The full figure becomes illegible. We can check that these ensembles are closed from the viewpoint of honeycomb symmetries as each element of a class has its image through symmetries within the class.

¹⁸ Y. Kosmann-Schwarzbach and F. Singer. *Groups and symmetries: from finite groups to Lie groups*. Universitext. Springer, New York, NY, 2010. OCLC: 297148428

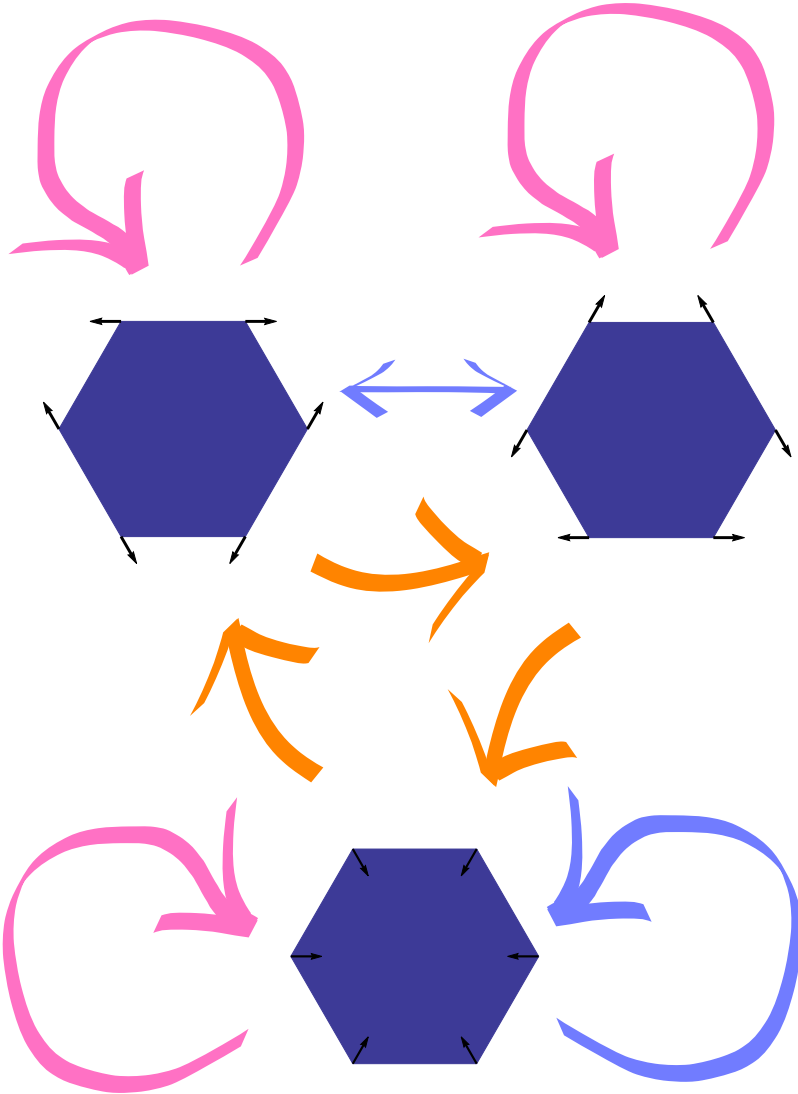


Figure 1.23: Operation of symmetries on the representants of class (α) . Blue arrows indicate the effect of reflection symmetry, orange arrows the effect of translation symmetry, pink arrows the effect of rotation symmetry.

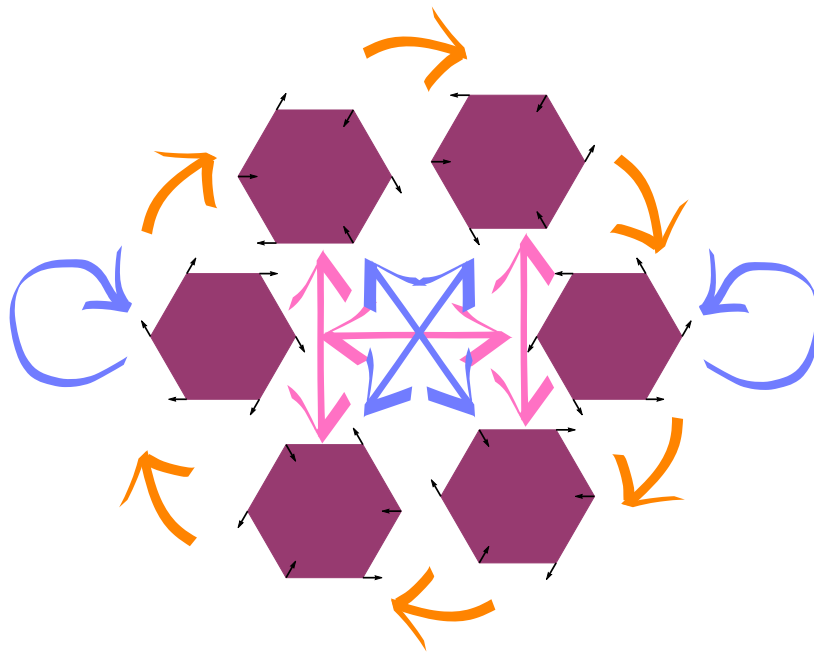


Figure 1.24: Operation of symmetries on the representants of class (β). Blue arrows indicate the effect of reflection symmetry, orange arrows the effect of translation symmetry, pink arrows the effect of rotation symmetry.

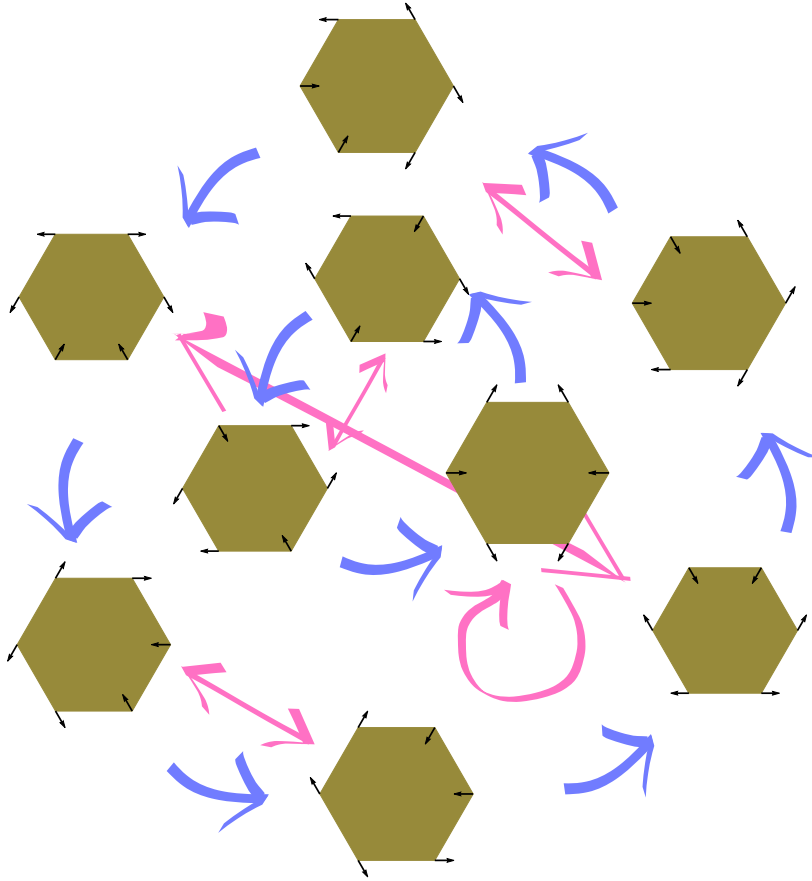


Figure 1.25: Operation of symmetries on the representants of class (β) . Blue arrows indicate the effect of reflection symmetry, orange arrows are not represented for the sake of clarity. Pink arrows the effect of rotation symmetry.

2

Numerical procedures

This chapter is devoted to our numerical methods. In section 2.1 we tell about our algorithm to minimise energy. In section 2.2 we explain how we compute stresses and elastic constants from our systems' potential energy function. In section 2.3 we explain how we apply a fixed stress to the material. Finally, in section 2.4 we go further into the code structure.

2.1 Energy minimisation

The previous chapter introduced a potential energy function of the non affine coordinates of the network. In this section we give details on our numerical procedure to apply a strain γ . We built our code on top of the existing work of Pierre Ronceray¹, the code concerned in this part pre-existed when I arrived in 2016.

To apply a finite strain to the network, we first move all sites affinely from their reference position

$$\mathbf{x}_i^0 \mapsto \mathbf{x}_i^0 + \underbrace{\gamma \mathbf{x}_i^0}_{=\mathbf{u}_i^{\text{aff}} \text{ affine displacement}} .$$

As a result, the site i feels a force $\mathbf{F}^i = -\nabla_{\mathbf{u}_i} \mathcal{U}$, where the ∇_i notation refers to a gradient with respect to the coordinates of site number i . To reach its equilibrium position, it needs to move to cancel this force. In order to do so, it could follow direction of \mathbf{F}_i in an overdamped motion², or follow Langevin dynamics to account of thermal fluctuations. However, we did not study the dynamics of this motion³ and we tried to reach equilibrium at least computational cost. Henceforth we minimise energy by means of a non linear conjugate gradient algorithm^{3,4}. This algorithm is implemented in the GNU standard library for C/C++ languages⁵. During this minimisation we impose the Lees-Edwards boundary conditions as a constraint on edges displacements.

Once we are given the set non affine displacements $\mathbf{u}^*(\gamma)$ of the microscopic degrees of freedom with respect to the affinely deformed state under

¹ P. Ronceray, C. P. Broedersz, and M. Lenz. Fiber networks amplify active stress. *Proceedings of the National Academy of Sciences*, Mar. 2016

² H. Goldstein, C. Poole, and J. Safko. *Classical Mechanics*. Addison Wesley, 2002

³ J. R. Shewchuk. An introduction to the conjugate gradient method without the agonizing pain. Technical report, Pittsburgh, PA, USA, 1994

⁴ R. Fletcher. *Practical Methods of Optimization; (2Nd Ed.)*. Wiley-Interscience, New York, NY, USA, 1987

⁵ M. Galassi, J. Davies, J. Theiler, B. Gough, G. Jungman, P. Alken, M. Booth, F. Rossi, and R. Ulerich. GNU Scientific Library

³ For the fibers networks we study, thermal fluctuations and inertia are negligible.

strain γ ⁶, we end up with a potential energy $\mathcal{U}^*(\gamma) = \mathcal{U}(\gamma, \mathbf{u}^*(\gamma))$ which corresponds to the minimal amount of work an operator would need to exert the strain γ from a zero energy configuration. This configuration may sometimes be fictitious since it could require to cut bonds and isolate subparts of the system.

2.2 Stresses and elastic constants

We saw in section 2.1 a protocol to minimise the potential energy of a system under strain. In this section we present two methods to compute stress and differential elastic moduli around a configuration with fixed strain and compare their benefits. The first method, similar to the one presented in⁷, is presented in subsection 2.2.2. This is the most natural for the physicist as it comes to apply an infinitesimal strain to test out the system's stiffness, however it shows issues concerning the choice of the amplitude of this perturbation. The second method in section 2.2.3 uses a mathematical structure not routinely used in physics : the *hyperdual* numbers. This method is less natural to implement, but enables systematic, reliable computations regardless of the specific nature of the considered system.

2.2.1 Definitions, Voigt basis

In section we defined $\mathcal{U}^*(\gamma) = \mathcal{U}(\gamma, \mathbf{u}^*(\gamma))$. We define the *stress* as the conjugate variable to the strain, divided by the initial volume V_0 (the initial area in 2D, the initial length in 1D) so as to get an intensive quantity :

$$\sigma_{ij} = -\frac{1}{V_0} \frac{\partial \mathcal{U}^*(\gamma)}{\partial \gamma_{ij}}$$

We define the *differential stiffness tensor* as the Hessian tensor per unit volume of $E^*(\gamma)$:

$$G_{ijkl} = -\frac{1}{V_0} \frac{\partial^2 \mathcal{U}^*(\gamma)}{\partial \gamma_{ij} \partial \gamma_{kl}} = \frac{\partial \sigma_{kl}}{\partial \gamma_{ij}}$$

Examples.

This general definitions applied to more restricted contexts reduce to the following :

- For a 1D system such as an Euler elastica (Fig. 2.1) of rest length ℓ_0 and end-to-end length ℓ , the strain $\gamma = \frac{\ell - \ell_0}{\ell_0}$ reduces to a scalar, the stress is obtained by derivatives rules for nested functions :

$$\begin{aligned} \sigma &= -\frac{1}{\ell_0} \frac{d\ell}{d\gamma} \frac{\partial \mathcal{U}^*(\ell)}{\partial \ell} \\ &= F \end{aligned}$$

which is the force along the filament induced by the compression.

⁶ Hereafter, the boldfont notation for a vector refers to a dN vector which concatenates coordinates of all sites. The star over a quantity indicates that it minimises potential energy under strain γ , thus it is a function of γ .

⁷ A. Lemaitre and C. Maloney. Sum Rules for the Quasi-Static and Visco-Elastic Response of Disordered Solids at Zero Temperature. *Journal of Statistical Physics*, Apr. 2006

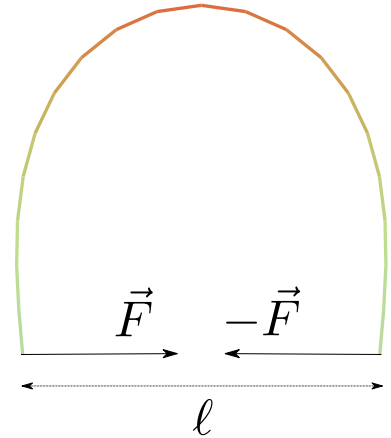


Figure 2.1: Example : Euler Elastica buckles under axial compression

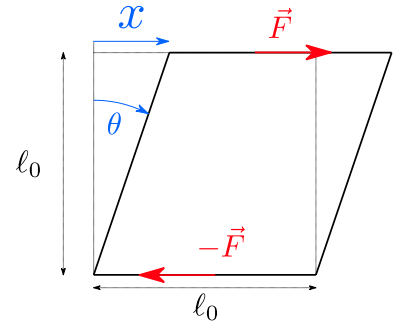


Figure 2.2: Example : Square under shear.

- For a 2D system such as a square of side ℓ_0 (Fig. 2.2) under shear

$$\gamma = \begin{pmatrix} 0 & \epsilon \\ 0 & 0 \end{pmatrix} = \frac{\epsilon}{\sqrt{2}} \left[\frac{1}{\sqrt{2}} \begin{pmatrix} 0 & 1 \\ 1 & 0 \end{pmatrix} + \frac{1}{\sqrt{2}} \begin{pmatrix} 0 & 1 \\ -1 & 0 \end{pmatrix} \right]$$

, we have $\epsilon = \tan(\theta) = \frac{x}{\ell_0}$, where x is the deviation of the upper side along y axis, thus :

$$\begin{aligned} \sigma_2 &= -\frac{\sqrt{2}}{V_0} \frac{\partial \mathcal{U}^*(\gamma)}{\partial \epsilon} \\ &= -\frac{\sqrt{2}\ell_0}{V_0} \frac{\partial \mathcal{U}^*(\gamma)}{\partial x} \\ &= \frac{\sqrt{2}}{\ell_0} F \end{aligned}$$

Equates the shear force on the system divided by its reference height.

- For a 3D system under isotropic compression $\gamma = \begin{pmatrix} -\alpha & 0 & 0 \\ 0 & -\alpha & 0 \\ 0 & 0 & -\alpha \end{pmatrix}$ we

have $V(\alpha) = V_0(1-\alpha)^3$ and $\frac{dV}{d\alpha} = -3V_0(1-\alpha)^2$

$$\begin{aligned} \sigma_\alpha &= -\frac{1}{V_0} \frac{\partial \mathcal{U}^*(\alpha)}{\partial \alpha} \\ &= 3(1-\alpha)^2 \frac{\partial \mathcal{U}^*(V)}{\partial V} \\ &= 3(1-\alpha)^2 P \end{aligned}$$

which equates the pressure up to a geometrical factor.

We also give examples of elastic moduli :

- We take the same 3D isotropic compression as before :

$$\begin{aligned} G_{\alpha,\alpha} &= -\frac{1}{V_0} \frac{\partial^2 \mathcal{U}^*(\alpha)}{\partial \alpha^2} \\ &= \frac{\partial [3(1-\alpha)^2 P]}{\partial \alpha} \\ &= 3(1-\alpha)^2 \frac{\partial P}{\partial \alpha} - 6(1-\alpha)P \\ &= -9V_0(1-\alpha)^4 \frac{\partial P}{\partial V} - 6(1-\alpha)P \\ &= -9(1-\alpha)V \frac{\partial P}{\partial V} - 6(1-\alpha)P \end{aligned}$$

Which corresponds to the bulk modulus $-V \frac{dP}{dV}$ around the reference configuration for which $\alpha = 0$, and differs from it by a prestress additive term and a multiplicative geometrical factor away from the reference.

In the definitions above, we implicitly referred to tensor components in the *Voigt* basis. This basis is a convenient choice to avoid dealing with fourth rank tensors. Furthermore this basis is well suited to understand tensor's behavior under rotations as the basis tensors obey simple transformation rules under rotations.

In 2D, a rank 2 tensor can be written :

$$\begin{aligned} T &= \begin{pmatrix} T_{11} & T_{12} \\ T_{21} & T_{22} \end{pmatrix} \\ &= T_0 \underbrace{\frac{1}{\sqrt{2}} \begin{pmatrix} 1 & 0 \\ 0 & 1 \end{pmatrix}}_{e_0} + T_1 \underbrace{\frac{1}{\sqrt{2}} \begin{pmatrix} 1 & 0 \\ 0 & -1 \end{pmatrix}}_{e_1} + T_2 \underbrace{\frac{1}{\sqrt{2}} \begin{pmatrix} 0 & 1 \\ 1 & 0 \end{pmatrix}}_{e_2} + T_3 \underbrace{\frac{1}{\sqrt{2}} \begin{pmatrix} 0 & -1 \\ 1 & 0 \end{pmatrix}}_{e_3} \end{aligned}$$

or, with the Einstein summation convention over repeated indices $T = T_{ij}e_{ij} = T_I e_I$, where e_{ij} are the elementary matrices in canonical basis, and the e_I are the elementary matrices in Voigt basis. They allow to represent a 2D rank 2 tensor under the form of a length 4 vector, and a rank 4 tensor as a 4×4 matrix. The Voigt basis allows to read more easily the symmetry properties of a tensor, indeed e_0 is a generator for isotropic compression, e_2 and e_3 are generators for shear, and e_1 is a generator for rotation⁸. Then, we can interpret the components of the elastic tensor as follows : G_{00} is the coupling of isotropic compression with itself, G_{02} is the coupling between compression and shear, G_{03} is the coupling between compression and rotation, and so on and so forth for the other components. If the system is isotropic, we can say that G_{I3} and G_{3I} should vanish for all I 's since there is no energetic cost to bulk rotation. If it is achiral G_{02} and G_{12} may not vanish as the compression along an axis can induce shear along an other one.

This notation amounts to decomposing the space of 2 rank tensors into irreducible representations of the group of rotations, and to write tensors in a corresponding basis. Sometimes, the group of continuous rotations doesn't leave the material invariant, and Voigt basis will not simplify the expression of G_{IJ} . Despite our networks display fewer symmetries, we will stick with Voigt basis, nonetheless we will discuss more deeply the question of symmetry in the reference units cells (α) , (β) , (γ) and (δ) in section 3.4.1.

2.2.2 Preliminary attempt through finite differences calculations

Given the definitions in the section above, the evaluation of our observables boils down to the computation of numerical derivatives of a function f of several variables x_i ⁹. In this part we present an algorithm to numerically estimate derivatives of a generic function by computing finite differences. We provide a generating formula for arbitrary order formulae.

First, let f be a function of a single variable x . The multi-variable generalisation involves more formalism without fundamental conceptual changes so we won't address it.

⁸ We make the difference between basis matrices e_{XX} by using either a pair (ij) of indices or a single capital index I .

⁹ f being \mathcal{U}^* and the x_i the components γ_{ij} .

To estimate derivatives of f around a point x_0 , we start from a Taylor expansion, which provides a link between finite steps and differential calculus :

$$f(x_0 + h) = \sum_{n=0}^{\infty} \frac{f^{(n)}(x_0)}{n!} h^n$$

This formula being exact if $|h|$ is smaller than the convergence radius of the right hand side series.

We can then estimate the derivative thanks to the Taylor expansion of f around x_0

$$f'(x_0) = \frac{f(x_0 + h) - f(x_0)}{h} + \mathcal{O}(h^2)$$

up to the order h^2 . If we implement it however we experiment several issues :

- If h is too large, the error of order h^2 becomes predominant.
- Even if we have an analytical expression for f , we will compute differences between two really close quantities $f(x_0)$ and $f(x_0 + h)$ as h decreases. This is a case in which we face numerical cancelation of least significant digits. It is often advised not to take h below $\sqrt{\epsilon}$ where ϵ is the machine precision, or the precision on f ¹⁰. This error worsens as we compute higher order derivatives. Typically machine precision is 10^{-14} in floating point double precision numbers.
- If we don't have an analytical expression for f , (for instance in our case \mathcal{U}^* is the result of a conjugate gradient minimisation procedure) then f is evaluated with some relative precision $\frac{\delta f}{f}$ which can be larger than machine precision. This problem will manifest itself at higher finite steps than cancelation error and lower even more the admissible range for h .

One way to circumvent these issues is to make use of higher precision finite differences formulae, which we derive below.

For this we adopt an operatorial viewpoint in finite derivatives : we introduce the differentiation operator $D : f \mapsto f'$ and the finite difference operator Δ_h defined by $\Delta_h : f \mapsto \Delta_h[f] : x \mapsto f(x + h) - f(x)$.

The Taylor expansion can be re-expressed operationally as :

$$(\mathbb{1} + \Delta_h)[f] = \exp(hD)[f] = \left(\sum_{n=0}^{\infty} \frac{h^n D^n}{n!} \right) [f]$$

where the n -th power has to be understood as n iterations of the operator and the exponential is an operator exponential defined by its series expansion¹¹.

If we further introduce the central difference operator $\delta_h = \Delta_h - \Delta_{-h}$, we will cancel even terms in the series, we will see in what follows that it improves the precision in formulae.

$$\delta_h[f] = 2 \sinh(hD)[f] = \left(\sum_{p=0}^{\infty} \frac{h^{2p+1} D^{2p+1}}{(2p+1)!} \right) [f]$$

¹⁰ S. D. Conte and C. d. Boor. *Elementary numerical analysis: an algorithmic approach*. International Series in pure and applied mathematics. McGraw-Hill, New York, 3. ed edition, 1987. OCLC: 256318941

¹¹ E. B. Davies. *Liner Operators And Their Spectra*

In this formalism, our problem to express the operator D as a function of finite differences Δ_h reduces to an operator inversion. We can perform this by inverting the sinh series. This is an infinite system of equations to solve for the coefficients of the unknown inverse series whose solutions is given by the Argsh series :

$$D[f] = \frac{1}{h} \text{Argsh} \left(\frac{\delta_h}{2} \right) [f] = \frac{1}{h} \sum_{p=0}^{\infty} \frac{a_n}{2^n} \delta_h^n [f]$$

where the a_n are tabulated Taylor coefficients of the Argsh series expansion.

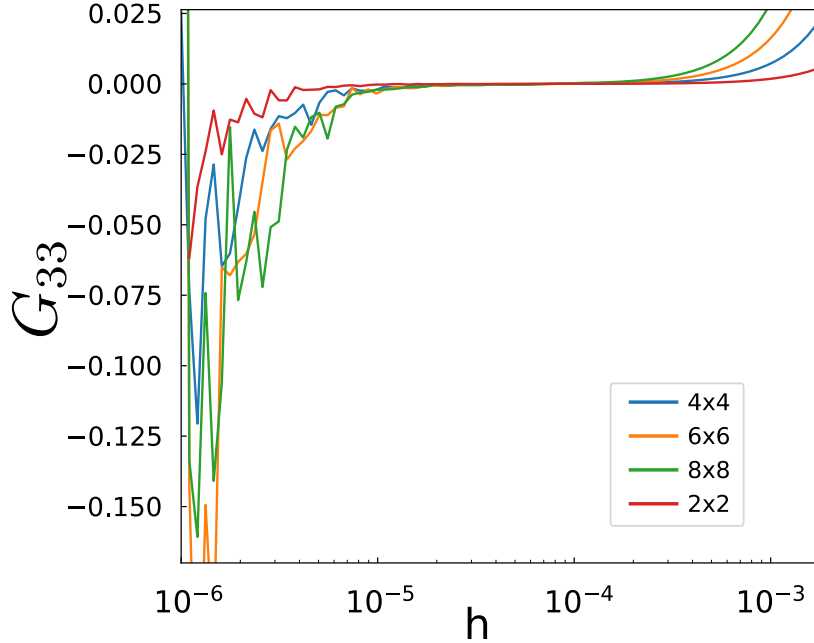


Figure 2.3: Estimation of the elastic modulus G_{33} (in Voigt basis: coupling between rotation and rotation. We know this modulus should vanish, and use it as a benchmark to validate algorithms) by a finite difference formula accurate up to order h^2 in a honeycomb lattice, prestress in geometry 2. We notice that the accuracy range for h depends on the number of cells (2×2 to 8×8) of the network. This is because conjugate gradient guarantees a precision on positions in configuration space, the errors are then propagated to the potential energy, which contains more and more terms as we increase system's size.

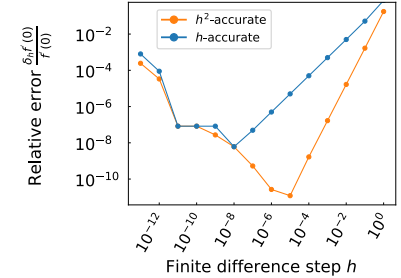


Figure 2.4: Finite difference error in the calculus of a first derivative on the test function $x \rightarrow e^x$, with h accurate formula and h^2 accurate formula. When h is too high, we accumulate an error of h or h^2 according to the Taylor expansion. When h goes to low, the relative error increases again due to cancellation error.

If we look for formulas to compute second derivatives, we merely iterate the operator D and its approximations twice. This could look like a time-consuming operation, but it can be fully automated, and the coefficients are calculated before the actual computations are made. Typically, we worked with the following h^2 accurate formulas:

$$\begin{cases} f'(x_0) = \frac{1}{h} \delta_h [f](x_0) + \mathcal{O}(h^2) = \frac{f(x_0+h) - f(x_0-h)}{2h} + \mathcal{O}(h^2) \\ f''(x_0) = \frac{1}{h^2} \delta_h^2 [f](x_0) + \mathcal{O}(h^2) = \frac{f(x_0+2h) - 2f(x_0) + f(x_0-2h)}{4h^2} + \mathcal{O}(h^2) \end{cases} \quad (2.1)$$

We computed numerically the first and second derivatives of the exponential $x \rightarrow e^x$ as a test function in 2.4 and 2.5 where we took two test functions.

The latter higher order formulas allow in principle a errors in derivative evaluations since they allow use of larger steps h , which wouldn't be affected by finite difference error. In practice, we should use the lowest order formula that allows an range for h where finite-difference error and cancellation error

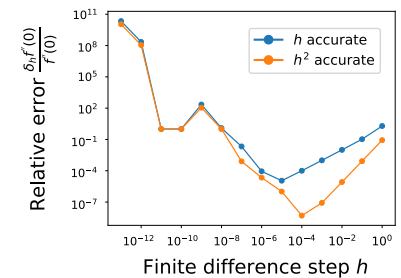


Figure 2.5: Same thing for second derivative. We see that cancellation error gets more dramatic than for first derivatives since the relative differences eventually diverges.

are simultaneously negligible. For example, an order h^2 formula is enough in fig. 2.3, thus we don't use order 3 and above formulae.

However, a limitation of this technique is that the step h should be adjusted for better precision depending on the function you compute the derivatives of, i.e. for us the physical system you are studying. Typically, if we change system size, parameters in the potential energy, geometry, or we consider different elastic constants, the choice of h should change. This limitation makes systematic studies difficult, for this reason we employ the method detailed in section 2.2.3.

2.2.3 Elegant approach : using hyperdual numbers

The accuracy problems in the previous section mainly comes from taking differences of close quantities that are only known with a finite accuracy. We present here an extension of real numbers that enables computation of derivatives without such differences.

For this, let us introduce the set of *dual*¹² numbers \mathbb{D} as a vector space of dimension 2 on \mathbb{R} with basis vectors noted¹³ 1 and ϵ . The vector space structure provides \mathbb{D} with an operation $+$, and an operation of multiplication by a real number, it enables to construct all the elements of the form $a + \epsilon b$, $(a, b) \in \mathbb{R}^2$. Now, we define an operation \times between dual numbers by their multiplication table in 2.6. By construction, the operations $+$ and \times reduce to their usual forms between real numbers. The algebraic construction that we just made is called a *field extension* of \mathbb{R} , which is nothing but extending a set to a larger one with compatible algebraic operations!¹⁴

As we would do with complex numbers, we define the operations \Re and \mathfrak{E} that take respectively real part and epsilon part of a dual number, they are mere projectors along components on the representation space.

We also define all the usual functions on \mathbb{D} by their series expansions:

$$\forall x \in \mathbb{D}, f(x) = \sum_{n=0}^{\infty} a_n x^n$$

Then it naturally follows that,

$$\begin{aligned} \forall x \in \mathbb{R}, f(x + \epsilon) &= \sum_{n=0}^{\infty} a_n (x + \epsilon)^n \\ &= \sum_{n=0}^{\infty} a_n (x^n + n\epsilon x^{n-1}) \\ &= \sum_{n=0}^{\infty} a_n x^n + \epsilon \sum_{n=1}^{\infty} n a_n x^{n-1} \\ &= f(x) + \epsilon f'(x) \end{aligned}$$

where we used the hyperdual number properties, making $(x + \epsilon)^n$ trivial to compute as its Newtons' expansion only contains two terms.

¹² A. A. Harkin and J. B. Harkin. Geometry of Generalized Complex Numbers. *Mathematics Magazine*, Apr. 2004

¹³ One way to represent \mathbb{D} is to take $\mathbb{D} = \mathbb{R}^2$, $1 = (1, 0)$ and $\epsilon = (0, 1)$. This enables us to represent them in $2D$ space, but isn't necessary to study the purely algebraic properties that we are interested in here.

¹⁴ An other example of a field extension is the field of complex numbers \mathbb{C} , but it is not the only choice !

\times	1	ϵ
1	1	ϵ
ϵ	ϵ	0

Figure 2.6: Multiplication table for dual numbers.

Finally, a way to compute a derivative is given by $f'(x_0) = \mathfrak{E} [f(x_0 + \epsilon)]$ which doesn't involve any finite difference operation !

It is worth noting that this relation is *exact*. In other terms, our generalized operations embed rules for *automatic differentiation*¹⁵. To benefit from it, we just need to implement an hyperdual class, the overloaded operations associated to it, and to define the usual functions of interest. We used Jeffrey Fike's C++ implementation

However dual numbers enable only first derivatives calculations, and elastic moduli are quantities of order 2. We thus proceed to a new field extension with basis vectors $1, \epsilon_1, \epsilon_2$ and $\epsilon_1\epsilon_2$. The multiplication table for it is presented in table 2.7, we call these number hyperdual numbers, we note their set \mathbb{H} . By the same generalizations as before, we can show that :

$$\begin{aligned} \forall x \in \mathbb{R}, f(x + \epsilon_1 + \epsilon_2) &= \sum_{n=0}^{\infty} a_n (x + \epsilon_1 + \epsilon_2)^n \\ &= \sum_{n=0}^{\infty} a_n \left(x + n a_n (\epsilon_1 + \epsilon_2) + \frac{n(n-1)}{2} a_n \epsilon_1 \epsilon_2 \right) \\ &= f(x) + (\epsilon_1 + \epsilon_2) f'(x) + \frac{1}{2} f''(x) \epsilon_1 \epsilon_2 \end{aligned}$$

This result is again exact, by construction. Henceforth, this new field extension allows us to perform automatic differentiation up to order 2. This process can be extended to higher order but multiplications get heavier each time : we need find a tradeoff between computational time and full knowledge of a function. Hyperdual derivation remains much faster than symbolic differentiation.

Example : We use this method to compute the first and second derivatives of the test function:

$$f(x) = e^{\sqrt{2+\sin(x)}}$$

which has been chosen because it will test out rules for nested derivatives computed thanks to hyperdual numbers.

To perform our tests, we can compute explicitly :

$$\begin{aligned} f'(x) &= \frac{e^{\sqrt{2+\sin(x)}} \cos(x)}{2\sqrt{2+\sin(x)}} \\ f''(x) &= \frac{e^{\sqrt{2+\sin(x)}} (-2\sin(x)(2+\sin(x)) + \cos^2(x)(\sqrt{2+\sin(x)} - 1))}{4(2+\sin(x))^{3/2}} \end{aligned}$$

These formulae being used in figures 2.8 and 2.9.

Final algorithm :

At this stage, our issue remains unsolved because we don't have an analytic form for $E^*(\gamma)$. Indeed, $E^*(\gamma)$ is defined implicitly by the following set of equations :

$$\begin{cases} E^*(\gamma) = E(\gamma, \mathbf{u}_i(\gamma)) \\ \nabla_{\mathbf{u}} E(\gamma, \mathbf{u}) = 0 \implies \mathbf{u} = \mathbf{u}^*(\gamma) \end{cases}$$

¹⁵ A. G. Baydin, B. A. Pearlmutter, A. A. Radul, and J. M. Siskind. Automatic differentiation in machine learning: a survey. *arXiv:1502.05767 [cs, stat]*, Feb. 2015. arXiv: 1502.05767

Jeffrey Fike's C++ implementation of hyperdual numbers is available at <http://adl.stanford.edu/hyperdual/#Code>

\times	1	ϵ_1	ϵ_2	$\epsilon_1\epsilon_2$
1	1	ϵ_1	ϵ_2	$\epsilon_1\epsilon_2$
ϵ_1	ϵ_1	0	$\epsilon_1\epsilon_2$	0
ϵ_2	ϵ_2	$\epsilon_1\epsilon_2$	0	0
$\epsilon_1\epsilon_2$	$\epsilon_1\epsilon_2$	0	0	0

Figure 2.7: Multiplication table for hyperdual numbers.

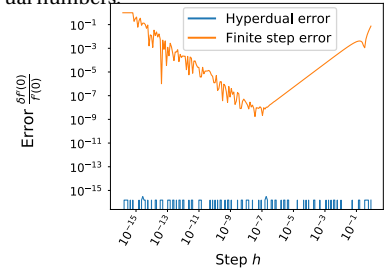


Figure 2.8: We computed relative differences of $(f(h) - f(0))/h$ and $f'(0)$ on one hand, of $\mathfrak{E}_1 [f(0 + h\epsilon_1)]/h$ on the other hand. For the finite differences formula, we see a cancellation error-dominated regime, and a finite step error-dominated regime. Hyperdual calculation on the other side is always accurate up to machine precision, without a need to adjust h !

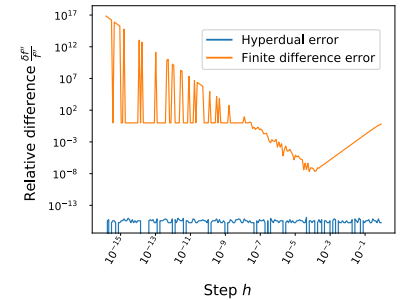


Figure 2.9: We computed relative differences of $\frac{f(2h) - 2f(0) + f(-2h)}{4h^2}$ and $f''(0)$ on one hand, of $\frac{\mathfrak{E}_{12}[f(0+h_1\epsilon_1+h_2\epsilon_2)]}{h_1h_2}$ on the other hand. For the finite differences formula, we see a cancellation error-dominated regime, and a finite step error-dominated regime. Hyperdual calculation on the other side is always accurate up to machine precision, without need to adjust h !

Where $\mathbf{u}^*(\gamma)$ is guaranteed to be a local solution of the zero force condition for smooth enough E functions. On the other hand the γ dependency in E is imposed by boundary conditions.

Therefore our problem is to compute second derivatives of a function defined implicitly. If we step back to genericity, we would like to compute derivatives of f defined by :

$$\begin{cases} f(x) = F(x, \mathbf{u}^*(x)) \\ \mathbf{G}(x, \mathbf{u}) = \mathbf{0} \implies \mathbf{u} = \mathbf{u}^*(x), \end{cases}$$

$\mathbf{u}^*(x)$ being two local differentiable expressions guaranteed to exist by the implicit function theorem through the $\mathbf{G}(x, \mathbf{u}) = \mathbf{0}$ condition. The cartoon in Fig. 2.10 shows a typical case. In particular, \mathbf{G} doesn't need to be related to derivatives of F , it only needs to define an implicit \mathbf{u}^* . From the above relation we can deduce relations between derivatives of \mathbf{u}^* :

$$\begin{cases} \frac{df}{dx}(x) = \frac{\partial F}{\partial x} + \nabla_{\mathbf{u}} F \cdot \frac{d\mathbf{u}^*}{dx} \\ \frac{\partial \mathbf{G}}{\partial x} + \left(\frac{d\mathbf{u}^*}{dx} \cdot \nabla_{\mathbf{u}} \right) \mathbf{G} = \mathbf{0} \end{cases} \quad (2.2)$$

and its second derivatives :

$$\begin{cases} \frac{d^2 f}{dx^2}(x) = \frac{\partial^2 F}{\partial x^2} + 2 \frac{\partial \nabla_{\mathbf{u}} F}{\partial x} \cdot \frac{d\mathbf{u}^*}{dx} + \left(\left(\frac{d\mathbf{u}^*}{dx} \cdot \nabla_{\mathbf{u}} \right) \nabla_{\mathbf{u}} F \right) \cdot \frac{d\mathbf{u}^*}{dx} + \nabla_{\mathbf{u}} F \cdot \frac{d^2 \mathbf{u}^*}{dx^2} \\ \mathbf{0} = \frac{\partial^2 \mathbf{G}}{\partial x^2} + 2 \left(\frac{d\mathbf{u}^*}{dx} \cdot \nabla_{\mathbf{u}} \right) \frac{\partial \mathbf{G}}{\partial x} + \left(\frac{d^2 \mathbf{u}^*}{dx^2} \cdot \nabla_{\mathbf{u}} \right) \mathbf{G} + \left(\frac{d\mathbf{u}^*}{dx} \cdot \left(\left(\frac{d\mathbf{u}^*}{dx} \cdot \nabla_{\mathbf{u}} \right) \nabla_{\mathbf{u}} \right) \right) \mathbf{G} \end{cases} \quad (2.3)$$

where all occurrences of F , \mathbf{G} and their derivatives are evaluated in $(x, \mathbf{u}^*(x))$, and all occurrences of \mathbf{u}^* and its derivatives are evaluated at x .

Henceforth, we notice that $\frac{d\mathbf{u}^*}{dx}$ is solution of the linear system (2.2) and the second derivatives $\frac{d^2 \mathbf{u}^*}{dx^2}$ are solutions of the linear system (2.3).

Thanks to hyperdual numbers properties, these two systems can be rephrased as follows for two unknown vectors \mathbf{a} and \mathbf{c} :

$$\begin{cases} \frac{df}{dx}(x) = \mathfrak{E}_1 \left[f \left(x + \epsilon_1, \mathbf{u}^*(x) + \epsilon_1 \frac{d\mathbf{u}^*}{dx}(x) \right) \right] \\ \mathbf{0} = \mathfrak{E}_1 \left[\mathbf{G} \left(x + \epsilon_1, \mathbf{u}^*(x) + \epsilon_1 \mathbf{a} \right) \right] \implies \mathbf{a} = \frac{d\mathbf{u}^*}{dx}(x) \end{cases} \quad (2.4)$$

and

$$\begin{cases} \frac{d^2 f}{dx^2}(x) = \mathfrak{E}_{12} \left[f \left(x + \epsilon_1 + \epsilon_2, \mathbf{u}^*(x) + \epsilon_1 \frac{d\mathbf{u}^*}{dx}(x) + \epsilon_2 \frac{d\mathbf{u}^*}{dx}(x) + \epsilon_1 \epsilon_2 \frac{d^2 \mathbf{u}^*}{dx^2}(x) \right) \right] \\ \mathbf{0} = \mathfrak{E}_{12} \left[\frac{\partial \mathbf{G}}{\partial x} \left(x + \epsilon_1 + \epsilon_2, \mathbf{u}^*(x) + \epsilon_1 \frac{d\mathbf{u}^*}{dx}(x) + \epsilon_2 \frac{d\mathbf{u}^*}{dx}(x) + \epsilon_1 \epsilon_2 \mathbf{c} \right) \right] \\ \implies \mathbf{c} = \frac{d^2 \mathbf{u}^*}{dx^2}(x) \end{cases} \quad (2.5)$$

The power of hyperdual numbers manifests in two respects :

- Hyperdual numbers automate the cumbersome calculation made on equations (2.2) and (2.3). The main point in making these calculations was to prove that the systems to solve is linear.

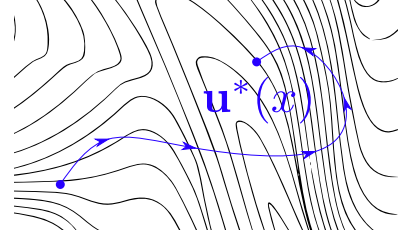


Figure 2.10: The microscopic degrees of freedom \mathbf{u} evolve in the energy landscape of F , and this landscape itself evolves with x . \mathbf{u} follows the curve $\mathbf{u}^*(x)$, local solution of $\mathbf{G}(x, \mathbf{u}) = \mathbf{0}$. The derivative of f taken at x has two contributions : \mathbf{u} moves along $\mathbf{u}^*(x)$ in a fixed landscape, and the landscape evolves at point $\mathbf{u}^*(x)$ between x and $x + dx$. For second derivative, the graphical interpretation would get more convoluted, but the algebra in equation 2.3 says nothing more.

- They provide a way to compute the second derivative of an implicit function up to the precision of the linear solver. This is done without finite differences issues. Moreover the precision of the linear solver remains the same for first order derivatives and second order ones. Finite differences methods on the contrary worsened as we went higher in derivatives order.

This part was a proof of concept in the one dimensional case, it didn't explain how to solve the problem in a concrete case, it only shows that a system of equations can be obtained for the derivatives, without computing differences, it proves that this system is linear. Now we will translate it to our original problem of computing elastic constants.

If we step back to our original problem, the variable x changes from a single variable to a set of matrix coefficients γ_I , I being a Voigt index. This doesn't introduce conceptual complexity : we just lose the geometrical interpretation of fig. 2.10 since the implicit curve becomes an implicit hypersurface in a higher dimension space. f becomes \mathcal{U}^* , F becomes \mathcal{U} and \mathbf{G} becomes $\nabla_{\mathbf{u}}\mathcal{U}$ (this gradient being taken with respect to all dN coordinates in configuration space).

$$\begin{cases} \mathcal{U}^*(\gamma) = \mathcal{U}(\gamma, \mathbf{u}^*(\gamma)) \\ \nabla_{\mathbf{u}}\mathcal{U}(\gamma, \mathbf{u}) = \mathbf{0} \implies \mathbf{u} = \mathbf{u}^*(\gamma) \end{cases}$$

We first find $\mathbf{u}^*(\gamma)$ by using a conjugate gradient algorithm. Then, we introduce the variables \mathbf{a}^I , \mathbf{b}^J , and \mathbf{c}^{IJ} as unknown vectors, we solve the linear system of equations :

$$\begin{cases} \underline{\mathcal{U}^*}(\gamma + \epsilon_1 \mathbf{e}_I + \epsilon_2 \mathbf{e}_J) = \underline{\mathcal{U}}(\gamma + \epsilon_1 \mathbf{e}_I + \epsilon_2 \mathbf{e}_J, \mathbf{u}^* + \epsilon_1 \mathbf{a}^I + \epsilon_2 \mathbf{b}^J + \epsilon_1 \epsilon_2 \mathbf{c}^{IJ}) \\ 0 = \underline{\nabla_{\mathbf{u}}\mathcal{U}}(\gamma + \epsilon_1 \mathbf{e}_I + \epsilon_2 \mathbf{e}_J, \mathbf{u}^* + \epsilon_1 \mathbf{a}^I + \epsilon_2 \mathbf{b}^J + \epsilon_1 \epsilon_2 \mathbf{c}^{IJ}) \end{cases} \quad (2.6)$$

The underlined quantities being understood as hyperdual versions of the corresponding real quantities. The e_I are elementary Voigt matrices. They allow a virtual deformation of the system in a hyperdual direction. The real parts equality is guaranteed by the conjugate gradient solution, the \mathfrak{E}_1 and \mathfrak{E}_2 equalities are guaranteed by a linear solving, they provide the stresses σ_I and σ_J . Finally, the \mathfrak{E}_{12} part is solution of a second linear problem, it provides the stiffness coefficient K_{IJ} . To build the full stiffness matrix, we need to call this solver for all (I, J) non trivial pairs. The trivial pairs being those associated to rotations, and half of the (J, I) pairs, which equate the (I, J) pairs.

More compactly, the solution provides :

$$\left\{ \begin{array}{l} \mathbf{a}^I = \frac{d\mathbf{u}^*}{d\gamma_I} \\ \mathbf{b}^J = \frac{d\mathbf{u}^*}{d\gamma_J} \\ \mathbf{c}^{IJ} = \frac{d^2\mathbf{u}^*}{d\gamma_I d\gamma_J} \\ \mathfrak{R}[\mathcal{U}^*(\gamma + \epsilon_1 \mathbf{e}_I + \epsilon_2 \mathbf{e}_J)] = \mathcal{U}^*(\gamma) \\ \mathfrak{E}_1[\mathcal{U}^*(\gamma + \epsilon_1 \mathbf{e}_I + \epsilon_2 \mathbf{e}_J)] = -V_0 \sigma_I \\ \mathfrak{E}_{1,2}[\mathcal{U}^*(\gamma + \epsilon_1 \mathbf{e}_I + \epsilon_2 \mathbf{e}_J)] = V_0 K_{IJ} \end{array} \right. \quad (2.7)$$

This algorithm is original, it has been designed by the author of this thesis.

2.2.4 Comparing the two methods

To conclude, we compare the two above mentioned methods to compute elastic moduli. First of all we can reproduce the results of fig. 2.3 concerning the coupling between rotation and rotation. Taking the same system, and computing the same benchmark, the hyperdual algorithm gave $0.145538 \cdot 10^{-14}$ for a 2×2 system, $0.985432 \cdot 10^{-14}$ for a 4×4 system, and $0.463597 \cdot 10^{-14}$ for a 8×8 system, validating the benchmark up to machine precision for this elastic constant.

On the other hand we can study a chain of springs lying along x axis, they all have a rest length of 1, and their stiffnesses alternate between μ_1 and μ_2 . This system is the simplest system we can build that would exhibit non-affine displacement when compressed, it will help provide a best case estimate for the accuracy the hyperdual method. The accuracy of linear solver being limited by the accuracy of the linear solver. For the system of equation not no be trivial, we had to test on a system displaying non-affine displacement, we thought this one was appropriate.

We will study an unit cell of this system made of two springs, and apply to it a strain γ through Lees-Edwards periodic boundary conditions as represented in fig. 2.11.

The potential energy of this unit cell reads :

$$\mathcal{U}(\ell_1, \ell_2) = \frac{\mu_1}{2} (\ell_1 - 1)^2 + \frac{\mu_2}{2} (\ell_2 - 1)^2$$

The Lees-Edwards boundary constraint reads:

$$\ell_1 + \ell_2 = 2(1 - \gamma)$$

Thus the energy

$$\mathcal{U}(\ell_1, \gamma) = \frac{\mu_1}{2} (\ell_1 - 1)^2 + \frac{\mu_2}{2} (1 - 2\gamma - \ell_1)^2$$

We can minimise it with respect to ℓ_1 so as to get at equilibrium

$$\left\{ \begin{array}{l} \ell_1 = 1 - \frac{2\gamma\mu_2}{\mu_1 + \mu_2} \\ \ell_2 = 1 - \frac{2\gamma\mu_1}{\mu_1 + \mu_2} \end{array} \right.$$

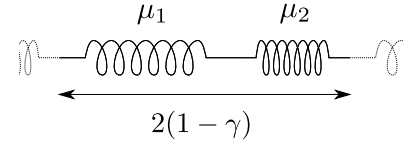


Figure 2.11: Unit cell of a chain of springs with stiffnesses μ_1 and μ_2 , $\mu_1 > \mu_2$ under compression. They are in series, so their compliances add up.

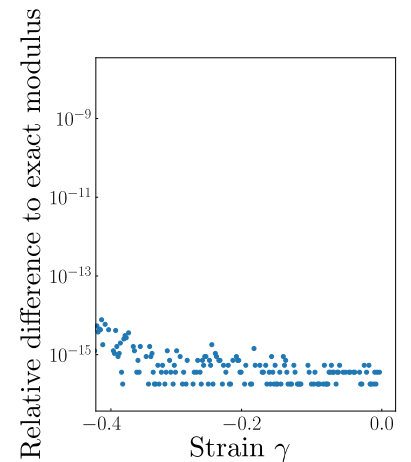


Figure 2.12: Relative difference between analytic result and hyperdual calculation of the compression modulus. $\kappa = 10000$, $\mu_1 = 10$ and $\mu_2 = 1000$. This gives a best case estimate.

so that

$$\mathcal{U}^*(\gamma) = \gamma^2 \frac{2\mu_1\mu_2}{\mu_1 + \mu_2}$$

Finally, the bulk modulus reads :

$$\begin{aligned} G &= \frac{1}{2} \frac{d^2 \mathcal{U}^*(\gamma)}{d\gamma^2} \\ &= \frac{2\mu_1\mu_2}{\mu_1 + \mu_2} \end{aligned}$$

In other terms, the chain of springs associated in series can be replaced by a chain of identical springs whose compliance is the average of compliances of the springs¹⁶, namely $\frac{1}{\mu_{eq}} = \frac{1}{2} \left(\frac{1}{\mu_1} + \frac{1}{\mu_2} \right)$.

We can use this exact expression to compute relative differences between the true result and the hyperdual result, for this computation we took $\kappa = 10000$, $\mu_1 = 20$ and $\mu_2 = 2000$, we show the result in fig. 2.12. This example shows that a best case approximation for the accuracy of the method is machine precision, even in presence of non affine displacement, provided the linear inversion reaches such a precision. In practice, we set the convergence criterion on the linear inversion to 10^{-10} for systems with more degrees of freedom.

This reliability is made possible to the price of a more costly evaluation of energy as each call to a mathematical function becomes calls to several functions, each hyperdual multiplication requires 9 real multiplications and 5 real additions, and each hyperdual addition requires 4 real additions. The easiest way to count it is to look directly at the Fick's library we mentioned above.

2.3 Apply an external stress to the material

When we considered systems with residual internal stresses, we faced the necessity to find a configuration with vanishing average stress. Indeed as soon as we apply stress at a microscopic level on forks, the reference configuration experiences stresses on its edges and tends to contract. In this section we address the more general issue to find the strain that ensures an imposed boundary stress. For this we will make a minimisation in two steps, the first step relaxes microscopic degrees of freedom through conjugate gradient, as described before. The second step takes the output of the first simulation to compute $\mathcal{U}^*(\gamma)$ and equates its derivatives to the applied stress.

2.3.1 Exert a finite stress by using Nelder-Mead algorithm

We want to apply a boundary stress to the edges of a material instead of a strain. For this, we need to consider the coefficients of γ as degrees of freedom and to minimise the following energy with respect to \mathbf{u}_i and γ :

$$H(\Sigma, \{\gamma_I, \mathbf{u}\}) := E(\gamma, \mathbf{u}) - \gamma_I \Sigma_I$$

¹⁶ The compliance is the inverse of the stiffness.

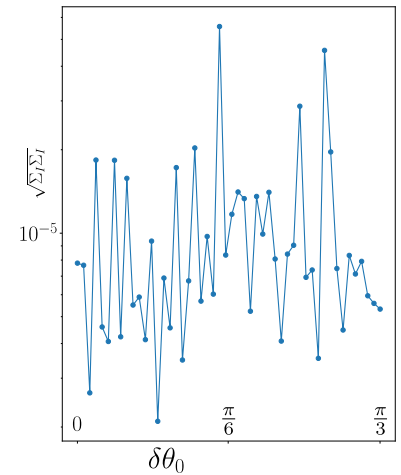


Figure 2.13: Residual stress on the boundaries of the geometry (α), after Nelder-Mead minimisation to find a zero stress configuration. We varied $\delta\theta_0$ from 0 to $\frac{\pi}{3}$ in 50 steps.

This is done in two steps : a first step uses conjugate gradient to obtain $E^*(\gamma)$ and a second one uses a Nelder-Mead algorithm¹⁷ to minimise

$$H^*(\Sigma, \gamma) := E^*(\gamma) - \gamma_I \Sigma_I$$

with respect to γ .

In particular we use it to find zero stress states once the prestress parameters in our system have been settled. It is of major importance if you consider the fact that the zero stress state of a system can involve shear with respect to the honeycomb configuration.

To validate the accuracy of the procedure, we took the geometry (α) with the standard set of parameters discussed on chapter 1, for $\delta\theta_0$ going from 0 to $\frac{\pi}{3}$. We looked for the strain which corresponded to a zero boundary stress and plotted the squared norm of this stress $\sqrt{\Sigma_I \Sigma_I}$ (Einstein summation over Voigt indices is involved) as a function of $\delta\theta_0$. The results are presented in fig. 2.13. This method converges generally towards boundary a stress of order 10^{-5} . Typically, when we obtain a convergence above 10^{-4} , we reiterate the Nelder-Mead minimisation after adding a random infinitesimal strain to make sure of the reference configuration and reduce the residual stress on edges. It is worth noting that this is an empirical decision. We must say that the measurement above is absolute and not relative, in practice we should compare the residual stress after minimisation to a typical scale of stress. For instance this scale can be the stress induced on the boundaries when we apply a strain. Here, as we increase $\delta\theta_0$ from 0 to $\frac{\pi}{3}$, $\sqrt{\Sigma_I \Sigma_I}$ goes typically from 0 to 150 in the initial configuration, meaning Nelder-Mead algorithm relaxes the stress by 7 orders of magnitude closer to 0 : the algorithm does the job and we didn't try to improve it !

However, we must notice that this two-steps algorithm is time consuming because the time required to compute $\mathcal{U}^*(\gamma)$ grows with system's size, henceforth, we can't use it systematically of large systems.

2.4 Code structure

In this section we discuss the structure of our code. We think it can help future use of it and serve as a simplified user manual. It can also help the reader find appropriate tools to write extensions of the code, to create a new one from it, or to learn about tools/libraries for other code projects.

Before we present the code into further details, we will have an overview of its structure. We run the code as soon as we want to simulate a fiber network and compute mechanical observables about it. For this we write an XML input file, we execute the code either locally or on a computation cluster, we retrieve results into text/binary files, and we analyse them by means of Python scripts.

Concerning coding languages, we chose C++ for its computational efficiency, and Python for its handy data analysis libraries. Every library in use is

¹⁷ J. A. Nelder and R. Mead. A Simplex Method for Function Minimization. *The Computer Journal*, Jan. 1965

free, they are the following :

- GNU scientific library for numerical optimisation.
- The Eigen 3 library for linear algebra.
- The pugiXML library for XML trees handling.
- The matplotlib library in Python for data plotting.
- The jsoncpp library for data serialisation.
- The for Python serialisation.
- The hyperdual library to handle hyperdual numbers.

2.4.1 XML input file, available functionalities

This section is more specifically devoted to future users of the code. We present the XML input file that contains the instructions for execution, we describe the custom syntax in use. Using such an input file enables to automate runs without building the whole C++ project again each time.

The input file takes form of an XML file since it enables to encode nested key/values pairs in a legible fashion. The syntactic highlightning that comes with many text editors further improves this legible aspect, which is convenient to fastly adapt simulations. Finally, the tree-like structure of an XML file enables every combinations of single independant instructions which makes the code very flexible to use, furthermore the parsing auto detects input errors and gives feedback to the user on typing errors.

Here is a non exhaustive list of allowed instructions :

- "CREATE" creates a network from a network input file, sets the boundary conditions, sets the number of subedges per strand and auto-adapts the stiffnesses accordingly, it can also deplete the network.
- "Stretching" selects the force extension relation, it sets the stretching constant in every edge of the system according to a normal distribution of prescribed average and width. It auto-adjusts constants them to the number of subedges so as a filament made of n strands converges towards the continuous limit we discussed in previous chapter.
- "Bending" sets the bending constant in every hinge of the system. It auto-adjusts them to the number of subedges in filaments.
- "Prestress" sets the forks preferred opening angle $\delta\theta_0$ in every edge of the system according to a normal distribution of prescribed average and width, it also sets the prestress intensity g .
- "ApplyStrain" applies a strain γ among several templates of usual deformations (axial compression, pure shear, simple shear, isotropic compression ...). It doesn't include relaxation for microscopic degrees of freedom.

- "ApplyStress" applies a stress σ among several templates of usual stresses (axial compression, pure shear, simple shear, isotropic compression ...), it includes relaxation for microscopic degrees of freedom and for strain, which are now degrees of freedom. Default values that work most of the time are taken to initialise minimizers.
- "CG" relaxes the microscopic positions of sites by means of a GSL conjugate gradient minimiser, under the constraint to satisfy boundary conditions.
- "NelderMead" minimises $\mathcal{U}^*(\gamma)$ by means of a Nelder-Mead algorithm with tunable parameters (sometimes avoids absurd results).
- "ComputeElasticTensor" computes full elastic tensors by means of hyperdual number algorithm.
- "WRITE" enables to write system's configuration with an adjustable level of details.
- "ResetPositions" enables to reset or randomize positions, and to reset strain.
- "ForLinear" allows to loop instructions over variable var , between values spanning from "begin" to "end", according to an arithmetic progression (addition of a constant step, if "log"=0) or to a geometric progressions (multiplication by a constant factor, if "log"=0).
- "ForEnum" allows to loop instructions over a list of values for variable var :

We show an example file for an input file in code below.

```

<!-- PROGRAM v7.0 - Tests -->
<INSTRUCTIONS>
  <CREATE>
    <Lattice      string = "HONEYCOMB2"
    ~ />
    <Shape        intX   = "10" intY="10" intZ="1"
    ~ />
    <PercolationP double = "1.0"
    ~ />
    <Lambda       double = "1.0"
    ~ />
    <SubEdges     int    = "10"
    ~ />
    <Boundaryconditions string = "PERIODIC"
    ~ />
    <CircularDomain enabled = "false">

```

```

    <Center          x="0" y="0"/>
    <Radius          double = "0.0" />
  </CircularDomain>
  <RectangularDomain enabled = "false">
    <Dimensions      x="0" y="0" />
  </RectangularDomain>
</CREATE>

<Stretching>
  <ForceExtensionRelation string = "Hooke" />
  <AvgStiffness          double = "1000." />
  <StdStiffness          double = "0.0" />
</Stretching>

<Bending double = "1.0" />

<Prestress>
  <PrestressG double = "100"/>
  <dTheta0Avg double = "0.52359877559"/>
  <dTheta0Std double = "0.0" />
</Prestress>

<ForLinear var = "gamma" begin = "0.2" end = "-0.6" N =
  - "100" log = "0">
  <ApplyStrain>
    <RotateStrain enabled = "false"
      double = "0.0"/>
    <gamma double = ""
      string = "PureDilation"/>
  </ApplyStrain>
  <CG>
    <ALGO string = "BFGS" />
    <Maxiter int = "100000" />
    <GradientTol double = "0.0" />
    <LineTol double = "0.001" />
    <InitialStep double = "0.01" />
  </CG>
  <Write>
    <Directory string = "../RESULTS/" />
    <SaveNetworkFile enabled = "true" />
    <RecordConfig enabled = "true" />
    <RecordForces enabled = "true" />
    <RecordForks enabled = "false" />

```

```

</Write>
<ResetPositions>
  <ResetNonAffinities   enabled = "false" />
  <ResetStrain           enabled = "false" />
  <RandomizeNonAffinities enabled = "true"
                        double  = "0.1" />
</ResetPositions>
</ForLinear>
</INSTRUCTIONS>

```

2.4.2 Code documentation

We documented C++ code by means of the Doxygen software and its tools for graphical visualisation. This software enables to create an html documentation of a project and to keep track of its structure. In particular it enables to plot class hierarchy graphs, and call graphs for functions such as in fig. 2.14. The whole documentation is available upon request, it is not available on-line because of its weight. A few comments must be done concerning the essential points that led to code efficiency :

- The project is object oriented, and every instruction available on the input file is a class that inherits from the metaclass Instruction. Keeping this logic allows to implement new fonctionnalities without breaking old ones.
- Simulations can be done in 2D or in 3D. However we didn't use dynamically allocated vectors in the Eigen library as they are slow to compute with. Instead, we built every class as a template taking space dimension as an input and make inner use of statically allocated vectors so as to keep efficiency at run time.
- Simulations can be made using either double or hyperdual data types, since each class is a template that takes data type T as a parameter.

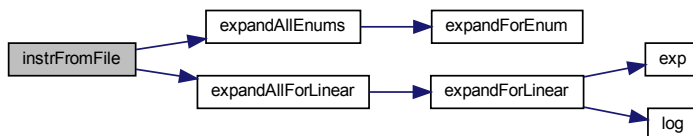


Figure 2.14: Call graph generated by Doxygen for the function that reads an XML file, expands loops, and allocate in memory the instantiations of "Instruction" classes.

3

Linear response in presence of residual stresses

In this chapter we investigate the effects of residual stress on the linear response of 3-coordinated fiber networks in 2D. Section 3.1 explains our choice of geometry. Section 3.2 presents the results of a linear computation for the shear modulus and bulk modulus around a configuration with zero boundary stress. Section 3.3 presents a theoretical model to help rationalize how elastic moduli get altered by residual stress. The section 3.4 discuss the limits of validity for this model. Finally 3.5 summarizes the important results .

3.1 *Choice of geometry*

In this section we present two factors which affect dramatically the mechanics of networks : their connectivity, and the residual stresses they store. We devote a subsection to each of these to motivate our choices of geometry and prestress.

3.1.1 *Connectivity of fiber networks*

The connectivity of fiber networks impacts dramatically their mechanical behaviour. Indeed, we can predict the existence of mechanisms in the network by comparing its number of degrees of freedom and its number of constraints, a mechanism, or zero-mode, is a mode of deformation which doesn't cost energy. This counting is known in literature as Maxwell's criterion^{1,2}. The average connectivity of the network is a control parameter for a rigidity phase transition which has been studied in ³ for lattice networks, in ⁴ for off-lattice networks.

Maxwell's is a criterion that only considers the overall topology of a network, by computing the number of its degrees of freedom and comparing it to its number of constraints. This mean-field argument can be contradicted by specifically designed structures, nonetheless it appeared robust to estimate phase transitions in random models. Namely, it was tested out on regular lattices depleted with a probability p or an on off-lattice networks with an average coordination z . In both cases, the criterion predicts very accurately the

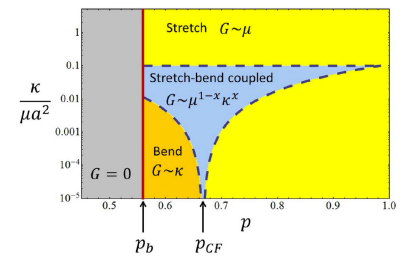


Figure 3.1: Phase diagram for the different regimes of a depleted triangular lattice. Survival probability of an edge during depletion is labeled p , and the dimensionless ratio of bending over stretching constants is $\frac{\kappa}{\mu a^2}$, shear modulus is labeled G . From Broedersz and MacKintosh, 2014.

¹ J. C. Maxwell. *The Scientific Papers of James Clerk Maxwell*. Cambridge University Press, Cambridge, 2011

² C. Calladine. Buckminster Fuller's "Tensegrity" structures and Clerk Maxwell's rules for the construction of stiff frames. *International Journal of Solids and Structures*, 1978

³ C. P. Broedersz, X. Mao, T. C. Lubensky, and F. C. MacKintosh. Criticality and isostaticity in fibre networks. *Nature Physics*, Oct 2011

⁴ E. M. Huisman and T. C. Lubensky. Internal Stresses, Normal Modes, and Nonaffinity in Three-Dimensional Biopolymer Networks. *Physical Review Letters*, Feb. 2011

critical point for the rigidity transition given by a system-specific simulation.

For the on-lattice case, the argument reads as follows : let's consider a random lattice in dimension d , with N sites, and N_b bonds, connected with a propability p . We count each edge of length ℓ as a constraint $\ell = \ell_0$, and each hinge as $(d - 1)$ angular constraints. The number of degrees of freedom is dN . The number of stretching constraints is pN_b as bonds are connected with probability p . The number of bending constraints is $(d - 1)N_b p^2$ as two bonds must be connected to form a hinge. A lattice is thus stabilized by stretching if $pN_b \geq dN$. It is stabilized by bending modes if $dN \leq pN_b + (d - 1)N_b p^2$ (which has only one positive root). This is in quantitative agreement with fig. 3.1 which shows that a phase transition is controlled by p , the order of this transition however might be system-dependant. This figure indeed shows more, because it also considers the ratio $\frac{\kappa}{\mu}$ of bending stiffness over stretching stiffness. It displays that, for unflexible networks, the network pass straight from a stretching dominated regime where shear modulus scales with stretching stiffness to a floppy regime. At the opposite limit, for flexible networks, where stretching constants dominate over bending ones, the networks get display three regimes, cascading from stretching dominated to bending dominated to floppy. In between, there is the existence of a mixed phase, and the transition is not sharp.

We don't give the argument for the off lattice case, since it is very similar.

This behaviour, according to which the elastic response of a network is dominated by its connectivity, display the universal phenomenology of phase transitions, such as critical exponents and scale invariance. For this reason it motivated a generic terminology in litterature. We call *hypostatic* a network below the critical point, *hyperstatic* a network above it, *isostatic* a network which is exactly at the critical point.

Examples Below we give a few examples of networks, we count their degrees of freedom, their number of constraints, and classify them according to the above terminology.

- **Hyperstatic** : A triangular lattice with $N = 2$ edges per bond has 8 degrees of freedom per cell, 6 stretching constraints, and 6 bending constraints. It is hyperstatic. We can't deform it without performing work as we can see in fig. 3.3.
- **Hypostatic** : The honeycomb lattice in 2D with two edges per bond. An unit cell of it has 5 sites and 6 edges. The number of degrees of freedom is thus 10 as we are in 2D, and the number of constraints is $6 + 3 = 9$. The network is thus hypostatic (we counted shearing constraints + bending ones), which translates into the activation of a zero mode when shearing it. It is worth noting that the number of edges per bond is in fact irrelevant, since adding one edges in a bond adds two degrees of freedom, but adds two constraints (on one length, and one angle). We show a shearing mode in 2D in fig 3.3.

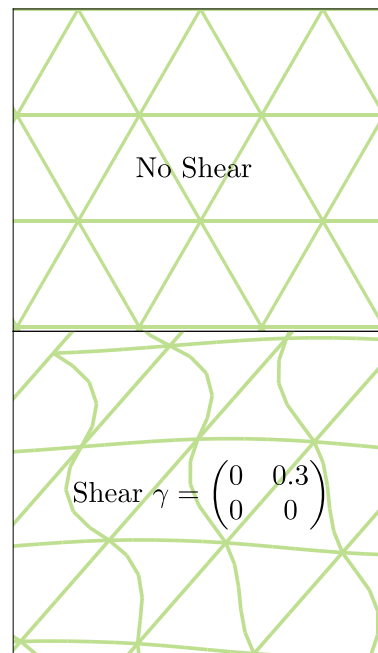


Figure 3.2: A triangular lattice in 2D is hyperstatic, as a result shearing costs energy.

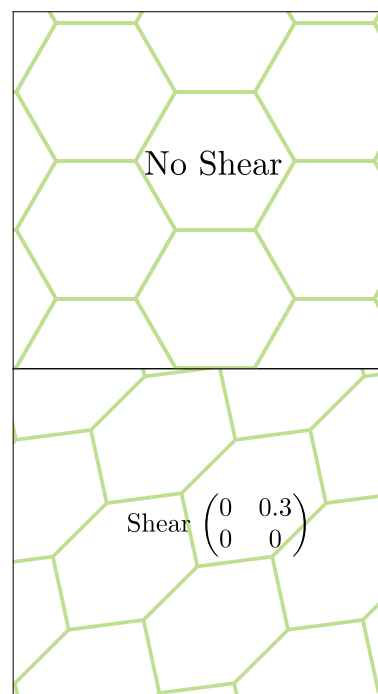
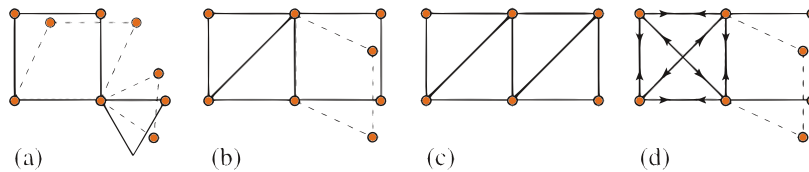


Figure 3.3: A honeycomb lattice in 2D is hypostatic, there is a shear soft mode which involve nor extension nor bending. We also represent an unit cell and its sites in black.

- **Isostatic** : the four frames in figure 3.4 satisfy exactly Maxwell's criterion (if we remove trivial translation and rotation zero modes). By changing the positions of its building blocks, we see that we can create mechanisms.

However, we can see in the figure 3.4 that Maxwell's criterion can fail at predicting the existence of stiff/soft modes. Indeed, by reconnecting bonds elsewhere, we can always create soft modes to the price of state of self stress⁴. This result is detailed in ⁵, the figure is extracted from this paper.



⁴ A state of state of self stress is a set of forces that an operator can apply and still preserve the equilibrium of the system.

Figure 3.4: Several structures that show that counting constraints sometimes fails at predicting network's stiffness. From Lubensky et al. 2015. Indeed, (a) has two soft modes, (b) one soft mode and one state of self stress, (c) has two self-stress states, (d) has one soft mode and one self-stress state

Furthermore, it is worth noting that Maxwell's criterion applies well for networks at rest. Nonetheless there exist several ways to stiffen an hypostatic network by disturbing its equilibrium :

- **Global prestress** This phenomenon where a structure has its stiffness increased under stress is general. A famous example is at the very principle of many musical instruments : if we put a rope under tension, it ends up with a finite transverse stiffness, proportional to the tension. The same holds for a 2D structure such as a skin put under stress by a adjustable metallic circle in a drum set... In our context, if we put the honeycomb lattice under tension by applying an isotropic strain to it, the shearing soft-mode will end up with a finite stiffness.
- **Tensegrity** Alternatively tensegrity structures, can provide a network made of a mixture of soft elements and stiff elements with a finite stiffness⁶. It comes into play for systems made of non linear elements with complementary non linearities like ropes which are soft under compression and stiff under extension, and metallic rods which are stiff under compression and can break under extension.
- **Residual stresses** Bundled actin displays many residual stresses at a local scale because of unsatisfied constraints in a self-assembled network. This question has been addressed recently⁷ numerically, having hydrogel metamaterials in mind. It remains however an open question. This is what we study in this thesis.

We choose to work with a honeycomb network in 2 dimensions which has a connectivity of 3, and the model of forks we made in chapter 1 requires 3 coordinated nodes. Furthermore, it is hypostatic from the viewpoint of bending and stretching, which makes it a good candidate to be stiffened by residual stress.

⁵ T. C. Lubensky, C. L. Kane, X. Mao, A. Souslov, and K. Sun. Phonons and elasticity in critically coordinated lattices. *Reports on Progress in Physics*, July 2015

⁶ D. Stamenović and D. E. Ingber. Tensegrity-guided self assembly: from molecules to living cells. *Soft Matter*, 2009

⁷ A. Bose, M. F. J. Vermeulen, C. Storm, and W. G. Ellenbroek. Self-stresses control stiffness and stability in overconstrained disordered networks. *Physical Review E*, Feb. 2019

We search how it is affected by the presence of forks which generate residual stresses. The question of distributing these forks over the network was already addressed on section 1.4. We concluded that four representants encompassed all the invariance group of a honeycomb network in figure 1.10 : we will make measurements systematically over the representants (α), (β), (γ) and (δ) of these classes.

3.2 Linear Results

In this section we characterise linear elastic response of the unit cells, only considering bulk modulus and shear modulus in a first time, considering the three non zero eigen values of the stiffness tensor in a second time.

3.2.1 Parameters in use

The parameters in use have been the same as those determined in Chapter 1, i.e. filaments subdivided into $N = 4$ parts, a bending stiffness $\kappa = 1$, a stretching stiffness $\mu = 1000$, a strong clamp on each fork with $g = 500$. We varied however the opening angle of forks at rest, $\delta\theta_0$, between its acceptable physical limits (i.e. without overlapping filaments) $-\frac{2\pi}{3}$ and $\frac{\pi}{3}$ which correspond to the physical situations represented in fig. 3.5 where forks are respectively fully open and fully closed.

For each of the values of $\delta\theta_0$, we equilibrated the network to a zero boundary stress state, then we measured its elastic moduli. We did this for the geometries (α), (β), (γ) and (δ). We first comment on their isotropy, we then make a systematic measurement of shear modulus and bulk modulus.

3.2.2 Unit cells response

The experiment we made was to first set $\delta\theta_0$ to a given value between the physical bounds $-\frac{2\pi}{3}$ and $\frac{\pi}{3}$. We selected the bounds $-\frac{2\pi}{3}$ and $\frac{\pi}{3}$ for $\delta\theta_0$ which correspond to the forks being fully open and fully closed. To realize these plots, we started from $\delta\theta_0 = 0$ and slowly increased (resp. decreased) its value, we then gathered the results into a single plot for positive and negative values.

Bulk Modulus. Here we display the bulk modulus K of the rest configuration as a function of $\delta\theta_0$: in fig. 3.6.

From these graphics, we see that the material becomes softer under isotropic compression when $|\delta\theta_0|$ increases (at least in the vicinity of 0). We can get a qualitative understanding of it if we realize the following : the bulk modulus $K = -A_0 \frac{\partial P}{\partial A}$. However for $\delta\theta_0 = 0$ the area would be maximal for inextensible filaments, since the geometry is hexagonal. Thus for a small pressure increment δP , the relative variation in area would be of order δP^2 , making K diverge. In practice K gets regularised at the scale of $\mu = 1000$ and

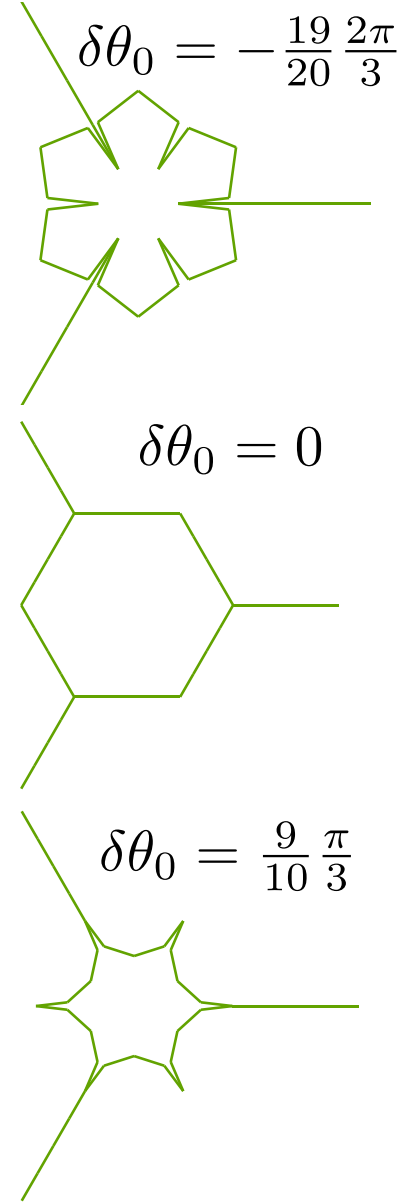


Figure 3.5: The physical limits for forks are reached for $\delta\theta_0 = -\frac{2\pi}{3}$ (fully open fork) and $\delta\theta_0 = \frac{\pi}{3}$ (fully closed fork) in the case of the geometry (α).

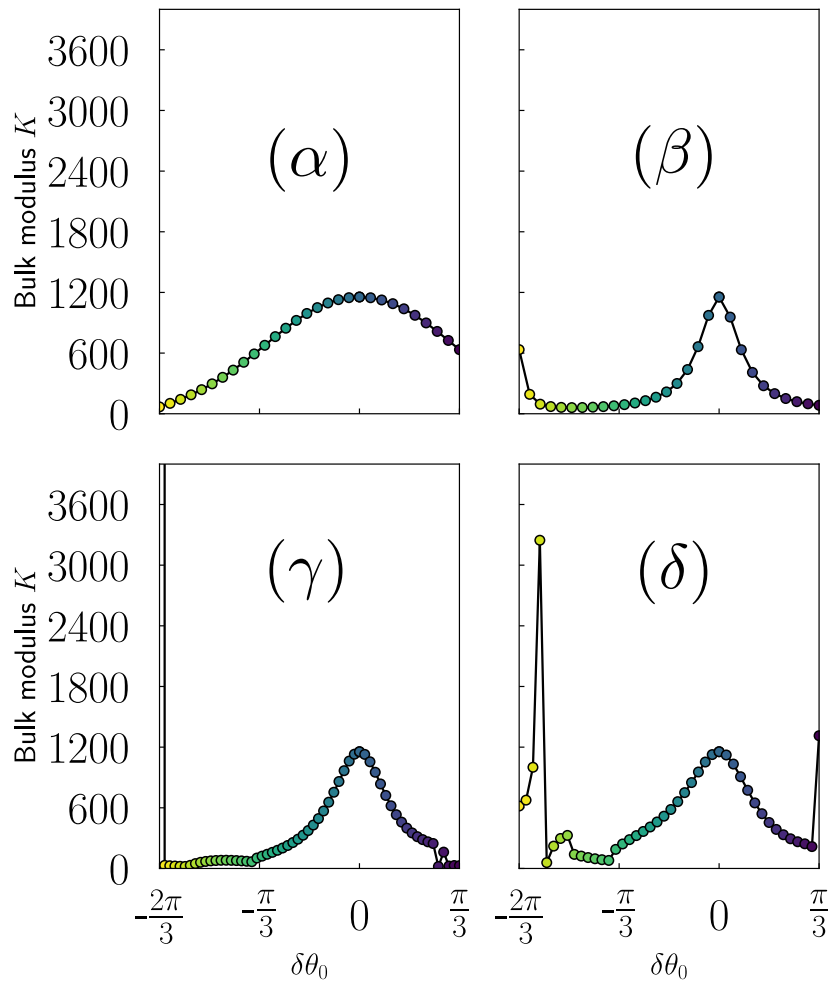


Figure 3.6: Bulk modulus as a function of $\delta\theta_0$. $\delta\theta_0 = 0$ means that the target geometry is honeycomb. In this case the orientation of forks no longer plays a role, so the four moduli are the same at this value. As soon as $\delta\theta_0 \neq 0$ the four geometries differentiate, however in each case the prestress into forks induces a softening of the material. The color of dots is redundant with the value of $\delta\theta_0$, however it will help in comparing figures in chapter 4.

probes extensibility of filaments. This is why the stiffness is of this order of magnitude.

Shear Modulus. We now present the results for the shear modulus G measured as a function of $\delta\theta_0$ depending on the geometry in figure 3.7.

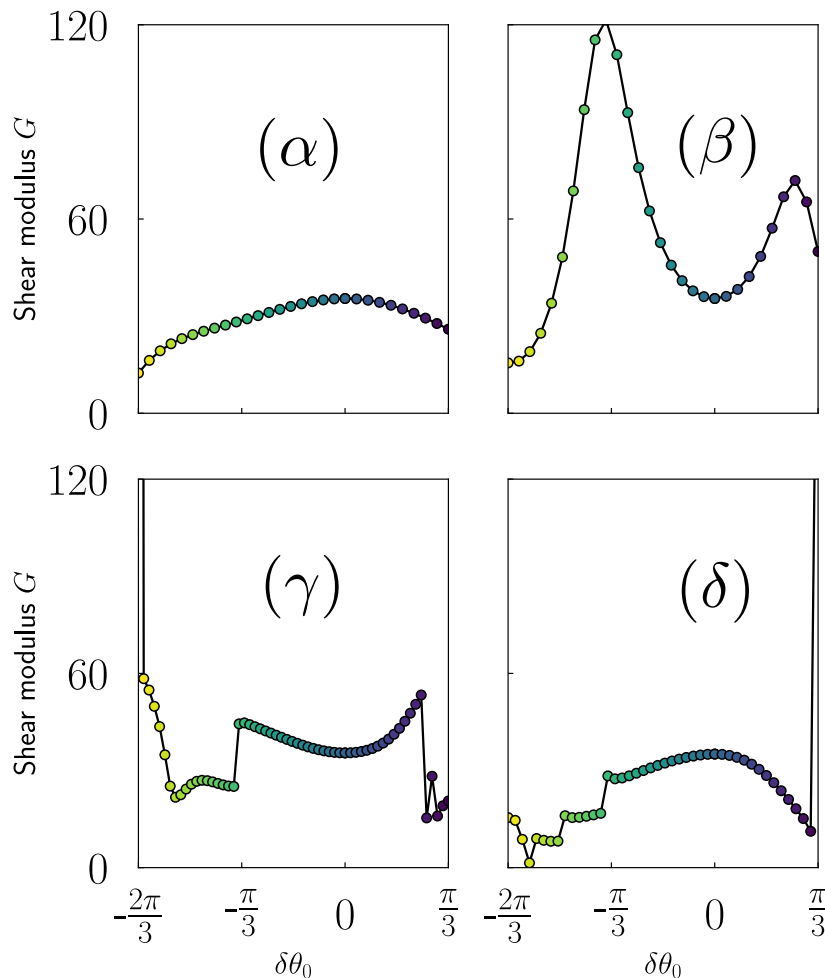


Figure 3.7: Shear modulus as a function of $\delta\theta_0$. $\delta\theta_0 = 0$ means that the target geometry is honeycomb. In this case the orientation of forks no longer plays a role, so the four moduli are the same at this value. No universal trend can be drawn : the prestress can induce either a softening or a stiffening of the material.

On these plots, the conclusion concerning the material stiffening is not as universal as for bulk modulus. Indeed the shear modulus doesn't always have a monotonous trend. Furthermore the trend for small $\delta\theta_0$ depends on the geometry we are considering.

On these two sets of curves, we realise that discontinuous events occur for the highest values of $|\delta\theta_0|$. Up to now we did not pay attention to it, but if we think about the Nelder-Mead algorithm to relax boundary stress, we notice that we are not guaranteed to find the closest one in strain space. As a consequence, the sudden jumps in elastic moduli suggest the existence of several zero boundary stress states. This could be the signature of instabilities leading to the collapse of the cell, which may be favoured by the topology of

surrounding forks. These instabilities can be studied through the non linear strain of the system, which is the object of chapter 4. For now however, we will leave them appart and close our eyes on the highest values of $\delta\theta_0$ for the linear curves to come.

3.2.3 Assembly response

When we dealt with spatially extended systems, we did not see deformation patterns exceeding the scale of one unit cell. In other terms, the cristalline symmetry isn't broken by the presence of prestress. The prestress doesn't couple unit cells between each other unless it lies on non regular patterns, which we didn't study enough to comment on a quantitative basis.

3.3 A model to explain linear stiffening in presence of residual stresses.

The previous section showed that residual stresses could lead to either stiffening or softening of a material. However it has been made on a specific kind of systems and doesn't tell about generic networks. For this reason this section presents the formalism drawn by in ref ⁸. This formalism defines states of infinitesimal self-stress states and zero modes/mechanisms. We then extend this formalism to the case where forces are not central. Indeed, because of the forks, filaments can be subject to torques, which induce a different kind of self-stress states. We believe that the existence of such states under tension is able to change the stiffness of the materials. For this reason, our generalisation is necessary.

3.3.1 Self-Stress states and mechanisms, in absence of torque

Let's consider networks of fibers with N sites and N_b bonds around an equilibrium reference position. If we displace sites by an amount $\mathbf{U} \in \mathbb{R}^{dN}$, bonds have an extension $\mathbf{E} \in \mathbb{R}^{N_b}$, sites feel a force $\mathbf{F} \in \mathbb{R}^{dN}$ and bonds a signed tension $\mathbf{T} \in \mathbb{R}^{N_b}$. We can fully obtain tensions \mathbf{T} from forces \mathbf{F} . Likewise, we can fully obtain the extensions \mathbf{E} from the displacements \mathbf{U} . We have the linear relation :

$$\begin{cases} Q\mathbf{T} = \mathbf{F} \\ C\mathbf{U} = \mathbf{E} \end{cases} \quad (3.1)$$

Where Q is a $dN \times N_b$ matrix and C a $N_b \times dN$ one.

We define *self-stress states* as a set of tensions that all compensate so that the system doesn't feel a force, namely $\mathbf{F} = 0$ but $\mathbf{T} \neq 0$. We define *zero-modes* as displacements that doesn't involve extension of bonds, i.e. $\mathbf{E} = 0$ but $\mathbf{U} \neq 0$. In this infinitesimal formalism they are thus vectors of the kernel of Q and C .

⁸ T. C. Lubensky, C. L. Kane, X. Mao, A. Souslov, and K. Sun. Phonons and elasticity in critically coordinated lattices. *Reports on Progress in Physics*, July 2015



Figure 3.8: Tensegrity structure with cables under extension and rods under compression. A Snelson-Fuller sculpture in the graduate college courtyard at Princeton.

A self-stress state requires a coexistence of tensions and extension. They are at the basis of tensegrity structure, which are stiff structures in which soft elements in extension compensate for compression of stiff elements as in fig. 3.8.

We can apply this formalism to a very simple example : a metallic rod lying on the x axis, almost inextensible with a stiffness μ_1 and a rest length ℓ_1 , in parallel with a soft spring with a stiffness μ_2 and a rest length $\ell_2 \leq \ell_1$. The set of extensions here contains the extension of the first spring and of the second spring, which are different because the reference of each spring is different :

$$\begin{aligned} \mathbf{E} &= \begin{pmatrix} x_2 - x_1 - \ell_1 \\ x_2 - x_1 - \ell_2 \end{pmatrix} \\ &= \begin{pmatrix} -1 & 0 & 1 & 0 \\ -1 & 0 & 1 & 0 \end{pmatrix} \begin{pmatrix} u_1 \\ v_1 \\ u_2 \\ v_2 \end{pmatrix} - \begin{pmatrix} \delta \ell_1 \\ \delta \ell_2 \end{pmatrix} \end{aligned}$$

Where $\delta \ell_i$ represents the extension of the spring i in the rest configuration. For the network to be at rest, it should verify the equilibrium condition $\mu_1 \delta \ell_1 + \mu_2 \delta \ell_2 = 0$.

Likewise, the tensions lead to the forces :

$$\mathbf{F} = \begin{pmatrix} f_{1x} \\ f_{1y} \\ f_{2x} \\ f_{2y} \end{pmatrix} = \begin{pmatrix} 1 & 1 \\ 0 & 0 \\ -1 & -1 \\ 0 & 0 \end{pmatrix} \begin{pmatrix} t_1 \\ t_2 \end{pmatrix} = \begin{pmatrix} t_1 + t_2 \\ 0 \\ -t_1 - t_2 \\ 0 \end{pmatrix}$$

We find here that we have a state of self stress $\mathbf{T} = \begin{pmatrix} 1 \\ -1 \end{pmatrix}$ for which one spring is in compression and the other is in extension. We have only three trivial zero modes $(1 \ 0 \ 1 \ 0)$, $(0 \ 1 \ 0 \ 1)$ and $(1 \ 0 \ -1 \ 0)$ which correspond to global translations and infinitesimal rotation.

It is worth noting the difference with the formalism presented in the aforementioned reference on states of self stress. Indeed we didn't assume the springs to be individually at rest in the reference configuration: we allowed springs to store a pretension, provided this respects force balance : the pretension must thus be a linear combination of states of self-stress.

3.3.2 Geometrical non linearities impact elastic moduli

In this part, we want to show that a system in which non linear elements store residual stress in a self stress state can be stiffer (or softer) than the same system with linear elements storing the same residual stresses. It is a generalisation of the mechanism according to which a string stiffens transversely when it is prestressed. However here, prestress is not applied by an

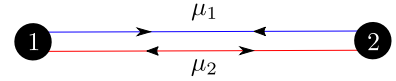


Figure 3.9: Springs state of self stress, the x axis is along the symmetry axis. A blue bond is extended, whereas a red bond is compressed

external operator, but results from tensions in the elementary constituents of the system.

Let's consider a system with residual stress, in a rest configuration with residual tensions in its constituents which are compatible with a state of self stress T_0 (or a linear combination of states of self stress). We exert a strain γ on the system, so that its sites respond in moving of an infinitesimal \mathbf{U} :

$$d\mathcal{U} = \frac{1}{2} \mathbf{U} \mathbf{K} \mathbf{U}$$

where \mathbf{K} is the elastic matrix of local stiffnesses of the system. We add to it the non linear displacement-extension relation of the system, called geometrical non linearity (for instance $l = \sqrt{x^2 + y^2}$ for a system of one bond linked to the origin).

$$E_i = C_{i\alpha} U_\alpha + \frac{1}{2} C_{i\alpha\beta}^2 U_\alpha U_\beta,$$

where C and C^2 are the coefficients of this expansion.

On the other side we can write $d\mathcal{U}$ from the extensions, with the help of the bonds diagonal stiffness matrix \tilde{K} :

$$\begin{aligned} d\mathcal{U} &= \frac{1}{2} \mathbf{E} \tilde{\mathbf{K}} \mathbf{E} \\ &= \frac{1}{2} \left(C_{i\alpha} U_\alpha + \frac{1}{2} C_{i\alpha\beta}^2 U_\alpha U_\beta \right) \tilde{K}_{ij} \left(C_{j\sigma} U_\sigma + \frac{1}{2} C_{j\sigma\rho}^2 U_\sigma U_\rho \right) \\ &= \frac{1}{2} U_\alpha C_{i\alpha} \tilde{K}_{ij} C_{i\sigma} U_\sigma + U_\alpha C_{i\alpha} \frac{1}{2} C_{j\sigma\rho}^2 U_\sigma U_\rho \\ &= \frac{1}{2} \mathbf{U} \mathbf{K}_{effective} \mathbf{U} \end{aligned}$$

Thus, provided we know the U 's as a function of γ (which, in fact, would require to solve the minimisation problem...), we could deduce the stiffness tensor as a function of the local stiffnesses matrix, which is affected by the degree of pretension stored in the springs through the non linearity in C^2 . This remains true even if the relations between generalised tensions and generalised extensions are linear.

3.3.3 Generalisation of the notion of self-stress state to systems with residual torques

The formalism presented up to now doesn't translate directly to the networks we study. Indeed constraints arise from the fact that edges prefer to remain at rest, but there are simultaneously angular degrees of freedom trying to minimise bending and to satisfy the angular constraints of forks. We thus need to develop a generalized formalism to account of the equilibrium between tensed forks and extended filaments. In this section we proceed to this generalisation, then we give an example of a model system, which only exhibits one angular interaction and a stretching interaction.

If we consider a network made of N sites, N_b bonds and N_a stiff angles (hinges or forks), we can generalize equation 3.1 to :

$$\begin{cases} \begin{pmatrix} \mathbf{Q}_b & \mathbf{g}_{ab} \\ \mathbf{g}_{ba} & \mathbf{Q}_a \end{pmatrix} \begin{pmatrix} \mathbf{T} \\ \Gamma \end{pmatrix} = \mathbf{F} \\ \begin{pmatrix} \mathbf{C}_b \\ \mathbf{C}_a \end{pmatrix} \mathbf{U} = \begin{pmatrix} \mathbf{E} \\ \eta \end{pmatrix} \end{cases} \quad (3.2)$$

Where we defined the vector of torques Γ and the vector of angular extensions η . Q_b generalises the matrix Q we previously had and \mathbf{C}_b the matrix C . The quantities with an index "a" generalise these notions to angles, finally the matrices g 's correspond to the coupling terms. It is worth noting that these block matrices are not square matrices !

We can re-define states of self stress as a set of tensions and torques that leave the system at rest, and a soft-mode a set of displacements that does not extend filaments nor opens angles.

A variation in energy for an infinitesimal displacement which result in a force field \mathbf{F} is then given by :

$$\begin{aligned} \delta \mathcal{U} &= \frac{1}{2} \mathbf{F}^T \mathbf{U} \\ &= \frac{1}{2} \begin{pmatrix} \mathbf{T}^T & \Gamma^T \end{pmatrix} \begin{pmatrix} Q_b & g_{ba} \\ g_{ab} & Q_a \end{pmatrix} \mathbf{U} \end{aligned}$$

In other words the constraints in the system induce a coupling between two sectors of G that is proportional to the pre-tensions into forks.

We can apply this formalism to compute generalised states of self stress of a system made of three rods with an angular forcing on one angle at the top. We label nodes by an arabic number, and bonds by a roman number, according to figure 3.10.

We have the purely geometric relation :

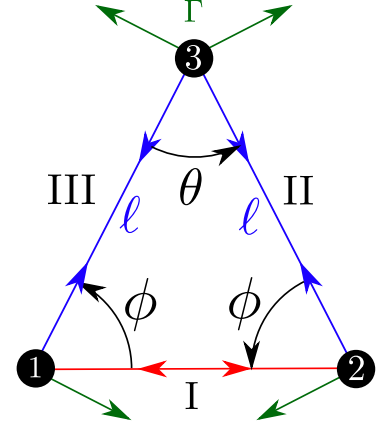


Figure 3.10: Generalized state of self-stress with torque forcing. Sites are labeled from 1 to 3, edges from I to III, there is a fork over site 3. We can take, among others, the potential energy :

$$\mathcal{U} = \sum_{i=I}^{III} \frac{1}{2} (\ell_i - 1)^2 + \frac{1}{2} g (\theta - \theta^0)^2$$

$$\begin{aligned}
 \mathbf{F} = \begin{pmatrix} f_{1x} \\ f_{1y} \\ f_{2x} \\ f_{2y} \\ f_{3x} \\ f_{3y} \end{pmatrix} &= \begin{pmatrix} -1 & 0 & -\cos(\phi) & \frac{\cos(\frac{\theta}{2})}{\ell} \\ 0 & 0 & -\sin(\phi) & -\frac{\sin(\frac{\theta}{2})}{\ell} \\ 0 & 1 & \cos(\phi) & -\frac{\cos(\frac{\theta}{2})}{\ell} \\ 0 & 0 & -\sin(\phi) & -\frac{\sin(\frac{\theta}{2})}{\ell} \\ 0 & \sin(\frac{\theta}{2}) & \sin(\frac{\theta}{2}) & 0 \\ 0 & \cos(\frac{\theta}{2}) & \cos(\frac{\theta}{2}) & 2\frac{\sin(\frac{\theta}{2})}{\ell} \end{pmatrix} \begin{pmatrix} t_I \\ t_{II} \\ t_{III} \\ \Gamma \end{pmatrix} \\
 &= \begin{pmatrix} -1 & 0 & -\sin(\frac{\theta}{2}) & \frac{\cos(\frac{\theta}{2})}{\ell} \\ 0 & 0 & -\cos(\frac{\theta}{2}) & -\frac{\sin(\frac{\theta}{2})}{\ell} \\ 0 & 1 & \sin(\frac{\theta}{2}) & -\frac{\cos(\frac{\theta}{2})}{\ell} \\ 0 & 0 & -\cos(\frac{\theta}{2}) & -\frac{\sin(\frac{\theta}{2})}{\ell} \\ 0 & \sin(\frac{\theta}{2}) & \sin(\frac{\theta}{2}) & 0 \\ 0 & \cos(\frac{\theta}{2}) & \cos(\frac{\theta}{2}) & 2\frac{\sin(\frac{\theta}{2})}{\ell} \end{pmatrix} \begin{pmatrix} t_I \\ t_{II} \\ t_{III} \\ \Gamma \end{pmatrix}
 \end{aligned}$$

Where we used $\theta + 2\phi = \pi$. This shows the existence of a state of self stress that verifies

$$\begin{cases} t_I = -\lambda \left(\tan\left(\frac{\theta}{2}\right) \sin\left(\frac{\theta}{2}\right) + \frac{1}{\ell} \cos\left(\frac{\theta}{2}\right) \right) \\ t_{III} = \lambda \tan\left(\frac{\theta}{2}\right) \\ \Gamma = \lambda \end{cases} \quad (3.3)$$

where λ is a scalar parameter. This states of self-stress couples extension of filaments and opening of forks.

The example above suggests that a wide variety of generalized self-stress states can be reached when we add up bending stiffness of filaments, where bending could get coupled to forks for instance.

3.4 Limits of validity of the simulations

In this section we comment on the limits of validity of our numerical experiments. We subdivide this discussion in two parts. The first part deals about the lack of isotropy of the cells of interest, the second deals about excluded volume which is not taken into account although it should for high values of $\delta\theta_0$.

3.4.1 Isotropy of the cells

As the four geometries studied don't belong to the same symmetries classes, we shall study how many independant elastic coefficients they have to test weither or not measuring two elastic components is enough to fully characterise their elastic response.

By "independant elastic coefficient" we mean an eigen value which labels for a (sometimes degenerate) eigen space in the elastic tensor. Let's illustrate the concept with a 3D linear isotropic material. For such a material, the elastic tensor provides the linear relationship between stress and strain, it reads as follows in the Voigt basis (introduced chapter 1):

$$\sigma_I = K_{IJ}\gamma_J \quad (3.4)$$

$$\begin{pmatrix} \sigma_I \\ \sigma_{II} \\ \sigma_{III} \\ \sigma_{IV} \\ \sigma_V \\ \sigma_{VI} \end{pmatrix} = \begin{pmatrix} K + \frac{4}{3}G & K - \frac{2}{3}G & K - \frac{2}{3}G & 0 & 0 & 0 \\ K - \frac{2}{3}G & K + \frac{4}{3}G & K - \frac{2}{3}G & 0 & 0 & 0 \\ K - \frac{2}{3}G & K - \frac{2}{3}G & K + \frac{4}{3}G & 0 & 0 & 0 \\ 0 & 0 & 0 & 2G & 0 & 0 \\ 0 & 0 & 0 & 0 & 2G & 0 \\ 0 & 0 & 0 & 0 & 0 & 2G \end{pmatrix} \begin{pmatrix} \epsilon_I \\ \epsilon_{II} \\ \epsilon_{III} \\ \epsilon_{IV} \\ \epsilon_V \\ \epsilon_{VI} \end{pmatrix} \quad (3.5)$$

where we noted the bulk modulus K and the shear modulus G . We can diagonalise it to find the eigen strains, i.e. strains which give rise a stress by a scalar factor. We get the following eigen values/eigen vector pairs :

$$(2G, \begin{pmatrix} 0 \\ 0 \\ 0 \\ 0 \\ 0 \\ 1 \end{pmatrix}), (2G, \begin{pmatrix} 0 \\ 0 \\ 0 \\ 1 \\ 0 \\ 0 \end{pmatrix}), (2G, \begin{pmatrix} 0 \\ 0 \\ 0 \\ 1 \\ 0 \\ 0 \end{pmatrix}), (2G, \begin{pmatrix} -1 \\ 0 \\ 1 \\ 0 \\ 0 \\ 0 \end{pmatrix}), (2G, \begin{pmatrix} -1 \\ 1 \\ 0 \\ 0 \\ 0 \\ 0 \end{pmatrix}), (3K, \begin{pmatrix} 1 \\ 1 \\ 1 \\ 0 \\ 0 \\ 0 \end{pmatrix})$$

Which means that there exist only two independant elastic coefficients in a 3D isotropic system (the number of independant eigen spaces). The bulk modulus K , which gives the lattice's stiffness for an isotropic deformation. The shear modulus G which gives the stiffness for a simple shear motion in either xy , yz or xz directions. It also provides the response for a isovolumic compression in these directions, indeed these are nothing but a simple shear rotated of $\frac{\pi}{4}$ in their plane.

In this terminology, we see that having two independant elastic moduli is not enough to be isotropic, as the eigen-strains may be different from those of an isotropic cell.⁹

For an isotropic material in 2D, we have :

$$\sigma_I = K_{IJ}\gamma_J \quad (3.6)$$

$$\begin{pmatrix} \sigma_I \\ \sigma_{II} \\ \sigma_{III} \\ \sigma_{IV} \end{pmatrix} = \begin{pmatrix} K+G & K-G & 0 & 0 \\ K-G & K+G & 0 & 0 \\ 0 & 0 & G & 0 \\ 0 & 0 & 0 & 0 \end{pmatrix} \begin{pmatrix} \epsilon_I \\ \epsilon_{II} \\ \epsilon_{III} \\ \epsilon_{IV} \end{pmatrix} \quad (3.7)$$

This still leads to three independant elastic moduli, one for the bulk response, one for the shear response, and one for the isochore compression of an axis with dilation of the orthogonal axis.

⁹ TODO : Find examples of materials to emphasize physical meaning. Comment on Landau's "complex coordinate" argument which says that an O(3) symmetry provides only two independant moduli, but doesn't say anything about eigen-strains. In 2D we would prefer to use an eigen value / angles parametrization of the problem.

The isotropic case will serve as a benchmark to measure the degree of anisotropy of our systems.

In practice, we must stress out :

- The fact that we only make our study on shear modulus and bulk modulus,
- The fact that we don't always check that a shear deformation and a bulk deformation are eigen strains of the system,

even though we know our systems are anisotropic. We will check how much on the next subsection, in order to keep in mind afterwards, whenever we won't recheck it. In the end we will prioritise the convenient physical interpretation of the shear and bulk deformations we apply over their fitness to the material. Furthermore, we need a comparison point between cells, and shear, bulk moduli are better suited for this purpose.

3.4.2 Fixed $\delta\theta_0$, fixed g : how isotropic are these cells.

In this subsection, we compute the full elastic tensor for the geometries of interest at $\delta\theta_0 = 0.35$. We diagonalise it to conclude on the number of independant moduli the system has. The results are gathered in the table 3.11, rounded to 10^{-3} for the sake of legibility :

Geometry	Elastic tensor (Voigt basis)	Eigen values	Eigen vectors
(α)	$\begin{pmatrix} 289.333 & 255.072 & 0 & 0 \\ 255.072 & 289.333 & 0 & 0 \\ 0 & 0 & 34.261 & 0 \\ 0 & 0 & 0 & 0 \end{pmatrix}$	$\begin{pmatrix} 544.405 \\ 34.261 \\ 34.261 \\ 0. \end{pmatrix}$	$\begin{pmatrix} 1 \\ 1 \\ 0 \\ 0 \end{pmatrix}, \begin{pmatrix} 1 \\ -1 \\ 0 \\ 0 \end{pmatrix}, \begin{pmatrix} 0 \\ 0 \\ 1 \\ 0 \end{pmatrix}, \begin{pmatrix} 0 \\ 0 \\ 0 \\ 1 \end{pmatrix}$
(β)	$\begin{pmatrix} 123.357 & 81.132 & 0 & 0 \\ 81.132 & 123.36 & 0 & 0 \\ 0 & 0 & 42.226 & 0 \\ 0 & 0 & 0 & 0 \end{pmatrix}$	$\begin{pmatrix} 204.491 \\ 42.227 \\ 42.227 \\ 0 \end{pmatrix}$	$\begin{pmatrix} 1 \\ 1 \\ 0 \\ 0 \end{pmatrix}, \begin{pmatrix} 1 \\ -1 \\ 0 \\ 0 \end{pmatrix}, \begin{pmatrix} 0 \\ 0 \\ 1 \\ 0 \end{pmatrix}, \begin{pmatrix} 0 \\ 0 \\ 0 \\ 1 \end{pmatrix}$
(γ)	$\begin{pmatrix} 253.530 & 220.106 & -2.483 & 0 \\ 220.106 & 257.861 & -2.823 & 0 \\ -2.483 & -2.823 & 35.867 & 0 \\ 0 & 0 & 0 & 0 \end{pmatrix}$	$\begin{pmatrix} 475.844 \\ 35.963 \\ 35.451 \\ 0. \end{pmatrix}$	$\begin{pmatrix} -0.704 \\ -0.710 \\ 9.10^{-3} \\ 0 \end{pmatrix}, \begin{pmatrix} 0.361 \\ -0.346 \\ 0.866 \\ 0 \end{pmatrix}, \begin{pmatrix} 0.612 \\ -0.612 \\ -0.5 \\ 0 \end{pmatrix}, \begin{pmatrix} 0 \\ 0 \\ 0 \\ 1 \end{pmatrix}$
(δ)	$\begin{pmatrix} 236.675 & 209.275 & 0 & 0 \\ 209.275 & 252.393 & 0 & 0 \\ 0 & 0 & 34.079 & 0 \\ 0 & 0 & 0 & 0 \end{pmatrix}$	$\begin{pmatrix} 453.957 \\ 35.112 \\ 34.079 \\ 0 \end{pmatrix}$	$\begin{pmatrix} 0.694 \\ 0.720 \\ 0 \\ 0 \end{pmatrix}, \begin{pmatrix} 0.720 \\ -0.694 \\ 0 \\ 0 \end{pmatrix}, \begin{pmatrix} 0 \\ 0 \\ 1 \\ 0 \end{pmatrix}, \begin{pmatrix} 0 \\ 0 \\ 0 \\ 1 \end{pmatrix}$

Figure 3.11: Diagonalisation of elastic tensors of the four unit cells.

A few comments can be done on the light of the symmetries of the selected cells.

- The (α) geometry behaves as an isotropic continuous medium, it doesn't couple shear to compression, it has only two independant elastic moduli,

and the corresponding eigen-strains are the well known isotropic compression, axial traceless compression and simple shear. This is consistent with it having an order 6 symmetry under rotations and being achiral.

- The (β) geometry behaves identically, as it is isotropic however it is chiral, which could in principle allow coupling between compression and shear.
- The (γ) geometry displays a small degeneracy lift between x compression and y compression, consistent with its anisotropy, and a coupling between shear and compression, consistent with its chirality. It starts to lift the degeneracy in the eigenspace associated to shear, which we will confirm later by increasing $\delta\theta_0$.
- The (δ) geometry displays a small degeneracy lift between x compression and y compression, consistent with its anisotropy, and no coupling between shear and compression, consistent with its achirality.

In order to obtain more legible results, we can represent these elastic

tensors on the Voigt basis : $\left\{ \begin{pmatrix} 1 \\ 1 \\ 0 \\ 0 \end{pmatrix}, \begin{pmatrix} 1 \\ -1 \\ 0 \\ 0 \end{pmatrix}, \begin{pmatrix} 0 \\ 0 \\ 1 \\ 0 \end{pmatrix}, \begin{pmatrix} 0 \\ 0 \\ 0 \\ 1 \end{pmatrix} \right\}$:

Geometry	Elastic tensor (New basis)
(α)	$\begin{pmatrix} 544.405 & 0 & 0 & 0 \\ 0 & 34.261 & 0 & 0 \\ 0 & 0 & 34.261 & 0 \\ 0 & 0 & 0 & 0 \end{pmatrix}$
(β)	$\begin{pmatrix} 204.49 & 0.002 & 0 & 0 \\ -0.002 & 42.227 & 0 & 0 \\ 0 & 0 & 42.227 & 0 \\ 0 & 0 & 0 & 0 \end{pmatrix}$
(γ)	$\begin{pmatrix} 475.801 & -2.165 & -3.752 & 0 \\ -2.165 & 35.590 & 0.240 & 0 \\ -3.752 & 0.240 & 35.867 & 0 \\ 0 & 0 & 0 & 0 \end{pmatrix}$
(δ)	$\begin{pmatrix} 453.809 & -7.859 & 0 & 0 \\ -7.859 & 35.259 & 0 & 0 \\ 0 & 0 & 34.079 & 0 \\ 0 & 0 & 0 & 0 \end{pmatrix}$

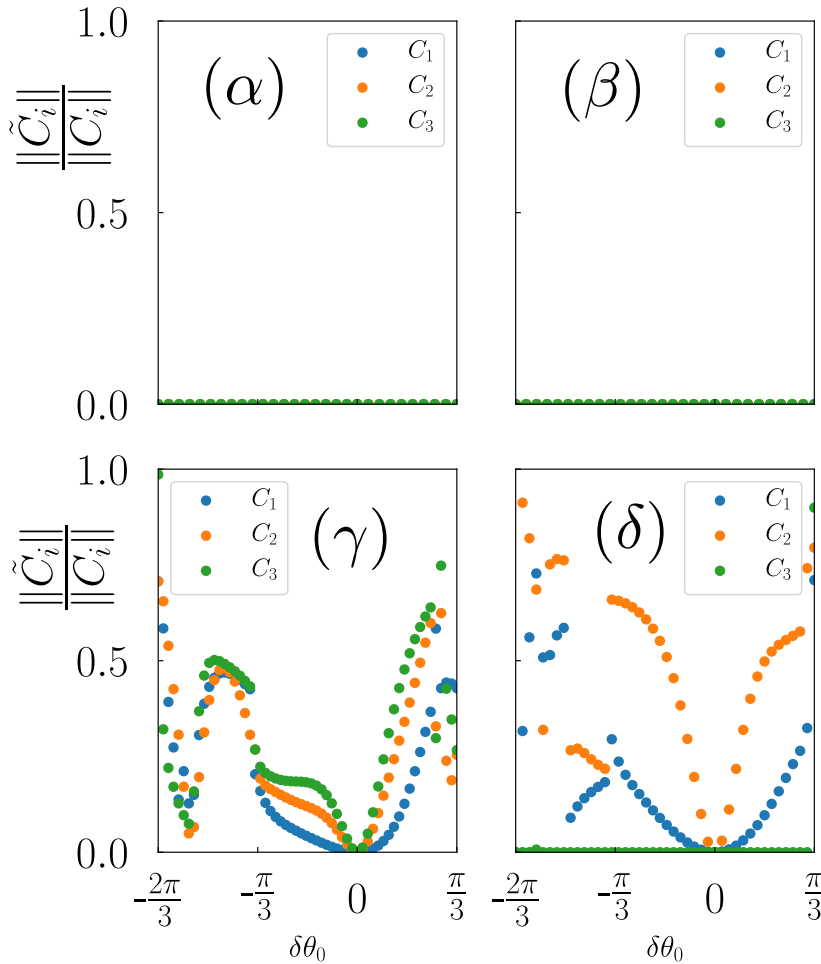
This makes appear a clear separation of scales between shear response and bulk response, as compression modes can involve stretching of filaments, while shear privilege bending.

3.4.3 How isotropic are the unit cells ?

In order to state on how anisotropically the network behaves as a function of residual stress, we compute the elastic constants in the Voigt basis as the ratio $\frac{\|\tilde{C}_i\|}{\|C_i\|}$ where C_i denotes the column i of the elastic tensor in the eigen-basis for isotropic materials, and \tilde{C}_i is the same vector minus its i 'th component. If the matrix is diagonal it vanishes, otherwise it measures the proportion of non diagonal components with respect to the diagonal components.

This characterisation is one among others, we could have been using a graphical method to estimate how anisotropic the elastic tensors were like the diagrams of poles proposed in ¹⁰.

We measured anisotropy for the physical bounds $\delta\theta_0 = -\frac{2\pi}{3}$ to $\delta\theta_0 = \frac{\pi}{3}$. We plot the anisotropy as a function of $\delta\theta_0$ in figure 3.12.



¹⁰ M. François. Identification des symétries matérielles de matériaux anisotropes

Figure 3.12: Evolution of the anisotropy as $\delta\theta_0$ increases. We see that the more we increase $|\delta\theta_0|$, the more networks behave anisotropically. However we will only plot bulk modulus K and shear modulus G for any geometries because it provides a easy to test experimental comparison.

These results show that the (α) and (β) cells behave as isotropic cells no matter what $\delta\theta_0$ we choose, and that the cells (γ) and (δ) behave more and

more anisotropically $\delta\theta_0$ grows as suggested by figure 3.13. In this figure, the unit cells progressively goes from honeycomb ($\delta\theta_0 = 0$) to an uniaxial geometry where red filaments are under compression and blue filaments are under extension. A first discontinuity arises when these filaments buckle for $\delta\theta_0 = 60^\circ$. A second one appear because a bistability between two configurations, which is allowed by a self-intersection of the network.

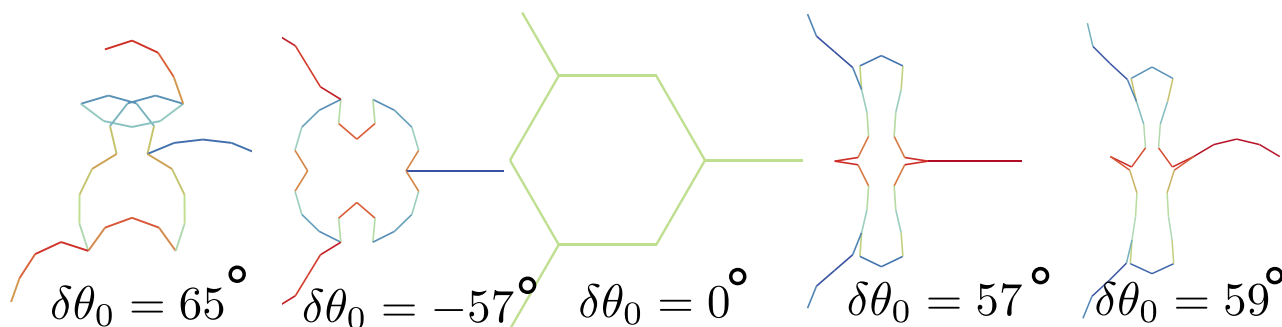


Figure 3.13: How the (δ) geometry evolve as $\delta\theta_0$ increases from $-\frac{2\pi}{3}$ to $\frac{\pi}{3}$. They are ordered from left to right according to increasing by growing $\delta\theta_0$. Red filaments are compressed, while blue ones are extended. We display a new figure before and after discontinuities each time.

3.4.4 Excluded volume, collapse of some geometries

As we mentioned at the beginning of the chapter, we did not study the collapses occurring at high $|\delta\theta_0|$, we merely tried to avoid them by increasing $\delta\theta_0$ as slowly as possible. We call collapse an event in which the area of the network comes close to 0. Given our definition of the area of the network, as the area spanned by the vectors joining two periodic copies of a site, collapses correspond most often to self intersecting lattices.

These collapses are made possible because our model doesn't take into account excluded volume interactions of filaments : this limits the range of validity of simulations to a narrower band of $\delta\theta_0$ than the initially proposed $-\frac{2\pi}{3}$ to $\frac{\pi}{3}$. Nonetheless it doesn't invalidate the region where the networks doesn't self intersect since excluded volume wouldn't come into play. Indeed it is a short ranged interaction, which doesn't affect system's mechanics when filaments are separated by more than its characteristic range. We show an example of a collapse in figure 3.14, we will study them more deeply in the chapter 4, about non linear elastic response.

3.5 Summary

In this chapter, we discussed our choice of an hypostatic geometry and the orientations of forks. We explained why Maxwell's criterion couldn't help to determine the rigidity of stressed networks. We measured two independant elastic components on these networks and saw that residual stresses could affect the elasticity of the material in both directions. We proposed a model to explain this effect on the light of the pretension stored in non linear elements

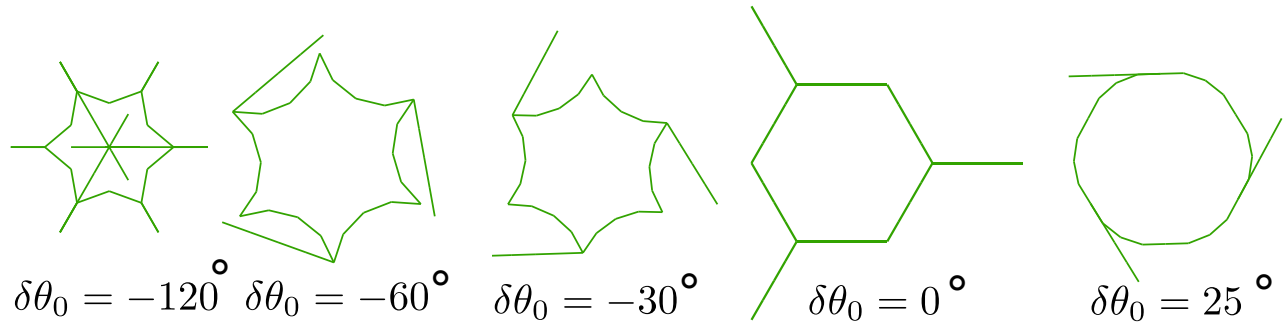


Figure 3.14: Example of a collapse as $\delta\theta_0$ decreases, on geometry β , lowest values are at left. This collapse wouldn't be allowed by excluded volume interactions.

at a microscopic level. An other possible mechanism being geometrical stiffening due to non linearities of the generalized extensions. In the end we discussed the limitations of our measurements : first our geometries can be strongly anisotropic, then the geometries can collapse for strong angular mismatches, in addition we didn't observe large scale deformation patterns when repeating the units cells over a broad network.

This taught us that residual stresses can induce the linear response of a network to be stiffer or softer when we shear it, and be softer when we compress it. The case of random lattices has not be addressed but is on its way to draw a more universal conclusion concerning these effects. Our analytic model proposed a generalisation of the notion of states of self-stress that could involve tensions exerted by forks. We proposed that the elastic tensor of networks would get increased/decreased by the amount of tension stored into these. Nonetheless, these analytic models become untractable as we go beyond model cases and could be applied to larger networks.

4

Response to finite boundary strains

In this chapter we study the non linear response of the networks in the presence of residual stresses. This study complements the linear study made on chapter 2, indeed in this chapter we used an algorithm to find zero boundary stress, without paying attention to how we reached this zero boundary stress, this chapter fills this gap. In section 4.1 we present the stress and the elastic moduli of networks as they are sheared and compressed of finite amounts. In section 4.2 we present a model for the collapse of the (α) unit cell under isotropic compression and discuss how this collapse should be regularised by excluded volume interaction. Beyond this particular case we do this in order to show generally how the local geometries of forks can enhance local collapses while compressing fiber networks. Section 4.3 draws a conclusion on the teachings of this non linear study.

4.1 Response to non linear compression and shear

When studying the linear response of the networks with residual stress, we encountered several cases where the networks collapsed when trying to relax boundary stress. To study more quantitatively the physics in this range of parameters, we decided to study the response of the network by fixing the boundary strain. In subsection 4.1.1 we show the evolution of shear stress and shear modulus when applying finite shear strains at the boundaries, we find scaling laws between them. Subsection 4.1.2 shows the evolution of boundary pressure and bulk modulus when applying a finite shear strain, we conclude that it induces collapses. Finally subsection 4.1.3 concludes on the points that cannot be reached by simulations.

4.1.1 Residual stress tunes the predominance of bending over stretching under shear

The experiment we have simulated was to start from the reference configuration with zero boundary stress. This configuration corresponded to a strain γ_0 , leading to a deformation $\mathbb{1} + \gamma_0$ from the honeycomb configuration.

From this configuration we applied a strain γ on boundaries, leading to a deformation tensor from the honeycomb configuration $(\mathbb{1} + \gamma)(\mathbb{1} + \gamma_0)$. In this experiment γ_0 is a function of $\delta\theta_0$ of the system. Our control parameter is then γ , the strain relative to the zero boundary stress configuration.

The curves of shear stress against strain are displayed in figure 4.1.

The first striking phenomenon we see on these curves is their similarity : no matter the orientation of forks we chose, it doesn't affect dramatically the shear response of the networks. For this reason we will comment on the set of curves for the geometry (α), and the comments will hold for all geometries.

Let's comment the set of curves (α). At fixed $\delta\theta_0 = 0$ (the blue curve), we mainly see two regimes : one with a small slope at small strains, and one with a larger slope at larger strains. The small slope regime corresponds to the fact that the network response starts by curving bending modes to accomodate strain, which is energetically favourable. The large slope regime arises as filaments bending doesn't project over boundary shear anymore. From this point the network accomodates larger strains by allowing filament extensions and angular torsions on forks, which translates into an increase in shear modulus (the slope of the curves), since the stretching constants of edges and the stiffnesses of forks are both of order 10^3 , while the bending constant is of order 1.

As we increase or decrease $\delta\theta_0$ ($\delta\theta$ increases when the curves turn more purple, it decreases when they turn more yellow), the soft regime shrinks to leave room to the stiff regime. This can be qualitatively understood by the fact that there bending only can accomodate a finite amount of strain which has to be shared between satisfying shear strain and satisfying at fork angles. As $|\delta\theta_0|$ increases, this amount gets partially exhausted by pre-bending into filaments, which reduces the margin for the soft regime in the strain response. As a result, there exists a cross-over which corresponds to the transition between these regimes, characterised by a crossover strain that decreases as $|\delta\theta_0|$ increases.

To give a second reading of these two regimes, we provide a curve of shear modulus versus strain in figure 4.2. These curves display more clearly the stiffening effect of residual at low strain, since we only have to read the evolution of the shear modulus at the origin. Noenetheless we don't see a clear criterion on strain to identify the transition between soft and stiff regime. These curves also show that forks start to open when we shear the system too much, which we can see with the presence of a maximum in the shear modulus. In other terms, we are not anymore in the limit of strong angular clamping that we discussed chapter 1. In practice for the actin bundles we have in mind, this regime of strains would be so drastic that it would be able to unzip the frustrated bundles, which we don't take into account in the model, contrarily to ref.¹. For this reason we did not shear the system by more than 200%.

Finally, we plot the absolute value of shear modulus versus absolute value

¹ M. Caruel, J.-M. Allain, and L. Truskinovsky. Mechanics of collective unfolding. *Journal of the Mechanics and Physics of Solids*, 76, Mar. 2015

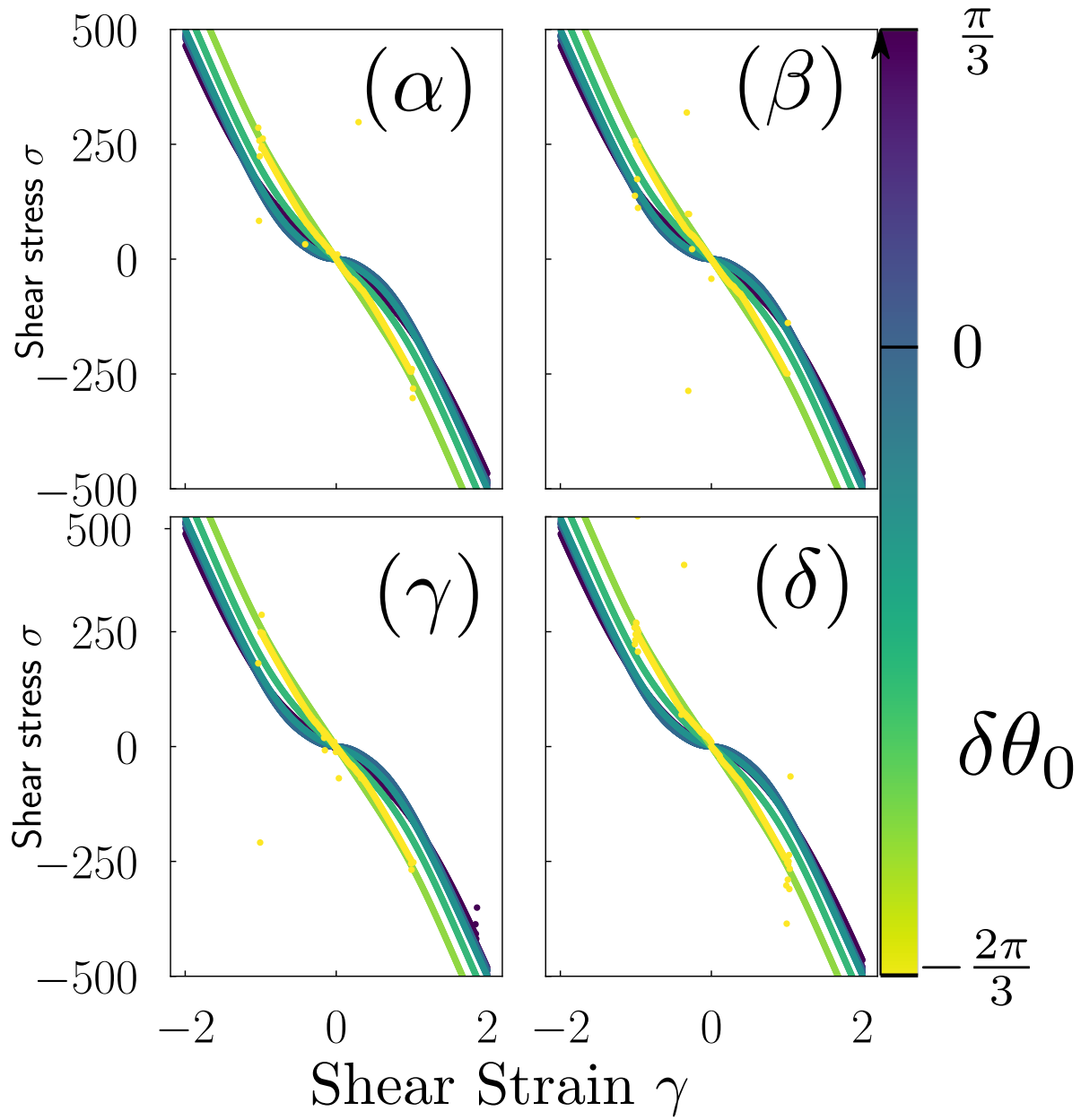


Figure 4.1: Curves of shear stress versus shear strain during a non linear shearing operation. The curves color scale correspond to the value of $\delta\theta_0$, yellow for $-2\pi/3$, purple for $\pi/3$, blue for 0, it is the same as for the linear figures.

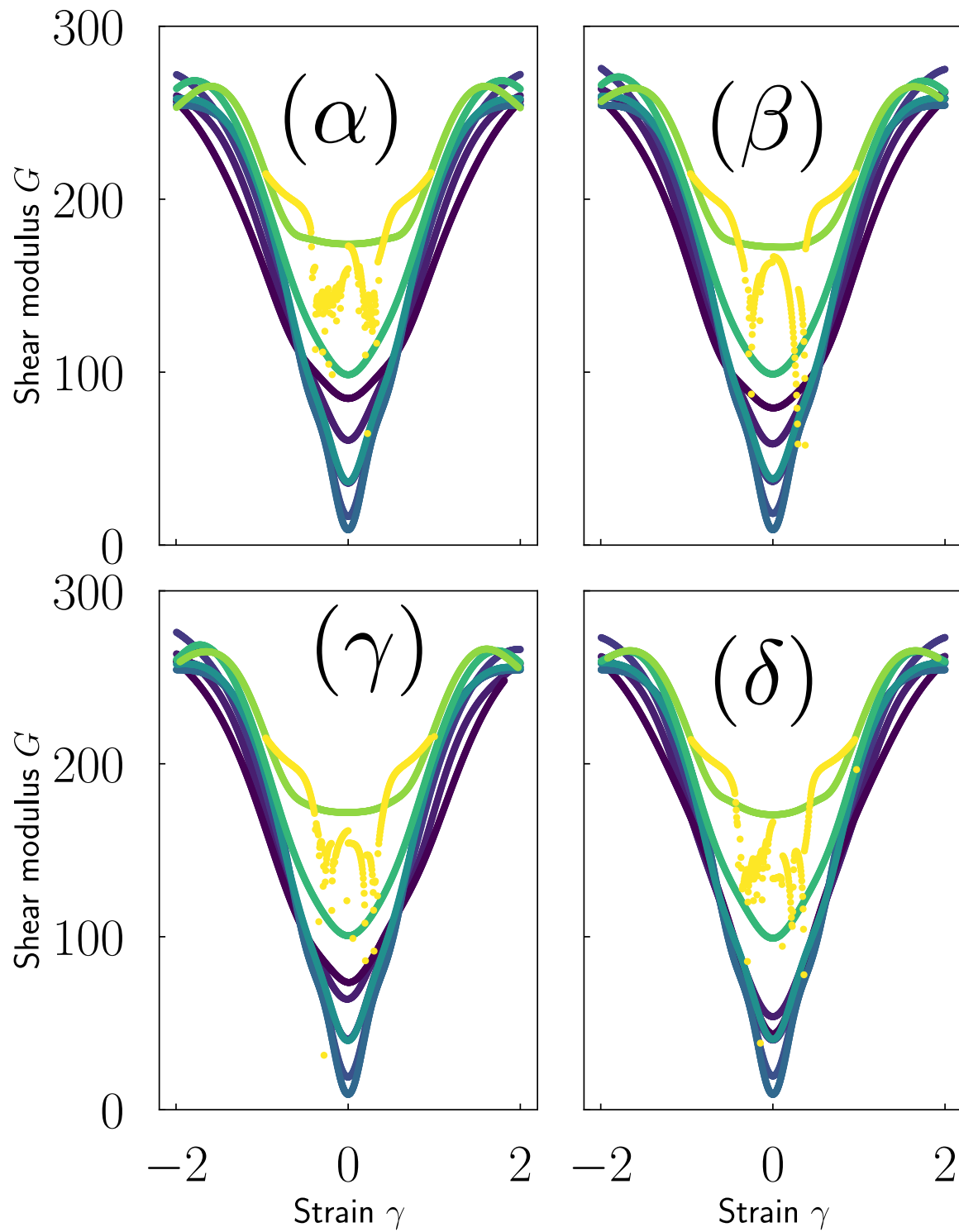


Figure 4.2: Differential shear modulus versus non linear shear strain for the four reference geometries. We see more clearly the stiffening effect of residual stress at small strains. However, critical strain becomes more difficult to read in this graphs.

of shear stress, in log-log scale, in figure 4.3. We see very clearly the existence of two elastic regimes, controlled by a critical stress. A linear regime where shear modulus is constant at low stress, and a stiffening regime where elastic modulus scales proportional to shear stress after a critical stress which is function of $\delta\theta_0$. This critical stress increases as $|\delta\theta_0|$ increases, contrarily to the critical strain. These two regimes are similar to what was observed experimentally in collagen networks², it differs however from what is observed in actin networks in reference, where the authors measure a stiffening exponent of $3/2$ ³.

Finally, we display figure 4.4 the results for a random network made of 8x8 random cells with random orientation of their forks, which confirms previous observations that the two regimes doesn't depend on fork's orientations. We didn't reproduce the experiment over larger networks nor more realisation of a network of this size. Indeed, it didn't seem there was much variability from one realisation to an other. However we didn't compute standard deviation to affirm it quantitatively.

² A. J. Licup, S. Münster, A. Sharma, M. Sheinman, L. M. Jawerth, B. Fabry, D. A. Weitz, and F. C. MacKintosh. Stress controls the mechanics of collagen networks. *Proceedings of the National Academy of Sciences*, 112, Aug. 2015

³ M. L. Gardel. Elastic Behavior of Cross-Linked and Bundled Actin Networks. *Science*, 304, May 2004; and M. Jaspers, M. Dennison, M. F. J. Mabesoone, F. C. MacKintosh, A. E. Rowan, and P. H. J. Kouwer. Ultra-responsive soft matter from strain-stiffening hydrogels. *Nature Communications*, Dec. 2014

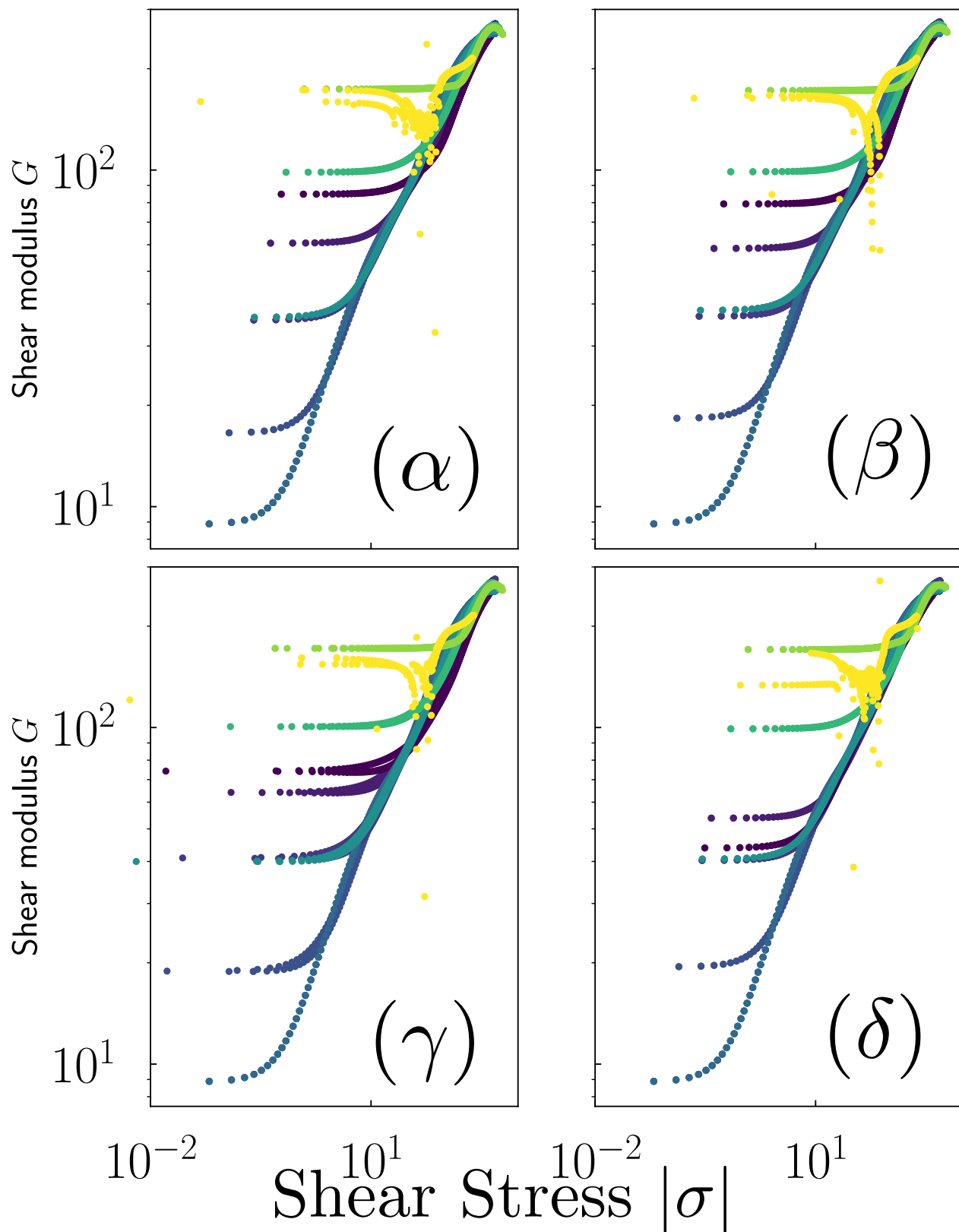


Figure 4.3: Curves of absolute value of shear modulus versus absolute value of shear stress, in log-log scale. The color code remains the same as in the previous graphs. These curves highlight the transitions between a linear regime and a stiffening regime with scaling exponent 1.

4.1.2 Residual stress enables instabilities under compression

We also tested the response under isotropic compression of the network, this might not be relevant to networks living in aqueous solution, as their response is dominated by the incompressibility of the solvent. However it is within reach of our simulations, and help answer our research question to understand the effect of residual stress on fiber networks.

This time we didn't look for the zero stress state before doing simulations. Indeed, we discovered that depending on the residual stress, there existed several zero stress states some of them being collapsed networks, which are unphysical because of their self intersections. These collapsed states appear when compressing the system as discontinuities in elastic quantities. Even when proceeding with very small increments of strain we cannot get rid of them. They are the manifestation of an instabilities that we can study partially numerically, as long as we can get continuous compression curves. We can partially study them analytically on specific geometries, and this time we don't have problems in obtaining continuous compression curves, furthermore excluded volume can be studied analytically as a regularising mechanism preventing self-intersecting structures.

In figure 4.5 we plotted the pressure against strain. The strain was shifted so that the zero pressure state corresponds to zero strain on post treatment of the simulations. Indeed we did not take the risk to relax boundary stress using the Nelder-Mead algorithm, which could have resulted in a collapsed reference state. Instead we applied strains from the honeycomb configuration, then we shifted strains to the zero boundary stress of larger area, and rescaled it so that strains corresponded to a relative variation in area with respect to the zero pressure state and not the honeycomb reference geometry. To obtain smooth curves, we used a small strain increment $\delta\gamma = \frac{1}{400}$ so as to always follow the same continuous curve. Indeed, it happens that two equilibria configurations correspond to a same strain, for instance when a filament buckles or a cell flips inside out. However, with an increment $\delta\gamma$ too large, we would take the risk to apply a stress too suddenly at the pre-minimisation stage of affine compression of the network, this would result in a discontinuous event This is not always successful as some discontinuous events keep on occurring, however it is a good compromise between computation time and provided information. Furthermore, imposing a noise before minimisation may accelerate convergence in simulations, but here we avoid it. Indeed this could also introduce local stresses that would induce discontinuous events !

In particular, using these small compression steps together with the total absence of noise before minimisation induces that the $\delta\theta_0 = 0$ blue curve always follows affine compression, as nothing breaks the axial symmetry of

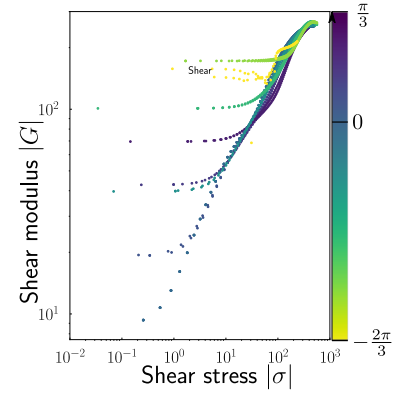
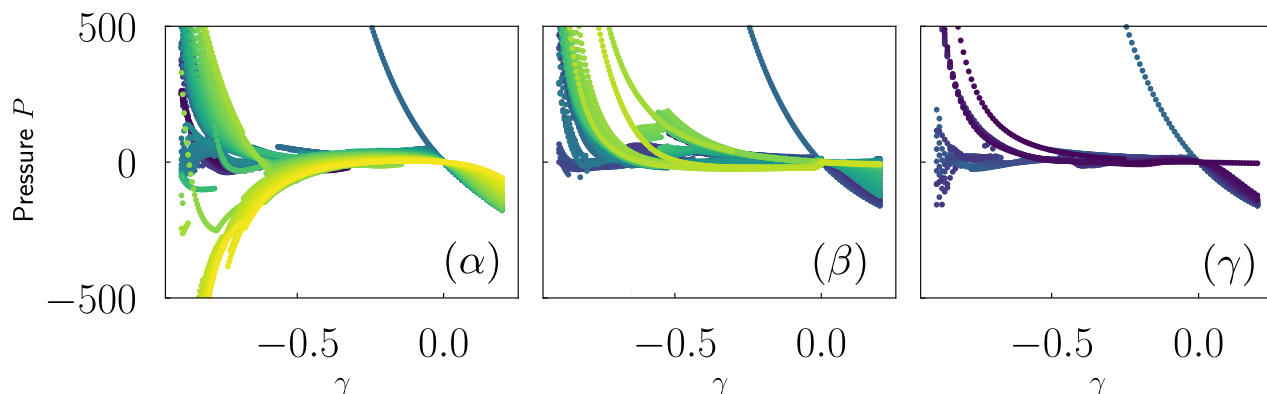


Figure 4.4: Absolute value of shear modulus versus absolute value of shear stress, in log-log scale, on a random 8x8 lattice. These curves confirm that the effect of residual stress on shear elasticity doesn't depend much on the geometry of forks.

We call collapsed networks with a area close to zero. Given our definition of area : the area spanned by the vectors between two periodic copies of a site, they are most often networks that self-intersect

filaments. However, as soon as $\delta\theta_0 \neq 0$, this symmetry is broken by the forks, and the transition from stretching to buckling becomes smooth.

We see that depending on the value of $\delta\theta_0$, an instability may emerge. More specifically, if the slope $\frac{\partial P}{\partial \gamma}$ is negative the network is stable, if it is positive it is unstable. Sometimes an inflection leads to the existence of several zero pressure states. The instability will be studied into further details in 4.2.3.



We can see that the geometry matters very much in the stabilising or destabilising effect of residual stress :

- The (α) geometry only has one zero pressure state at low $|\delta\theta_0|$, but already has an unstable region for compressive strains. As we increase $|\delta\theta_0|$, we end up with three intersections with the x axis. For the most negative values of $\delta\theta_0$, we loose the stable area for the biggest compressions. However, these compressions are such that we should care about excluded volume, which would stabilise the network after a collapse to a geometry of small area, without self-intersections. In practice, we don't trust too to the smallest strains in these curves because they involve self-intersections.
- For the (β) geometry, residual stress has a stabilising effect as the unstable part of the curve can disappear for some negative values of $\delta\theta_0$. We observe instabilities for positive values of $\delta\theta_0$.
- For the (γ) geometry, residual stress has a destabilising effect when $\delta\theta_0$ becomes more positive. When it becomes negative, we observe discontinuous events that make the numerical study unable to study instabilities. Indeed many states close to zero pressure seem to coexist, and we oscillate between them as we compress the system. The study of the instability in this case is beyond the perimeter of our simulations.
- We did not run simulations for the (δ) geometry under compression.

Figure 4.5: We display here the pressure versus compressive strain. The strain is measured with respect to the reference honeycomb configuration but was shifted and rescaled on post-treatment for the zero pressure states to correspond. Color code for $\delta\theta_0$ is the same as usual, in particular the blue curve corresponds to $\delta\theta_0 = 0$. We didn't have time to run simulations on the geometry (δ) .

The strong dependance on geometry prompts us to study broader random networks, in which the random orientations of the forks would induce local collapses, that would be smoothed in the elastic response of the large network. We may ask how the mechanical stability of the whole network will be impacted.

We plot the pressure-strain curve for a random 8x8 network (figure 4.6). Here we used a noise before minimisation to help our conjugate gradient procedure to converge, and we took fewer data points. As a results we observe several discontinuous events under compression, they get more and more likely as $|\delta\theta_0|$ increases, and they correspond to local collapses of cells due to instabilities similar to the ones that we studied with unit cells. These instabilities are favoured by the local geometries of forks around a collapse just before it occurs. For now however, these results are preliminary, and we only present them qualitatively to the reader. Indeed, we should increase system's size so that the local collapses get smoothed out, we think that it would result in a plateau in the elastic response, as we will describe in the next section. The next section proposes a model to this foam-like behaviour, in the restricted case of a network made of the cell (α) alone.

4.1.3 Conclusion

4.2 A model for non linear behavior on the alpha unit cell

In this section we propose an analytic model to explain the behaviour a specific geometry under compression: the cell (α). First we make a pressure-area curve to show the emergence of an instability, then we make a phase diagram in which we summarise the stability regions as a function of the forks opening angle $\delta\theta_0$. Nonetheless, we emphasize that this results only holds for one kind of geometry, and might well be different on an other one. The phase diagram presented is thus an example of the richness of phenomena that can occur because of residual stresses, it deserves to be completed.

4.2.1 Pressure-Area curve shows instability

In order to reduce the problem to a one-dimensional system, we need to make some assumptions. First we will consider forks as infinitely stiff : the angles at which anchorings occur will be set equal to $\delta\theta_0$. Second we will consider each bond to be subdivided in four subedges, each of them being infinitely stiff and their length set equal to $\frac{1}{4}$. Finally we assume the system to preserve its symmetry of order 6 as it deforms. In the end we end up with a system with one degree of freedom, the angle ϕ in the middle of a filament, as we can see on figure 4.7.

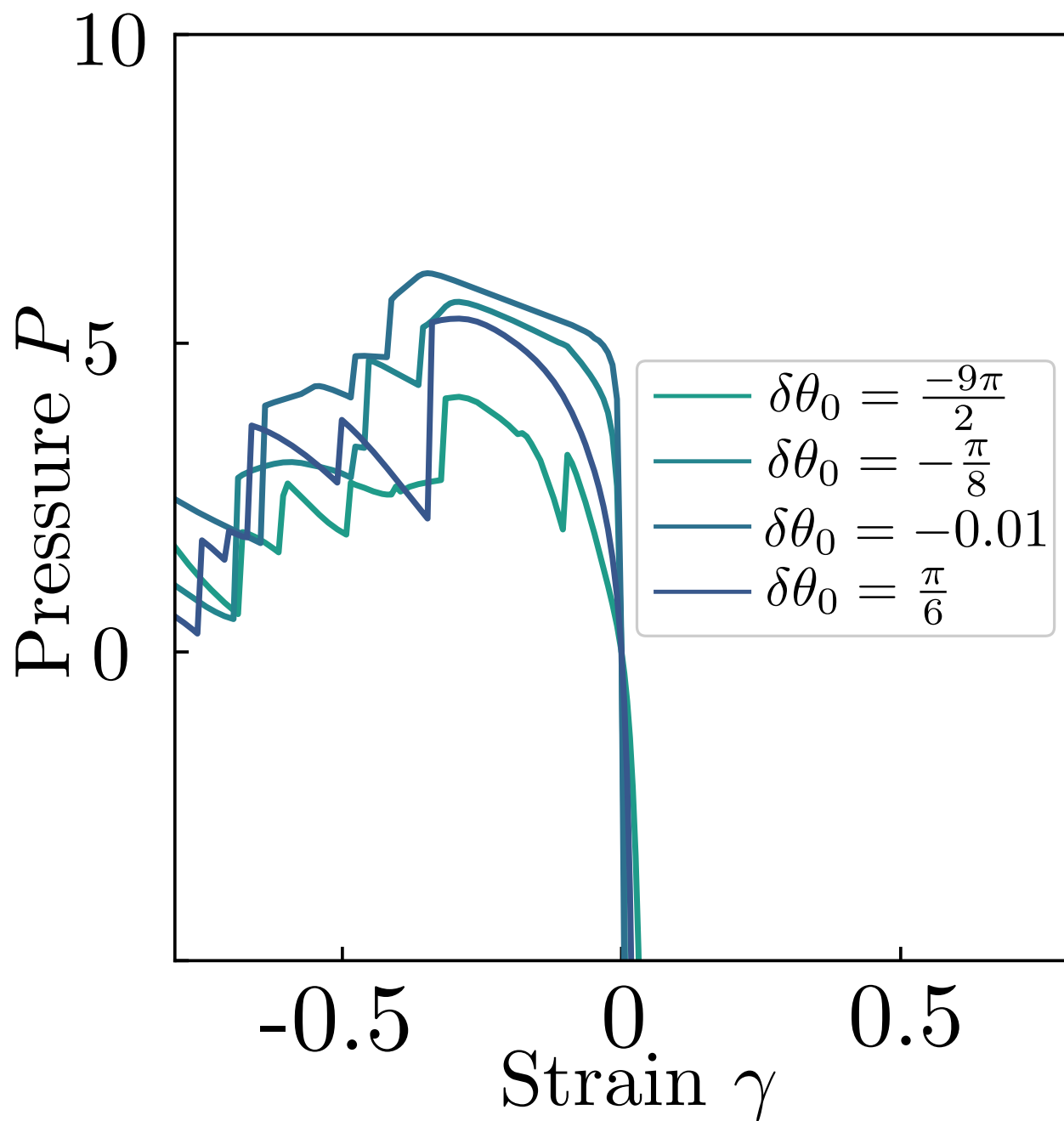


Figure 4.6: Pressure-modulus curve for a network under compression, we see a sequence of local collapses as compressive strain increases.

By doing so we can write the potential energy of the system as a function of the control parameter $\delta\theta_0$ and the degree of freedom ϕ .

$$\mathcal{U}(\delta\theta_0, \phi) = 4(3 - 2 \cos(\phi - \delta\theta_0) - \cos(2\phi))$$

On the other hand the pressure then reads :

$$P = - \frac{\partial \mathcal{U}}{\partial A} \quad (4.1)$$

$$= - \frac{\partial \mathcal{U}}{\partial \phi} \frac{\partial \phi}{\partial A} \quad (4.2)$$

We then have to compute an expression for ϕ as a function of A . For this we will invert the following relation, obtained by computing the determinant of the vectors that generate the hexagon :

$$A(\delta\theta_0, \phi) = \frac{\sqrt{3}}{2} (1 + \ell(\delta\theta_0, \phi))^2 \quad (4.3)$$

$$= \frac{\sqrt{3}}{2} \left(1 + \frac{1}{2} (\cos(\delta\theta_0) + \cos(\phi)) \right)^2 \quad (4.4)$$

There exist several solutions as two angles ϕ correspond to the same area, one with a filament bent upwards, one with a filament bent downwards. Depending of the signe of $\delta\theta_0$, only one of them is physical. Thus we keep the one that minimises the bending energy :

$$\phi(\theta, A) = \epsilon(\delta\theta_0) \arccos(2l - \cos(\delta\theta_0)) = \epsilon(\delta\theta_0) \arccos\left(2\left(\sqrt{\frac{2A}{\sqrt{3}}} - 1\right) - \cos(\delta\theta_0)\right)$$

where $\epsilon(\delta\theta_0)$ in the function that gives the sign of $\delta\theta_0$.

These expressions enable us to compute pressure versus area curves as displayed in figure 4.8. The model differs from figures 4.5, by the hypothesis of inextensible filaments which is relaxed in numerical simulations. However their general trend is similar, as we observe the instable region with positive slope, and the stable ones with negative slopes. We also observe the existence of a collapsed stable geometry, of a collapsed unstable geometry, and a stable equilibrium geometry. The curves are not in quantitative agreement however because of the possibility for forks to open and edges to extend. However the curves display the same qualitative trend, unless for $\delta\theta_0 = -\frac{2\pi}{3}$.

More precisely, this curve displays a behaviour typical of an instability : there exist three equilibrium configurations. The stability criterion is that the slope in this diagram is positive, so two equilibria are stable and one is unstable. From now on we will refer to the lowest area geometry "collapsed" and the largest area "relaxed". From this we can propose a phenomenology for the collapse of a network of prestressed cells on the geometry (α) forced in

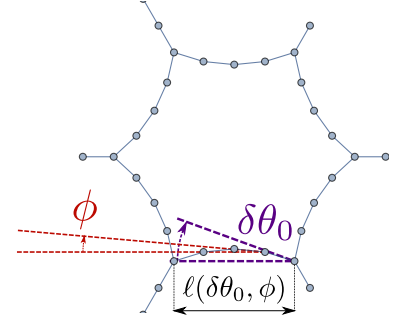


Figure 4.7: System reduced to one degree of freedom

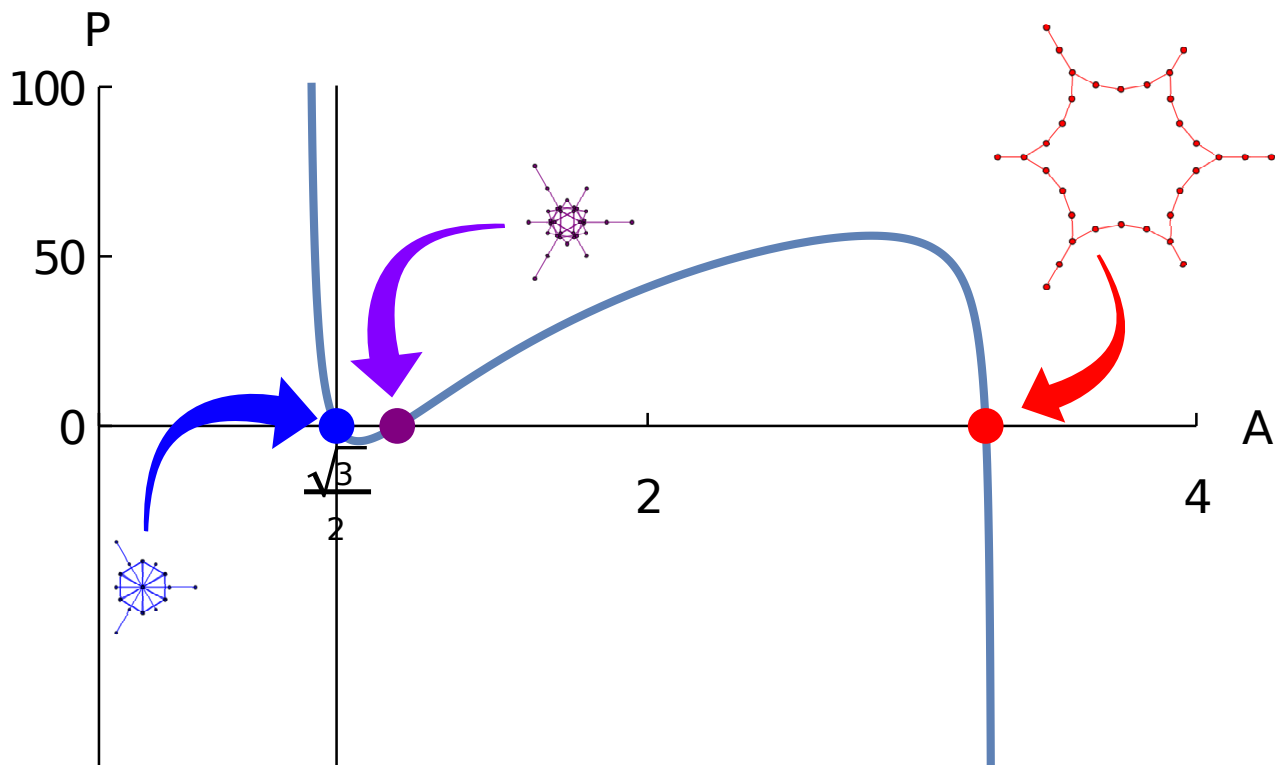


Figure 4.8: Analytically computed pressure versus area curve for the (α) geometry, we took $\delta\theta_0 = 0.1$ as a typical value. We represented the equilibrium geometries with three colors. The purple and blue geometries show how excluded volume can become a necessary ingredient to prevent self intersections in the network.

strain. As we would increase compressive strain, all units cells in the network would get to their relaxed state, then between two characteristic values there would be a coexistence of relaxed and collapsed state to accomodate the total strain. Finally, below some critical strain, all cells would be in their collapsed state and the network fully collapsed.

In practice however the phenomenology would not be so simple as the symmetry of order 6 cannot be kept by the cells when they collapse. Furthermore the collapsed geometry obviously cannot be realised in presence of excluded volume, which we will comment on the next subsection. However, our results show that the presence of residual stress may destabilize the network if representants of the geometry (α) and its family become too numerous. It also says something on the mechanism of collapse when compressing : initially, all cells are at rest. As we reach the metastable area, a increasing fraction of collapsed cells participate in accomodating strain. In the end all cells are collapsed. This foam-like behaviour under compression has been reported for fibrin networks in ⁴, it is consistent with our observations when compressing random networks, despite lacking data on large enough networks.

4.2.2 Excluded volume prevents a full collapse

We saw in the previous subsection that the collapsed configuration displays filament overlaps. It is worth understanding filaments overlap as excluded volume could be a stabilising mechanism of collapsed cells in real networks. In this section we will determine an equation for the point at which the system starts to overlap. This will give the boundary for one line in the diagram 4.11.

The first case possible is when the central subedges of filaments start to overlap, as can be seen on figure 4.9. This gives a first bound :

$$\phi(\delta\theta, \gamma) = \pm \frac{\pi}{2}$$

The second case possible occurs for values of $\delta\theta$ which are bigger, when second nearest neighbour filaments overlap as illustrated figure 4.10. This provides a second bound :

$$\arg\left(e^{i\delta\theta} + e^{i\phi(\delta\theta, \gamma)}\right) = \frac{\pi}{3}$$

This relation being obtained by writing the relative position of the middle site of a filament with respect to the position of a main vertex of the hexagon lattice.

To conclude when the area becomes too small, some filaments get to overlap and excluded volume should come into play. The roughest approximation of it being to replace this part of the $P - A$ diagram by a vertical line below the critical area determined by the criteria above. Indeed, excluded volume doesn't impact the behaviour above this critical area, since filaments are then

⁴ O. V. Kim, X. Liang, R. I. Litvinov, J. W. Weisel, M. S. Alber, and P. K. Purohit. Foam-like compression behavior of fibrin networks. *Biomechanics and Modeling in Mechanobiology*, Feb. 2016

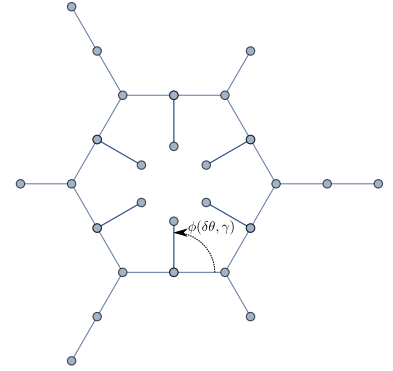


Figure 4.9: Overlap between central subedges for $\delta\theta_0 = 0$.

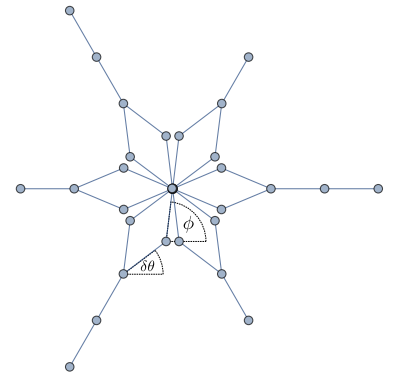
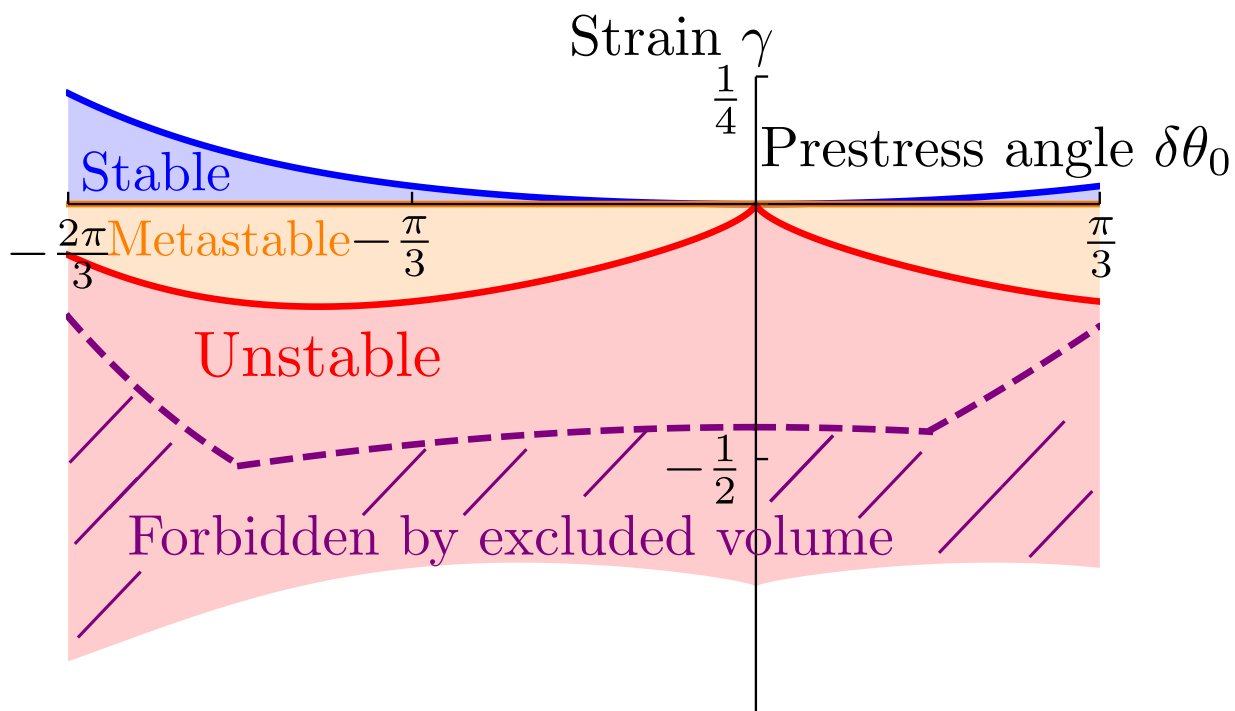


Figure 4.10: Overlap between second nearest neighbors filaments, for $\delta\theta = 0.65$, $\phi = 1.45$.

too far from each other to see this short-range interaction. Thus, it would require an infinite pressure to compress the network further after the edges intersected.

4.2.3 Phase diagram for one geometry



We now have all the elements to construct a phase diagram which displays the stability regions in the $(\delta\theta, \gamma)$ plane. We present it in figure 4.11.

The limits between metastable and unstable regions were obtained with the stability condition :

$$\frac{\partial P}{\partial \gamma} = 0$$

The limits between the metastable region and the stable region obey the rule

$$P(\gamma) = 0$$

The limits for the excluded volume area have been discussed in subsection 4.2.2, we obtain a piecewise defined curve which corresponds to the first filament overlap the compression induces : first neighbours for small $|\delta\theta|$. All the regions below this line cannot be reached without filament overlaps.

This diagram shows an example of how residual stresses induce a collapse on the specific case of geometry (α) .

Figure 4.11: Analytical collapse diagram for the (α) geometry. The white regions are not physically accessible, the blue regions are stable, the orange region is metastable and the red region is unstable. The dashed purple line corresponds to the excluded volume limit : the regions below in this diagram cannot be reached without having filament overlaps.

4.3 Conclusion

After this section, we know more about the non linear response of prestressed networks. Under shear we have seen that regardless of the geometry, the residual stress introduce pretension in the softest modes of the system. As these modes cannot be unfolded indefinitely, there is a transition from a bending dominated linear regime to a stiffening response which is stretching dominated. The relation of elastic response to shear modulus has characteristic exponent of 1. The main effect of $|\delta\theta_0|$ is to shift the range over which the network responds linearly, the linear response modulus increases as $|\delta\theta_0|$ increases.

When the networks get isotropically compressed, the forks induce more and more bending stress on the individual filaments. When the compression rate increases too much this induces buckling of filaments, followed by a local collapse. The compression of large random networks is thus made of a sequence of local collapses favoured by the local geometry of forks. As physical filaments cannot self intersect, they get crashed in contact to each other in collapsed structures stabilised by excluded volume interactions. We made a model of the (α) geometry under compression to explain the mechanism of a collapse for one peculiar geometry, we showed in a diagram that excluded volume allowed the onset of instabilities, but modified the nature of the collapsed state. We suspect this foam-like compression to be consistent with experiments made on fibrin networks.

5

General conclusion

Biopolymer networks are biological structures that appear at different scales. We meet different scales ranging from cells to skin or blood clots. At all these scales, they play an important mechanical role. In cells they are responsible for the so-called motility processes. These processes involve how cells displace and how they deform. In skin they provide skin with elastic properties unusual of ordered crystals. In blood clots they allow wound healing. Finding fiber networks involved in so many biological structures make us wonder the link between the microscopic properties of fibers and the elasticity of their assemblies. It motivates a study that goes across scales, starting from the knowledge of the microscopic structure of fibers to explain the behaviour of the mesoscopic they assemble into. Actin filaments are well characterised microscopically. Their persistence length was measured, their polymerisation process is known, the structure of their building monomers is resolved. They can interact through cross-linkers that can gather them into bundles or connect them at finite angle. Nonetheless, the self-assembly process of actin in presence of large concentrations of cross-linkers can lead to the formation of thick bundles containing up to 30 filaments. These filaments are interconnected into a mesh, and get zipped by cross-linkers through the polymerisation process, up to a point where the steric barrier to overcome stops the process ongoing. These frustrated bundles are thus tensed by the zipping crosslinkers, generating strong residual stresses in the networks, comparable with the energy scales of cross-linkers binding. The effect of these residual stresses on the elasticity of fiber networks is poorly understood and was studied here on bidimensional lattices.

To tackle this problem, Chapter 1 presented a model to simulate the statics of fibers networks as a network of fibers subdivided into N parts, with a bending stiffness on their junctions. We introduced a functional form for residual stresses that included frustrated bundles, but above all it was more general and allowed any frustrated angles in the network. We formulated a few assumptions to circumscribe our study, and we controlled their accuracy. Namely, we went to the limit of very stiff polymers under stretching, and very soft in bending, according to what is known of semiflexible networks. We

also controlled our continuum limit approximation, and studied the limit of infinitely stiff forks. This chapter classified according to their symmetries the unit cells of reference (α), (β), (γ) and (δ) that encompass the possible symmetries of residual stress orientations. This work was a preparatory work towards the systematic study of the effect of geometry on the mechanics of fiber networks.

In Chapter 2 we introduced the numerical methods into play to compute stress and elastic moduli in finite networks. More precisely, we discussed the limitations of the classic finite difference methods. We concluded that this method lacked precision, was time consuming, and missed some feedback on the accuracy of results. We presented an original method of automatic differentiation using hyperdual numbers (a generalisation of complex algebra). This method was robust to finite difference errors, and did not require to adjust a differentiation step by hand. In this chapter we also presented the structure of our code to allow future use of its sections.

In Chapter 3 we tested out the linear response of networks in presence of residual stress. This study was limited to the aforementioned unit cells, since we pre-relaxed edges of the system before computing its elastic moduli, a time consuming operation as the system grows in size. We discovered that residual stress can affect the linear response of elastic networks both in shear and in bulk. We discussed why we only considered shear and bulk response by analysing the symmetry loss of the unit cells in their reference configuration as $|\delta\theta_0|$.

In Chapter 4 we tested the non linear response of prestressed networks to externally imposed strains. We did this under shear and under isotropic compression, for reference unit cells as well as for small lattices with random orientations of forks.

Under shear, we reported that in presence of residual stress, the elastic response was made of a linear regime with constant elastic modulus, and a non linear regime with elastic modulus growing linearly with stress. The non linear threshold in strain decreased with $|\delta\theta_0|$, while in stress it increased.

Under compression, the study was made more difficult by the presence of instabilities. For this reason the chapter described the networks from a numerical point and from an analytic point. Numerically, we tried to compress the network as gently as possible in order to follow a single continuous pressure-strain curve. We did it for the three first unit cells with a variable degree of success. Nonetheless, this study was instructive in that it enabled us to conjecture that the local geometry of forks induced local collapses in random networks, and we verified it on a moderate size random network. We then studied analytically the collapse of the geometry (α) and made a stability diagram for it to confirm our (dirty) observations.

This thesis brought four contributions.

- The first of them is the new procedure to compute differential elastic

quantities around a given configuration of a network. It can also be used to accurately compute the forces and the matrix of local stiffnesses on a system of particles without computing its gradient analytically.

- The second is that residual stresses can either stiffen or soften the linear response of a material around its rest configuration.
- The third is that residual stress can tune the onset of nonlinear response of fibers networks under finite shear.
- The fourth is that residual stresses induce local collapses of networks under isotropic compression, we have proven that these collapses existed, but did not fully characterise their interplay with contact interactions between filaments.

6

Bibliography

- [1] B. Alberts, A. Johnson, J. Lewis, D. Morgan, M. Raff, K. Roberts, P. Walter, J. Wilson, and T. Hunt. *Molecular biology of the cell*. Garland Science, Taylor and Francis Group, New York, NY, sixth edition edition, 2015. OCLC: ocn887605755.
- [2] N. W. Ashcroft and N. D. Mermin. *Solid state physics*. Brooks/Cole Thomson Learning, South Melbourne, repr edition, 2012. OCLC: 935097630.
- [3] C. Ballestrem, B. Wehrle-Haller, B. Hinz, and B. A. Imhof. Actin-dependent Lamellipodia Formation and Microtubule-dependent Tail Retraction Control-directed Cell Migration. *Molecular Biology of the Cell*, Sept. 2000.
- [4] M. V. Baranov, R. A. Olea, and G. van den Bogaart. Chasing Uptake: Super-Resolution Microscopy in Endocytosis and Phagocytosis. *Trends in Cell Biology*, Sept. 2019.
- [5] A. G. Baydin, B. A. Pearlmutter, A. A. Radul, and J. M. Siskind. Automatic differentiation in machine learning: a survey. *arXiv:1502.05767 [cs, stat]*, Feb. 2015. arXiv: 1502.05767.
- [6] L. Blanchoin, R. Boujemaa-Paterski, C. Sykes, and J. Plastino. Actin Dynamics, Architecture, and Mechanics in Cell Motility. *Physiological Reviews*, Jan. 2014.
- [7] A. Bose, M. F. J. Vermeulen, C. Storm, and W. G. Ellenbroek. Self-stresses control stiffness and stability in overconstrained disordered networks. *Physical Review E*, Feb. 2019.
- [8] C. P. Brangwynne, F. C. MacKintosh, S. Kumar, N. A. Geisse, J. Talbot, L. Mahadevan, K. K. Parker, D. E. Ingber, and D. A. Weitz. Microtubules can bear enhanced compressive loads in living cells because of lateral reinforcement. *The Journal of Cell Biology*, 2006.
- [9] C. P. Broedersz and F. C. MacKintosh. Modeling semiflexible polymer networks. *Reviews of Modern Physics*, July 2014. arXiv: 1404.4332.

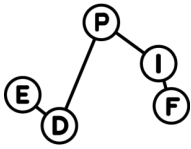
- [10] C. P. Broedersz, X. Mao, T. C. Lubensky, and F. C. MacKintosh. Criticality and isostaticity in fibre networks. *Nature Physics*, Oct 2011.
- [11] J.-F. Bruch, D. Sizaret, A. Brault, F. Tabareau-Delalande, and F. Maître. Étude historique du microscope optique : Des premières lentilles du XVIIe siècle aux techniques de super-résolution et de lecture automatisée. *Revue Francophone des Laboratoires*, Jan. 2015.
- [12] C. Calladine. Buckminster Fuller's "Tensegrity" structures and Clerk Maxwell's rules for the construction of stiff frames. *International Journal of Solids and Structures*, 1978.
- [13] M. Caruel, J.-M. Allain, and L. Truskinovsky. Mechanics of collective unfolding. *Journal of the Mechanics and Physics of Solids*, 76, Mar. 2015.
- [14] M. Claessens, M. Bathe, E. Frey, and A. Bausch. Actin-binding proteins sensitively mediate f-actin bundle stiffness. *Nature materials*, 10 2006.
- [15] S. D. Conte and C. d. Boor. *Elementary numerical analysis: an algorithmic approach*. International Series in pure and applied mathematics. McGraw-Hill, New York, 3. ed edition, 1987. OCLC: 256318941.
- [16] E. B. Davies. *Liner Operators And Their Spectra*.
- [17] J. Deek, R. Maan, E. Loiseau, and A. Bausch. Reconstitution of composite actin and keratin networks in vesicles. *Soft Matter*, 14, 02 2018.
- [18] A. V. Dobrynin, J.-M. Y. Carrillo, and M. Rubinstein. Chains Are More Flexible Under Tension. *Macromolecules*, Nov. 2010.
- [19] J. Dollond and J. Short. Xcviii. an account of some experiments concerning the different refrangibility of light. by mr. john dollond. with a letter from james short, m. a. f. r. s. acad. reg. suec. soc. *Philosophical Transactions of the Royal Society of London*, 1757.
- [20] A. J. Engler, S. Sen, H. L. Sweeney, and D. E. Discher. Matrix Elasticity Directs Stem Cell Lineage Specification. *Cell*, Aug. 2006.
- [21] O. T. Fackler and R. Grosse. Cell motility through plasma membrane blebbing. *The Journal of Cell Biology*, June 2008.
- [22] T. T. Falzone, M. Lenz, D. R. Kovar, and M. L. Gardel. Assembly kinetics determine the architecture of α -actinin crosslinked F-actin networks. *Nature Communications*, Jan. 2012.
- [23] R. Fletcher. *Practical Methods of Optimization; (2Nd Ed.)*. Wiley-Interscience, New York, NY, USA, 1987.
- [24] G. Foffano, N. Levernier, and M. Lenz. The dynamics of filament assembly define cytoskeletal network morphology. *Nature Communications*, Dec. 2016.

- [25] M. F. Fournier, R. Sauser, D. Ambrosi, J.-J. Meister, and A. B. Verkhovsky. Force transmission in migrating cells. *The Journal of Cell Biology*, 188, Jan. 2010.
- [26] M. François. Identification des symétries matérielles de matériaux anisotropes.
- [27] M. Galassi, J. Davies, J. Theiler, B. Gough, G. Jungman, P. Alken, M. Booth, F. Rossi, and R. Ulerich. GNU Scientific Library.
- [28] S. Ganguly, D. Das, J. Horbach, P. Sollich, S. Karmakar, and S. Sengupta. Plastic deformation of a permanently bonded network: Stress relaxation by pleats. *The Journal of Chemical Physics*, (18), Nov. 2018.
- [29] Q. Q. Gao and E. M. McNally. The Dystrophin Complex: Structure, Function, and Implications for Therapy. In R. Terjung, editor, *Comprehensive Physiology*. John Wiley & Sons, Inc., Hoboken, NJ, USA, June 2015.
- [30] M. L. Gardel. Elastic Behavior of Cross-Linked and Bundled Actin Networks. *Science*, 304, May 2004.
- [31] F. Gittes. Flexural rigidity of microtubules and actin filaments measured from thermal fluctuations in shape. *The Journal of Cell Biology*, Feb. 1993.
- [32] H. Goldstein, C. Poole, and J. Safko. *Classical Mechanics*. Addison Wesley, 2002.
- [33] A. A. Harkin and J. B. Harkin. Geometry of Generalized Complex Numbers. *Mathematics Magazine*, Apr. 2004.
- [34] H. Herrmann, H. Bär, L. Kreplak, S. V. Strelkov, and U. Aebi. Intermediate filaments: from cell architecture to nanomechanics. *Nature Reviews Molecular Cell Biology*, July 2007.
- [35] C. Heussinger, M. Bathe, and E. Frey. Statistical Mechanics of Semiflexible Bundles of Wormlike Polymer Chains. *Physical Review Letters*, July 2007.
- [36] C. Heussinger, F. Schüller, and E. Frey. Statics and dynamics of the wormlike bundle model. *PHYSICAL REVIEW E*, 2010.
- [37] R. Hooke, J. Allestry, and J. Martyn. *Micrographia, or, Some physiological descriptions of minute bodies made by magnifying glasses : with observations and inquiries thereupon*. London :Printed by Jo. Martyn and Ja. Allestry, printers to the Royal Society ..., 1665.
- [38] E. M. Huisman and T. C. Lubensky. Internal Stresses, Normal Modes, and Nonaffinity in Three-Dimensional Biopolymer Networks. *Physical Review Letters*, Feb. 2011.

- [39] H. Isambert, P. Venier, A. Maggs, A. Fattoum, R. Kassab, D. Pantaloni, and M. Carlier. Flexibility of actin filaments derived from thermal fluctuations. effect of bound nucleotide, phalloidin, and muscle regulatory proteins. *Journal of Biological Chemistry*, 1995.
- [40] M. Jaspers, M. Dennison, M. F. J. Mabesoone, F. C. MacKintosh, A. E. Rowan, and P. H. J. Kouwer. Ultra-responsive soft matter from strain-stiffening hydrogels. *Nature Communications*, Dec. 2014.
- [41] O. V. Kim, X. Liang, R. I. Litvinov, J. W. Weisel, M. S. Alber, and P. K. Purohit. Foam-like compression behavior of fibrin networks. *Biomechanics and Modeling in Mechanobiology*, Feb. 2016.
- [42] Y. Kosmann-Schwarzbach and F. Singer. *Groups and symmetries: from finite groups to Lie groups*. Universitext. Springer, New York, NY, 2010. OCLC: 297148428.
- [43] O. Kratky and G. Porod. Röntgenuntersuchung gelöster Fadenmoleküle. *Recueil des Travaux Chimiques des Pays-Bas*, Sept. 2010.
- [44] L. Landau, E. Lifshitz, A. Kosevich, J. Sykes, L. Pitaevskii, and W. Reid. *Theory of Elasticity*. Course of theoretical physics. Elsevier Science, 1986.
- [45] A. W. Lees and S. F. Edwards. The computer study of transport processes under extreme conditions. *Journal of Physics C: Solid State Physics*, Aug. 1972.
- [46] A. Lemaître and C. Maloney. Sum Rules for the Quasi-Static and Visco-Elastic Response of Disordered Solids at Zero Temperature. *Journal of Statistical Physics*, Apr. 2006.
- [47] A. J. Licup, S. Münster, A. Sharma, M. Sheinman, L. M. Jawerth, B. Fabry, D. A. Weitz, and F. C. MacKintosh. Stress controls the mechanics of collagen networks. *Proceedings of the National Academy of Sciences*, 112, Aug. 2015.
- [48] T. C. Lubensky, C. L. Kane, X. Mao, A. Souslov, and K. Sun. Phonons and elasticity in critically coordinated lattices. *Reports on Progress in Physics*, July 2015.
- [49] J. C. Maxwell. *The Scientific Papers of James Clerk Maxwell*. Cambridge University Press, Cambridge, 2011.
- [50] H. Miyata, R. Yasuda, and K. K. Jr. Strength and lifetime of the bond between actin and skeletal muscle α -actinin studied with an optical trapping technique. 1996.

- [51] P. Moore, H. Huxley, and D. DeRosier. Three-dimensional reconstruction of f-actin, thin filaments and decorated thin filaments. *Journal of Molecular Biology*, 1970.
- [52] J. A. Nelder and R. Mead. A Simplex Method for Function Minimization. *The Computer Journal*, Jan. 1965.
- [53] A. Ott, M. Magnasco, A. Simon, and A. Libchaber. Measurement of the persistence length of polymerized actin using fluorescence microscopy. *Phys. Rev. E*, Sep 1993.
- [54] C. Pelzl, K. Dürre, and A. Bausch. Reconstituted active actin networks in confinement. *Biophysical Journal*, 106, 01 2014.
- [55] B. A. Purnell. Regrow like an axolotl. *Science*, 2017.
- [56] G. T. Risa, F. Hurtig, S. Bray, A. E. Hafner, L. Harker-Kirschneck, P. Faull, C. Davis, D. Papatziadou, D. R. Mutavchiev, C. Fan, L. Meneguello, A. A. Pulschen, G. Dey, S. Culley, M. Kilkenny, L. Pellegrini, R. A. M. de Bruin, R. Henriques, A. P. Snijders, A. Šarić, A.-C. Lindås, N. Robinson, and B. Baum. Proteasome-mediated protein degradation resets the cell division cycle and triggers ESCRT-III-mediated cytokinesis in an archaeon. preprint, Cell Biology, Sept. 2019.
- [57] P. Ronceray, C. P. Broedersz, and M. Lenz. Fiber networks amplify active stress. *Proceedings of the National Academy of Sciences*, Mar. 2016.
- [58] F. Rückerl, M. Lenz, T. Betz, J. Manzi, J.-L. Martiel, M. Safouane, R. Paterski-Boujemaa, L. Blanchoin, and C. Sykes. Adaptive Response of Actin Bundles under Mechanical Stress.
- [59] J. R. Shewchuk. An introduction to the conjugate gradient method without the agonizing pain. Technical report, Pittsburgh, PA, USA, 1994.
- [60] B. Sjöblom, A. Salmazo, and K. Djinović-Carugo. α -actinin structure and regulation. *Cellular and Molecular Life Sciences*, May 2008.
- [61] F. Spira, S. Cuylen-Haering, S. Mehta, M. Samwer, A. Reversat, A. Verma, R. Oldenbourg, M. Sixt, and D. W. Gerlich. Cytokinesis in vertebrate cells initiates by contraction of an equatorial actomyosin network composed of randomly oriented filaments. *eLife*, Nov. 2017.
- [62] D. Stamenović and D. E. Ingber. Tensegrity-guided self assembly: from molecules to living cells. *Soft Matter*, 2009.
- [63] B. A. Stickler and E. Schachinger. *Basic concepts in computational physics*. Springer, Cham, second edition edition, 2016. OCLC: 951090652.

- [64] R. Virchow. *Die cellularpathologie in ihrer begründung auf physiologische und pathologische gewebelehre*. Berlin, A. Hirschwald, 1858, 1858. Théorie cellulaire.
- [65] M. A. Welte. Bidirectional Transport along Microtubules. *Current Biology*, July 2004.



Titre: Effet des contraintes résiduelles sur l'élasticité des réseaux de fibres.

Mots clés: contraintes résiduelles, polymères semiflexibles, élasticité

Résumé: Les cellules sont les unités fondamentales de tous les organismes vivants. Les cellules eukaryotes sont architecturées autour de fibres aussi diverses que les rigides microtubules et que l'actine semiflexible dans l'ensemble que forme le cytosquelette. C'est à ce titre que le cytosquelette est impliqué dans de nombreux les processus de déplacement et de déformation des cellules, il est aussi responsable de la rigidité mécanique des cellules. En son sein, les filaments d'actine peuvent être réticulés en fagots de plus de 30 filaments, mais aussi s'intersecter à des angles finis. Ces processus sont en compétition lors de l'auto-assemblage des réseaux d'actine, ce qui induit d'importantes contraintes

résiduelles.

Dans cette thèse, nous étudions l'effet des contraintes résiduelles sur l'élasticité des réseaux de fibres en 2 dimensions d'espace. Nous développons une méthode originale pour le calcul des contraintes au bord d'un réseau de fibres et ses modules élastiques. Nous trouvons que les contraintes résiduelles induisent une rigidification du réseau. Les contraintes résiduelles impactent aussi la réponse non linéaire du réseau : nous trouvons qu'elles rendent le réseau mécaniquement instable sous compression, qu'elles contrôlent la largeur domaine de réponse linéaire au cisaillement.

Title: Effect of residual stress on the elasticity of fiber networks.

Keywords: residual stress, semiflexible polymers, elasticity

Abstract: Cells are the basic units of all living organisms. Eukaryotic cells are structured on top of a scaffold of fibers ranging from stiff microtubules to semiflexible actin : the cytoskeleton. As such the cytoskeleton is involved into a broad family of processes of translocation and deformation of cells, it is also responsible for cells mechanical stiffness. The actin filaments into cytoskeleton can be cross-linked into bundles built of as much as 30 parallel filaments, but filaments can get bound at a finite angle also. These processes are in competition during network's self-assembly

and result in strong residual stresses.

In this thesis, we study the effect of these residual stresses on the elasticity of fiber networks in 2 dimensions of space. We develop an original method to compute stress on the boundaries of a network and its elastic moduli. We find that residual stress induces a stiffening in the infinitesimal response of the network. Residual stress also affects the non linear response of the network : we find that it makes the network unstable under compression, and that they control the onset of non linear response to shear.

Université Paris-Saclay
Espace Technologique / Immeuble Discovery
Route de l'Orme aux Merisiers RD 128 / 91190 Saint-Aubin, France